

# Femtosecond Laser Ablation

Dissertation

zur Erlangung des Doktorgrades des  
Fachbereichs Physik der Universität Dortmund

vorgelegt von

Vanja Margetić

Dortmund 2002

Erstgutachter: Prof. Dr. K. Niemax

Zweitgutachter: Prof. Dr. D. Suter

Tag der mündlichen Prüfung: 22.11.2002

# Contents

<b>1</b>	<b>Introduction</b>	<b>4</b>
<b>2</b>	<b>Ultrashort Laser Ablation</b>	<b>7</b>
2.1	Absorption of laser energy . . . . .	8
2.1.1	Metals . . . . .	8
2.1.2	Semiconductors . . . . .	8
2.1.3	Transparent dielectrics . . . . .	9
2.2	Two temperature model . . . . .	9
2.3	Material removal . . . . .	12
2.3.1	Normal vapourisation . . . . .	12
2.3.2	Normal boiling . . . . .	13
2.3.3	Phase explosion (explosive boiling) . . . . .	13
2.3.4	Critical-point phase separation . . . . .	15
2.4	Plasma expansion . . . . .	17
2.5	Nanosecond laser ablation . . . . .	22
<b>3</b>	<b>Laser Ablation Solid Sampling</b>	<b>23</b>
3.1	Detection techniques . . . . .	24
3.2	Matrix effects . . . . .	25
3.2.1	Fractional evaporation . . . . .	25
3.2.2	Internal standardisation . . . . .	26
3.3	Comparison of femtosecond and nanosecond laser ablation . . . . .	27

<b>4</b>	<b>Instrumentation</b>	<b>29</b>
4.1	Description of the laser system and the diagnostic techniques . . . . .	29
4.1.1	Femtosecond laser . . . . .	29
4.1.2	Pulse and beam diagnostics . . . . .	31
4.1.3	Determination of the focused beam area and threshold fluence . . . . .	32
4.2	LIBS . . . . .	34
4.3	TOF-MS . . . . .	35
4.4	ICP-MS . . . . .	39
4.5	LIF . . . . .	40
4.6	Microscopes . . . . .	43
<b>5</b>	<b>Basic Investigation of Ultrashort LA</b>	<b>44</b>
5.1	Crater morphology . . . . .	44
5.1.1	Ablation rate and threshold fluence . . . . .	46
5.1.2	The influence of ambient pressure on the ablation rate . . . . .	52
5.2	Laser ablation plasma properties . . . . .	52
5.2.1	Laser Induced Fluorescence . . . . .	54
5.2.2	Laser Induced Breakdown Spectroscopy . . . . .	62
5.3	Ion emission- direct TOF . . . . .	71
<b>6</b>	<b>Laser ablation sampling for bulk elemental analysis of solids</b>	<b>77</b>
6.1	Analysis of brass . . . . .	77
6.1.1	Comparison of femtosecond and nanosecond LIBS . . . . .	78
6.1.2	Modelling of non-linear calibration graphs . . . . .	83
6.2	Femtosecond LA-ICP-MS . . . . .	92
6.2.1	Analysis of Al samples . . . . .	93
6.2.2	Analysis of glass standards . . . . .	97
<b>7</b>	<b>In-depth Profiling</b>	<b>99</b>
7.1	The goal of the study . . . . .	100
7.2	Definition of depth resolution . . . . .	101

7.3	Cu-Ag layers on Si - LIBS . . . . .	102
7.4	TiAlN-TiN on steel - LA-TOF-MS . . . . .	104
7.5	Co implanted silicon wafer . . . . .	107
7.6	Beam Shaping . . . . .	109
7.6.1	Imaging . . . . .	112
7.6.2	LCD-Spatial Light Modulator . . . . .	115
7.7	Cr and Ni thin films on Si . . . . .	117
7.8	Summary . . . . .	128
<b>8</b>	<b>Conclusion</b>	<b>130</b>
<b>A</b>	<b>Elliptical plume</b>	<b>133</b>
<b>B</b>	<b>Triggering schemes</b>	<b>134</b>
<b>C</b>	<b>TOF - velocity distribution</b>	<b>137</b>
<b>D</b>	<b>LC properties</b>	<b>138</b>

# Chapter 1

## Introduction

Since the first demonstration of the light amplification by stimulated emission of radiation by Maiman in 1960 [1], lasers became a standard tool not only for research laboratories, but also in many fields of technology and engineering. Among the very first applicants were also analytical chemists who studied the applicability of lasers for the analysis of solid samples [2]. If a powerful laser beam impinges on the surface of a solid, a small quantity of the material can be removed. This process is called laser ablation (LA). Typically, a small transient plasma is induced above the sample surface, containing atoms, ions and particles of the ablated material as well as the ambient gas. The studies of the physics of ablation and the use of the laser ablation in microanalysis and spectroscopy developed in the seventies and eighties. During the last 10-15 years, the pulsed laser ablation became more and more popular for the analysis of solid samples. There is a large number of publications devoted to it and important aspects are encompassed in recent reviews [3-6]. In most applications, the nanosecond and picosecond pulsed lasers were used.

The laser solid sampling is so attractive for analytical chemistry because fast element analysis can be performed without any sample preparation. However, the quantification of the results is not so straightforward, and a careful choice of the experimental parameters is crucial. The nature of the laser-solid interaction imposes limits on the performance of ns and ps LA analysis that cannot be overcome by optimisation of measuring conditions or by employing shorter laser wavelengths.

Development of ultrashort pulsed lasers (the term ultrashort is used for the pulses of sub-

picosecond duration) opened many new fields of material research. In the medium intensity range that is typical for the ultrashort laser ablation experiments ( $10^{12}$ - $10^{14}$  W/cm<sup>2</sup>), the most prominent field of application of the femtosecond lasers is the precision microstructuring of diverse materials, from metals and dielectrics to bio-tissues. As a consequence of the specific time scale of an ultrashort laser pulse - solid interaction, the properties of the material removal should also have advantages for chemical analysis of solid samples.

The subject of this thesis is the investigation of the performance of femtosecond laser ablation, in particular in the elemental analysis of solids. Studies of material removal and spectroscopic investigations of the plasma created during the ablation process will be performed for better understanding and for optimisation in respect to analysis. Based on the acquired knowledge and experience, the appropriate experimental parameters for analytical measurements will be found.

The most popular techniques based on the laser ablation sampling are Laser Induced Breakdown Spectroscopy (LIBS), Laser Induced Fluorescence (LIF), Laser Ablation - Inductively Coupled Plasma - Mass Spectrometry (LA-ICP-MS), and Laser Ablation - Time of Flight - Mass Spectrometry (LA-TOF-MS). In LIBS, the emission lines from atoms and ions in the laser induced plasma are measured. The species in the plasma can be detected by LIF which has better detection limits than LIBS. In LA-ICP-MS, the particles created during the ablation process are transported by a noble gas into the ICP where they are atomized and ionised. The ions are then analysed with a mass spectrometer. In LA-TOF-MS, only the ions created during the ablation process are analysed. In order to explore different aspects of femtosecond laser ablation processes, all these techniques will be employed.

From the analytical point of view, femtosecond lasers are expected to overcome some of the severe difficulties immanent to the solid sampling with longer pulses, in particular the elemental fractionation from the laser crater and, for metals, melting and material mixing in the crater region, which worsen the spatial resolution of the analysis. Therefore, binary alloys will be studied which are known to be difficult systems for elemental analysis with nanosecond laser since they often show very strong matrix effects. Furthermore, certified glass samples and aluminium will be analysed.

The improved control of the material removal (no melting and mixing) should be an im-

portant advantage for using fs lasers for rapid and simple surface and surface layer analysis (in-depth profiling of thin layered structures). The reduced thermal diffusion could enable a depth resolution in lower sub- $\mu\text{m}$  range in combination with a good lateral resolution. Laser ablation in-depth profiling could be used for all kinds of solid materials. Investigations employing single-shot multielemental detection techniques will be carried out on conducting as well as non-conducting materials. Strategic guidelines for the development of a routine analytical method for ultrashort laser ablation in-depth profiling will be set.



## Chapter 2

# Ultrashort Laser Ablation

This chapter introduces the basic processes during the ultrashort (sub-picosecond) pulsed laser ablation. The detailed course of this very complex phenomenon depends strongly on many parameters of the laser, the sample and the ambient in which it takes place [7-11]. In general, there is a sequence of the following events:

1. deposition of laser energy into the solid sample
2. rapid (phase) transformation of the laser affected region
3. ejection and separation of matter from the sample surface
4. expansion of the plasma plume into the ambient.

An electromagnetic wave in the form of a very short pulse and with the wavelength from UV to near IR range can interact effectively only with the electron subsystem of a solid. Pulse duration in the sub-picosecond range guarantees that processes (2-4) take place after the laser pulse is over. Thermalisation time of the electrons is of the order of 10 fs - 1 ps [12]. Due to their low heat capacity, electrons can be heated to very high transient temperatures. The hot gas of free electrons thermalises with the lattice within typically 1 - 100 ps, depending on the strength of electron - phonon coupling [13, p. 270]. Only after that, can any significant material removal take place.

There is a distinctive difference in the laser interactions with conductors and dielectrics. In the following, primarily the interaction with metals will be described, and a short outline of the

case of dielectric samples will be given in Section 2.1.3. Models that will be presented in this chapter form a good basis for the interpretation of the obtained experimental results.

## 2.1 Absorption of laser energy

### 2.1.1 Metals

The absorption and reflection of light on metal surfaces is well described by the classical Drude model in which conducting electrons are considered to be free [14]. This applies to the ultrashort pulses as well, providing their intensity is low enough that the electron temperature remains below the Fermi temperature. For example, for copper and for laser pulses of 1  $\mu\text{m}$  wavelength and 1 ps duration, this condition is satisfied for  $I \leq 5 \times 10^{12} \text{ W/cm}^2$  [15]. Laser interacts with a dense cold matter and the spatial electron density profile can be described by a step function. The reflection of light is given by the Fresnel-Drude formulas [16].

For  $I \geq 5 \times 10^{12} \text{ W/cm}^2$ , as well as for longer, nanosecond pulses, an expanding electron density profile has to be taken into account. The laser pulse propagates into a plasma of a steep but non-zero gradient length. Main absorption processes are *the inverse Bremsstrahlung* and the linear resonance absorption at the critical electron density for p-polarisation [7, 15]. At even higher intensities than  $10^{15} \text{ W/cm}^2$ , non-linear effects begin to dominate [17].

Typical intensities used in the femtosecond laser ablation experiments are in the range of  $10^{12}$ - $10^{14} \text{ W/cm}^2$ . The absorption and reflection of ultrashort light pulses by metals obey the laws of linear metal optics up to intensities of  $10^{15} \text{ W/cm}^2$  [15, 18].

### 2.1.2 Semiconductors

As for metals, the absorption of laser light by semiconductors is a linear process [19]. The free-carriers are created as the electrons are excited into the conduction band through a single or two-photon absorption. Further absorption is dominated by the high density free-carriers plasma, and it can be effectively approximated by the Drude model [19].

### 2.1.3 Transparent dielectrics

For dielectric materials for which the laser photon energy is small compared to the material band-gap, it is the multi-photon ionisation process that dominates the initial creation of the free-carriers, accompanied by the avalanche ionisation [20]. If the critical carrier density is reached, the damage will occur. The relaxation of energy from hot electrons to the lattice can result in bond-breaking and induction of defect sites. In the presence of defect states the absorption is more efficient. Therefore, the incubation effects during multi-pulse irradiation are very pronounced. They are manifested as the reduction of the threshold fluence necessary for the material damage when the number of pulses applied to the same spot grows.

## 2.2 Two temperature model

The two temperature diffusion model describes the transition of the laser energy deposited in the electron subsystem of a solid to the lattice. The electron subsystem and the lattice can be described by two different temperatures:  $T_e$  (electrons) and  $T_i$  (lattice), since the time scale of the energy relaxation within the electron subsystem is much shorter than the time necessary to transfer this energy to the lattice.

Thermal diffusion of the hot electrons into the bulk takes place simultaneously with the transfer of energy to the lattice (phonons) by collisions. Heat diffusion of the electron subsystem is much faster than the lattice-mediated diffusion. The thermal conductivity of the lattice can therefore be neglected on the time scale of electron-phonon coupling. The temporal and spatial evolution of the  $T_e$  and  $T_i$  are described by the following coupled one dimensional differential equations [7, 8]:

$$\begin{aligned} C_e \frac{\partial T_e}{\partial t} &= \frac{\partial Q(z)}{\partial z} - \gamma(T_e - T_i) + S \\ C_i \frac{\partial T_i}{\partial t} &= \gamma(T_e - T_i) \\ Q(z) &= -k_e \frac{\partial T_e}{\partial z} \\ S &= I(t)\alpha \exp(-\alpha z) \end{aligned} \tag{2.1}$$

where  $z$  is chosen perpendicular to the sample surface.  $Q(z)$  is the heat flux,  $I(t)$  the laser

intensity measured in  $[\text{W}/\text{m}^2]$ ,  $\alpha$  the material absorption coefficient including the surface absorptivity, while  $C_{e,i}$  are the electron and lattice heat capacities per unit volume.  $\gamma$  is the electron-phonon coupling coefficient and  $k_e$  the electron thermal conductivity.

The electron temperature at the end of the laser pulse is determined by eq. 2.1, neglecting the electron heat diffusion and electron-phonon coupling during the pulse duration. After that, the laser source term  $S$  is zero. Solving the first three equations, assuming the rectangular laser pulse of intensity  $I_0$  and duration  $\tau_L$ , results with the approximate expression for attainable lattice temperature

$$T_i \simeq \frac{F_a}{C_i} \frac{1}{l^2 - \delta^2} [l \exp(-z/l) - \delta \exp(-z/\delta)],$$

where  $F_a$  is the absorbed fluence,  $\delta = 1/\alpha$  is the skin depth, and  $l$  is the electron heat penetration depth. It is given by

$$l = \sqrt{D\tau_a} \quad (2.2)$$

$D$  being the electron diffusivity constant, and  $\tau_a$  the time necessary for transfer of energy from the electrons to the lattice. The absorbed fluence is defined as

$$F_a = (1 - R)I_0\tau_L = \frac{E(1 - R)}{A}$$

with the laser pulse energy  $E$ , the sample reflectivity  $R$ , and the laser focal spot area  $A$ .

The ablation depth per laser pulse (or ablation rate) can be calculated *assuming an Arrhenius-type of evaporation* [8, 21]. A significant evaporation can occur if  $C_i T_i \geq \rho\Omega$ , where  $\rho$  is the density and  $\Omega$  the specific (per unit mass) heat of evaporation. Two cases have to be distinguished:

1. for low fluence, the number density of hot electrons is considered to be low enough that the energy transfer between the electrons and the lattice occurs only within the area characterised by the skin depth  $\delta$ ;
2. for high fluence, the electron diffusion length  $l$  becomes significant and the ablation rate increases.

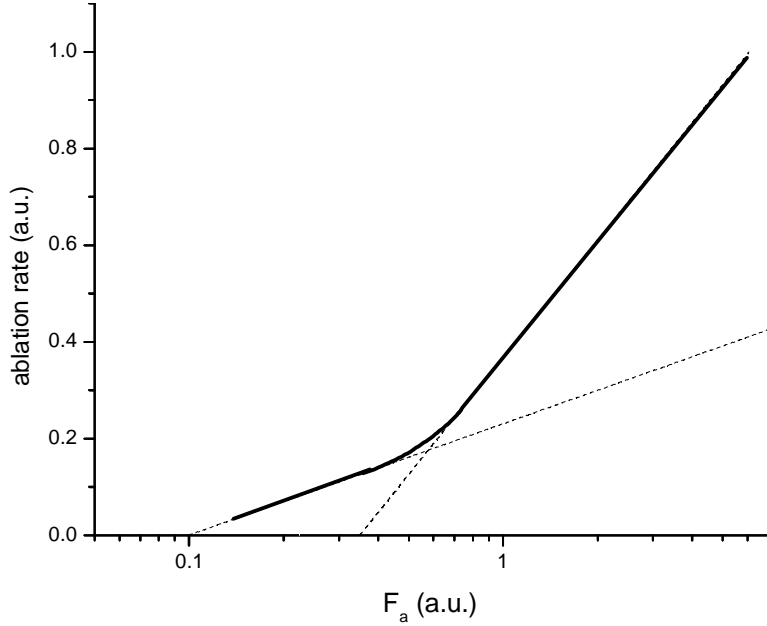


Figure 2-1: Dependence of the ablation rate on the laser fluence (full line). Broken lines are extrapolations from which the two threshold fluences, for high and for low energy regime, are determined.

In the first, the low energy case, the ablation depth per pulse,  $L_\alpha^\delta$ , is:

$$L_\alpha^\delta \cong \delta \ln\left(\frac{F_a}{F_{th}^\delta}\right), \quad F_{th}^\delta = \rho\Omega\delta \quad (2.3)$$

In the second case, the high energy case,  $L_\alpha^l$  is:

$$L_\alpha^l \cong l \ln\left(\frac{F_a}{F_{th}^l}\right), \quad F_{th}^l = \rho\Omega l. \quad (2.4)$$

$F_{th}^\delta$  and  $F_{th}^l$  are the ablation thresholds for the low fluence and the high fluence regimes, respectively. In the sub-picosecond range, the threshold fluence for ablation of metals and semiconductors does not significantly depend on the pulse duration [13]. The dependence of the ablation rate on the laser fluence is shown in Figure 2-1 [8, 9].

The depth of the zone affected by the surface radiation with an ultrashort laser pulse depends strongly on the electron heat penetration depth. It is shorter for materials with strong electron-phonon coupling (compare eq. 2.2), such as the transition metals with unfilled d shell, than

for good conductors as Ag and Cu [22, 23]. However, if the laser fluence is sufficiently low, the ablation depth can be even smaller than the optical penetration depth (eq. 2.3).

The validity of this model for the ultrashort laser ablation of metals has been experimentally verified [7, 8, 22, 23]. For dielectrics, it should give a qualitatively good description, but some additional ways of the energy dissipation within the crystal should be taken into account [20].

## 2.3 Material removal

The mechanisms governing the material removal during the ultrashort laser ablation are still subject to intensive investigations. Final lattice temperatures can be calculated from the two temperature diffusion model, presented in Section 2.2. For typical intensities used in sub-picosecond laser ablation ( $10^{12}$ - $10^{14}$  W/cm<sup>2</sup>), maximum temperatures of several thousand Kelvin are achieved in the surface layer, whose thickness is of the order of magnitude of the optical skin depth. Several processes are being discussed:

1. normal vapourisation
2. normal boiling
3. phase explosion (explosive boiling)
4. critical-point phase separation.

The first three were considered for longer-pulsed laser ablation. The critical-point phase separation [24] is suggested as the possible mechanism with ultrashort pulses only. All of them are termed thermal processes since they occur after the electron relaxation with the phonons, when the system is considered to be in a state of local equilibrium and the temperature has been established.

### 2.3.1 Normal vapourisation

Normal vapourisation refers to the particle emission from the extreme outer surface. The flux of the atoms leaving the surface (atoms cm<sup>-2</sup>s<sup>-1</sup>) is given by the Hertz-Knudsen equation [25]

$$\Phi_{vap} \approx \eta p_{sv} (2\pi m k_B T)^{-\frac{1}{2}}$$

and the velocity of surface recession is

$$\frac{\partial z}{\partial t}_{z=0} \approx \Phi_{vap} * \frac{m}{\rho} \approx \eta p_{sv} (2\pi m k_B T)^{-\frac{1}{2}} \lambda^3.$$

Here  $\eta$  is the vapourisation coefficient,  $p_{sv}$  is the saturated vapour pressure,  $m$  is the particle mass,  $k_B$  the Boltzmann constant,  $T$  the target temperature,  $\rho$  the target density, and  $\lambda$  the mean interatomic distance. An evaluation of the vapourisation velocity for different metals and for the temperatures straddling their boiling temperatures shows that, within 1 ns, much less than a monolayer of atoms can be vapourised [26]. This process, therefore, does not significantly contribute to the material removal during ultrashort laser ablation.

### 2.3.2 Normal boiling

Normal boiling involves heterogeneous vapour bubble nucleation at the boiling temperature ( $T_b$ ). The *heterogeneous nucleation* takes place on the outer surface of the liquid, on impurities or defects in the liquid bulk, or at the underlying or enclosing solid surface. Once formed, the bubbles have to diffuse and escape from the outer surface of the liquid. The bubble diffusion distances in liquids are of the order of 1-10 pm in 1 ns [26], meaning that this process is too slow to account for the material removal by ultrashort laser pulses.

### 2.3.3 Phase explosion (explosive boiling)

Even for nanosecond laser pulses, the normal boiling process can be too slow to keep the temperature close to  $T_b$ . Rapid heating to temperatures much higher than the boiling temperature leads to the superheated, metastable state of liquid. Figure 2-2 shows a temperature-density phase diagram. The dashed line represents the binodal curve which is a boundary between the one-phase region (vapour, liquid, supercritical) and the two-phase regime (gas-liquid). The dotted line is the spinodal curve, the coexistence line of stable and unstable states and the boundary of absolute instability. Their common vertex is the critical point. In between the binodal and the spinodal are the metastable regions (supercooled vapour and superheated liquid (SHL)). The dash-dotted arrow shows schematically the transition from the solid density sample at room temperature (a) to a superheated liquid state.

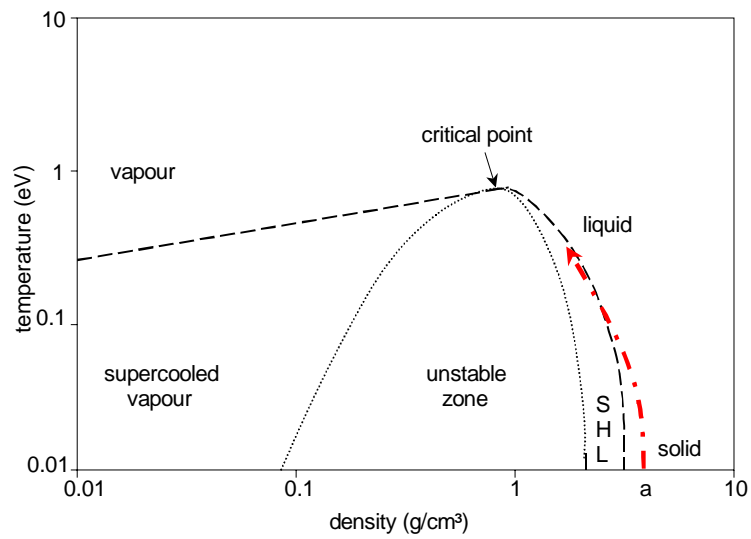


Figure 2-2: Temperature-density phase diagram typical for metals. Dashed line is the boundary between the one-phase and two-phase regime (binodal). Dotted line is the spinodal curve- the boundary of absolute instability. SHL = superheated liquid. The dash-dotted line schematically represents the transition from the cold solid to the superheated liquid state.



Large-scale density fluctuations are characteristic for the metastable regions. In that way, the sample makes a rapid transition from superheated liquid to a mixture of vapour bubbles and liquid droplets. This kind of bubble formation takes place spontaneously anywhere in the superheated volume and it is called *homogeneous nucleation* [27, 28]. At temperatures close to  $T_{critical}$  and in the vicinity of the spinodal, the rate of the homogeneous nucleation is so high that the number of critical nuclei (vapour bubbles that are big enough not to collapse) formed within  $\sim 1$  ns is sufficient for an *explosive* relaxation of the heated region into a mixture of vapour and droplets [25].

### 2.3.4 Critical-point phase separation

Considering of the time scale of the electron-phonon coupling and the final lattice temperature values that can be reached after the sample irradiation by ultrashort laser pulses shows that the course of the phase transition should differ from the one discussed for the phase explosion and nanosecond pulses. Figure 2-3 shows a temperature-density phase diagram (as in Figure 2-2) with several possible courses of the phase transitions caused by an ultrashort laser pulse (arrows) [24].

The heating rates of up to  $10^{15}$  K/s transfer the material isochorically into the hot, pressurised (several GPa), fluid state with the temperature close to or well above the critical temperature (the vertical solid line AB in Figure 2-3). Some of the particles in the uppermost layer have enough energy to transfer into the vapour phase directly (line AC). The pressure gradient causes an expansion of the layer away from the target (and the formation of a shock wave that propagates into the solid). At this point, the ambient pressure has little influence on the processes since it is much lower than the pressure within the hot layer. The expansion is accompanied by adiabatic cooling (line BD). The parts of the layer material that pass through the states close to the critical point can

- vaporise directly,
- reach the states of a superheated liquid,
- supercooled vapour,
- return into the solid state,

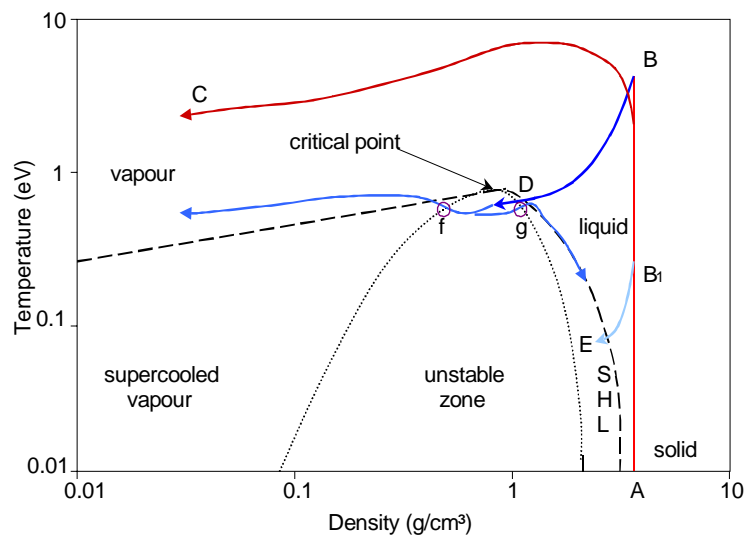


Figure 2-3: Temperature-density phase diagram typical for metals. Dashed line is the boundary between the one-phase and two-phase regime (binodal). Dotted line is the spinodal curve- the boundary of absolute instability. SHL = superheated liquid. Full lines schematically represent several possible courses of phase transition during the fs-laser ablation.

- or even enter the unstable zone of the phase diagram.

In the unstable zone, the smallest fluctuation will cause the rapid evolution of the thermodynamic state of the matter towards one of the two extrema of the isotherm on the spinodal curve (line fg) [24, 27], so that either bubbles or droplets are formed. The processes within the metastable regions are as described in Section 2.3.3. The bubble expansion through which the surrounding droplets are eventually pushed back is an *explosive* phenomenon. If the maximal lattice temperature is not above the critical temperature, the material can still reach the state of superheated liquid (line B<sub>1</sub>E) [24].

## 2.4 Plasma expansion

The onset of the material removal described in the previous section takes place within a very short time after the pulse (1-100 ps): on the time scale of the plasma expansion into the ambient (microseconds), this complete series of events can be regarded as a momentary release of energy. The plasma is initially much smaller than the distances at which the expansion is observed. These are the conditions under which the point blast model can be applied. The spherical expansion model developed by Arnold [29] is based on the laws of mass, energy and momentum conservation<sup>1</sup>. It can be applied to elliptically shaped plumes by simple scaling of the solid angle (Appendix A).

The segmentation of the plasma in the spherical expansion model is schematically presented in Figure 2-4. The initial size of the plume is given by the radius  $R_0$ .

In a vacuum, the plume is free to expand adiabatically. Initially is the energy of the plume purely thermal. During the expansion it is transformed into kinetic energy. When the plume radius is of the order of several  $R_0$ , the energy is almost completely transformed and the maximum velocity is reached that remains constant during further expansion [13].

In the presence of the ambient gas, the plume acts as a piston. The atmosphere is considered to be a homogeneous gas, with constant specific heat and density  $\rho_g$ . The gas is compressed and heated in the external shock wave (with radius  $R_{SW}$ ) which in turn decelerates the plume.

---

<sup>1</sup>The experimental evidence for the spherical shape of the shock wave and the plume can be found for example in the stroboscopic shock wave photography [30], time-resolved photography [31], and shadowgraphic imaging [32] studies of nanosecond laser ablation plumes.

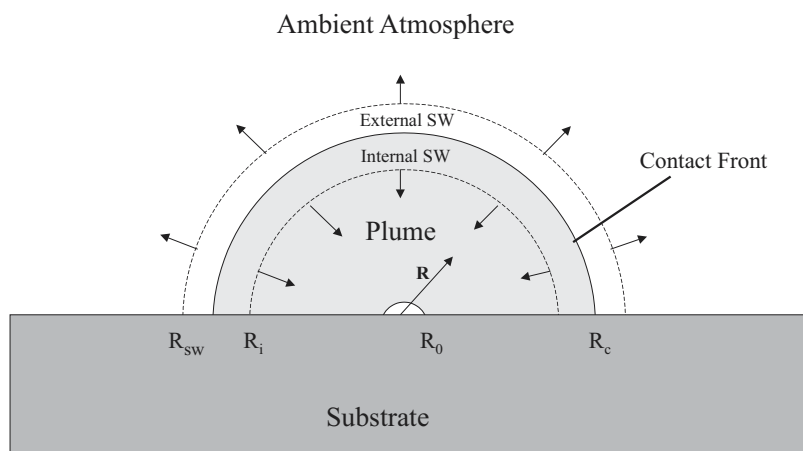


Figure 2-4: A scheme of the plume in the spherical expansion model.  $R_0$  is the initial radius of the plume. The contact front between the plume and the ambient ( $R_c$ ) is moving with the velocity  $R'_c$ .  $R_{SW}$  denotes the front of the external shock wave. The internal shock wave ( $R_i$ ) propagates inwards.

If the mass of the gas in the external shock wave is comparable to or bigger than the mass of the plume, the deviations from the free expansion will occur and the plume will be slowed down. A high counter pressure builds up in the ablated material near to the contact front ( $R_c$ ). In that region, the gas temperature is raised as the plume molecules collide with those of the gas and become reflected. The density is higher than in the centre of the plume. The internal shock wave ( $R_i$ ) formed in such a way propagates inwards. A significant part of the plume energy becomes thermal as the internal shock wave reaches the centre. Much weakened, it is reflected and the plume homogenises. Mixing of the plume and the ambient gas is not treated by the model.

The model considers the redistribution of energy between the thermal and kinetic energies of the plume and the shock waves. Equations for four dynamic variables  $R_i$ ,  $R_{SW}$ ,  $R_c$ , and  $R$  are formulated from the conservation laws derived from gas dynamics [29]. The mass conservation within the plume with a strong internal shock wave yields:

$$M_p(R_i, R) + M_i(R_c, R_i, R) = M$$

$M_p$  and  $M_i$  represent the mass in the plume and the internal shock wave respectively and  $M$  is the total ablated mass. The equation defines the position  $R_i$  of the internal shock wave. Mass conservation in the external shock wave yields the differential equation for  $R_{SW}$ :

$$M_{SW}(R_c, R_{SW}, \rho_{SW}(R'_{SW})) = M_{ambient}(R_{SW}, \rho_g).$$

The equation states that the amount of compressed gas in the external shock wave (mass in the layer between  $R_c$  and  $R_{SW}$ ) is equal to the amount of ambient gas that is repulsed by the plume. No diffusion between ablated material and ambient gas is considered.

The overall energy conservation states that the total energy in the plasma, i.e. the laser energy minus losses due to reflection, heat diffusion, plasma radiation, etc., is equal to the kinetic ( $E_k$ ) and thermal ( $E_t$ ) energies in the different parts of the plasma (subscript p stands for plume):

$$E = E_{pk}(R_i, R, R') + E_{pt} + E_{ik}(R_i, R_c, R, R') + E_{it}(R_i, R_c, p_c) +$$

$$+E_{SWk}(R_c, R_{SW}, R'_c, R'_{SW}) + E_{SWt}(R_c, R_{SW}, p_c).$$

This expression can be considered as a differential equation for  $R_c$ . Assuming a spatially homogeneous pressure within the shock waves, the thermal energies  $E_{it}$  and  $E_{SWt}$  are determined by  $p_c$  which is the pressure at the contact surface in the semi-spheres of the shock waves.  $p_c$  can be obtained from Newton's law describing the balance of forces for the external shock wave:

$$\frac{d}{dt} [P_{SW}(R_c, R_{SW}, R'_c, R'_{SW})] = 4\pi R_c^2 p_c - 4\pi R_{SW}^2 p_{ambient}.$$

$P_{SW}$  denotes the momentum of the shock wave which also has to be estimated. After insertion of the explicit formulas for the different terms with the appropriate initial conditions, these equations can be solved numerically. For different stages of the plasma expansion, approximated solutions exist [13, p. 638]. The temporal behaviour of radii  $R_i$ ,  $R_c$ ,  $R_{SW}$ , and  $R$  obtained from such a numerical calculation is plotted in Figure 2-5 in a dimensionless presentation [29].

At the earliest times, the plume evolution does not differ from the free expansion in vacuum, presented by  $R$ . Later, the plume deceleration can be seen from the increasing difference between  $R_c$  and  $R$ . The decrease of the radius  $R_i$  marks the moment in which the internal shock wave reaches the centre. Its further reflections are not treated by the model, and the plume is considered to be homogeneous after that. Providing the external shock wave is strong enough, the plume will be stopped and the contact front radius  $R_c$  will not grow further. At that point, the validity of the model becomes limited since effects like diffusion become significant. The time scale of the expansion depends strongly on the total energy of the plume and the ambient pressure, which can be seen from the Figure 2-5. For example, the front of the plume produced by a 210  $\mu\text{J}$  femtosecond pulse reaches the 1 mm distance from the sample surface at 100 ns after the pulse at 1 mbar argon pressure, and at 30  $\mu\text{s}$  when the pressure is 855 mbar (see Section 5.2.1). Under certain conditions, it is possible that the laser induces a plasma breakdown in the gas above the sample surface. The mixing of this plasma with the plume of ablated material is rather complicated. This phenomenon can be avoided with ultrashort pulses by careful focusing (beneath the sample surface) and by keeping the laser energy density below the gas plasma breakdown threshold (which is lower for higher pressure). Laser ablation with longer, nanosecond pulses inevitably involves the buffer gas plasma.

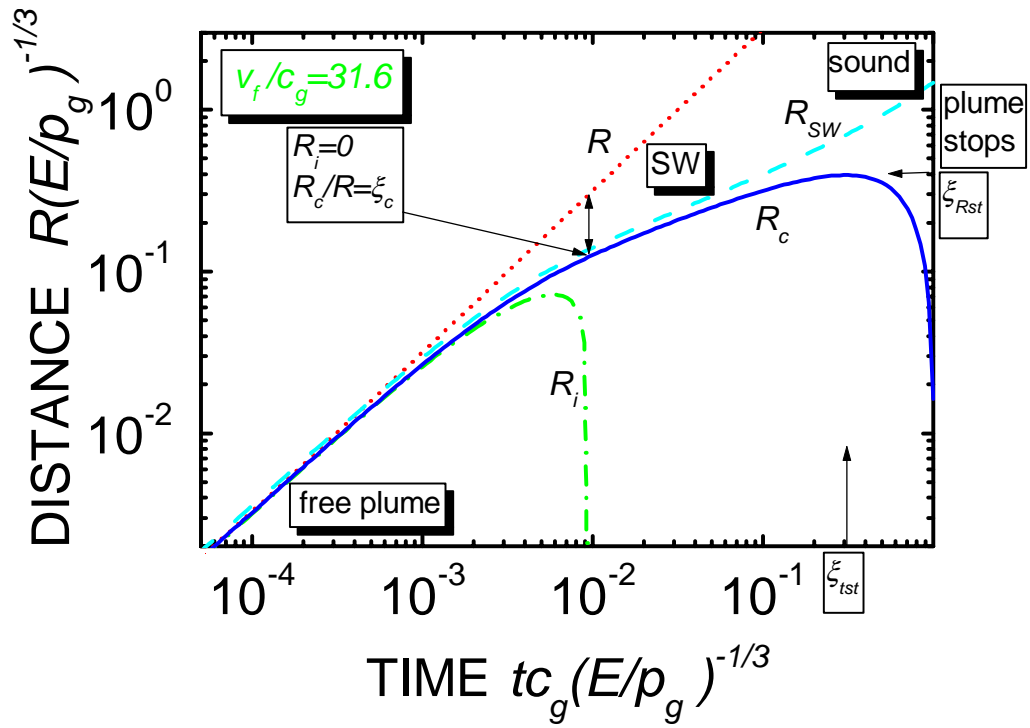


Figure 2-5: Dynamics of plume expansion in dimensionless variables (from [29]). Dotted line: free plume  $R$ ; dash-dotted line: internal SW  $R_i$ ; dashed line: external SW  $R_{SW}$ ; solid line: contact boundary  $R_c$ .  $v_f$  is the free plume expansion velocity and  $c_g$  the sound velocity in given medium.

## 2.5 Nanosecond laser ablation

From the time-scales of the processes during the ultrashort pulse ablation described above, it is evident that a nanosecond laser pulse interacts with many transient states of the matter, including the expanding plume and the ambient gas plasma. Most of the limitations in applications of nanosecond laser pulses can be understood from these basic considerations. The energy deposition is much slower, so that the thermal diffusion of the lattice is significant and cannot be neglected. The electrons and the ions can be considered to be in equilibrium during the nanosecond ablation process. The longer the pulse, the deeper and wider is the laser affected zone, which sets the limits on the precision of microstructuring and analytics. The threshold fluence depends therefore on the pulse length ( $F_{th} \sim \sqrt{\tau_{pulse}}$ , for  $\tau_{pulse} > 1 \text{ ps}$ ) [7], since there is a certain energy density that is necessary for the material removal. Typically, the femtosecond threshold fluence values are about one order of magnitude lower than the nanosecond ones [13, 33].

The phase transition processes have been discussed in Section 2.3. The sample surface can be heated up to temperatures close to the critical point, which can result in explosive boiling [26]. Due to the long duration of the ablation process, melting cannot be avoided. The plume expansion is complicated by plasma absorption of the laser light, which in turn reduces the efficiency of the energy deposition into the sample (*plasma shielding*). All that has consequences for the analytical sampling that is discussed in Chapter 3.



## Chapter 3

# Laser Ablation Solid Sampling

The pulsed laser ablation is a method of solid sampling for *elemental analysis* [3-6]. This Chapter introduces the analytical aspects of LA and the detection techniques that will be used in this thesis. The experimental details will be discussed in the following Chapters. Here, the difficulties encountered in quantitative analysis by LA will be addressed. Their solution or avoidance is the motivation for the analytical part of this study.

The most important advantages of LA solid sampling are the following:

- no (or very little) sample preparation is necessary so that the results can be obtained very fast;
- all solid materials can be sampled by laser ablation;
- small material quantities can be sampled by focusing the laser beam- microanalysis with high spatial resolution is possible;
- it can be performed in various environmental conditions;
- it can be coupled to different detection techniques, from optical spectroscopy to mass spectrometry techniques.

### 3.1 Detection techniques

One of the simplest and widely used detection techniques is LIBS, where *the light emission of the plasma plume* is observed spectrally resolved. Laser ablation plasmas are transient in nature and their emission decays within few tens of microseconds after the pulse (for fs-ns pulses). Quantitative analytical measurements should be performed after the atomisation processes in the region of observation are completed [34] and for this reason gateable detectors are required. LIBS can be performed in the atmospheric conditions, although the performance is better in a protecting noble gas atmosphere at low pressure (better signal-to-noise ratio and repeatability of the results). Typical detection limits are in the ppm range.

In LIBS, only the atoms and ions in excited states are the useful source of information. Significantly better detection limits can be reached if the sampled material is re-excited. The possibilities range from various fluorescence spectroscopic methods to a post-ionisation with another light source or a transport of the ablated matter into another plasma. This last approach is employed in LA-ICP-MS for which the detection limits are in the ppb to ppt range: the sample is placed in a gas tight chamber and *the particles created in the ablation process* are transported in a continuous flow of a suitable carrier gas (typically Ar, He) to the inductively coupled plasma. There, the particles are evaporated and ionised and the ions are measured in the mass spectrometer. Reliable, **multielemental measurements over wide concentration ranges** are possible.

Another detection technique that will be presented in this thesis is the direct coupling of LA with a time-of-flight mass spectrometer (LA-TOF-MS). The ablation is performed in the ultrahigh vacuum conditions and *the ions created during the ablation process* are mass(/charge) resolved and detected. Very small sampled quantities are sufficient for **single shot multielemental** analysis. Although the version of the instrument available for this study does not allow quantitative results on elemental composition, they could, in principle, be obtained by the TOF-MS technique [35, 36].

In general, all the measurement stages between the material removal from the sample and the signal detection can influence the analytical result. Their understanding is important for successful applications of the laser ablation sampling. The assumption that the composition of the sampled material (the atoms/ions that contribute to the signal) is representative of

the sample itself is, unfortunately, not always valid. The experimental parameters have to be carefully optimised for a given analytical problem, whereby the highest signal-to-noise ratio is not always the best optimisation criterion that will ensure accurate results [37, 38, 39].

## 3.2 Matrix effects

From the discussions in the previous Chapter it can be seen that the characteristics of the laser ablation process (absorbed energy, threshold fluence, amount of ablated material, thermal diffusion) strongly depend on the sample properties, composition and structure. The ablated mass and the yield of atoms, ions and particles, together with the laser and ambient parameters, are the starting conditions for the laser plasma evolution. The term matrix effects refers to all influences of the sample's matrix composition on the elemental sensitivities of the analytical method. These influences can result from different reasons (e.g. thermodynamics), and may lead to inaccurate results. They can arise in any phase of the analysis, from the ablation process to the signal detection. Some of the matrix effects, such as the differences in ablated mass, can be eliminated by the internal standardisation procedure (Section 3.2.2). An important and often discussed problem for the laser ablation sampling is the fractional evaporation.

### 3.2.1 Fractional evaporation

Fractional or preferential evaporation is especially pronounced for elements with a large difference in vapour pressures/evaporation temperatures. It can induce an enrichment or a depletion of some matrix or trace components in the sampled material so that its stoichiometric composition does not correspond to that of the sample. Volatile elements evaporate faster and can more easily diffuse out of the sampling volume.

In the laser ablation process, the preferential evaporation might take place during the material removal from the sample surface (*from the crater*) **or** within the plume (*from ejected material*). The first effect happens mainly during the cooling of the surface after the pulse. It grows with multiple pulses on the same spot, since each pulse interacts with the surface of slightly different composition. The ratio of the elemental signals is a function of the number of applied pulses [47]. As a consequence, there is a low repeatability of the results, even for

homogeneous samples. Since the evaporation from a molten phase is typical for the ablation with longer pulses, the occurrence of the fractionation effects is more probable. Moreover, the remaining molten material is subject to mixing, so that the spatial (depth) information is lost.

The fractionation from the ejected material within the plume can be significant if the evaporation of droplets and particles is not complete. A particle size distribution dominated by smaller particles is therefore favourable for the suppression of fractionation effects.

Fractional evaporation is not limited only to the ablation process. In plasma sources that are used for the post-excitation (e.g. ICP), the ablated particles should completely evaporate prior to the detection as well. An incomplete evaporation can lead to the non-stoichiometric plasma composition. That is one of the reasons why the size distribution of the laser ablated particles is a key issue for analytics [40]. Another reason is the transport efficiency. The transport itself can participate in the fractionation effects by having an enhanced/reduced efficiency for the particles that have already undergone the fractional evaporation during the ablation process, or that will contribute to it in the course of post-excitation.

### 3.2.2 Internal standardisation

A quantitative elemental analysis is possible through comparison with the certified samples of known composition - standards [34, 41, 42, 43]. Different physical properties of the unknown sample and the standard lead to different sampling quantities, particle size distributions, ionisation degrees, and atomic and ionic level occupations. To avoid these differences, relative intensities are evaluated.

For optical emission measurements, assuming the local thermodynamic equilibrium conditions in plasma, the ratio of the line intensities of elements  $a$  and  $b$  is given by

$$\frac{I_{ij}^a}{I_{kl}^b} = \frac{A_{ij}g_j\lambda_{kl}n_{tot}^a}{A_{kl}g_l\lambda_{ij}n_{tot}^b} \frac{U^b(T)}{U^a(T)} \exp\left(\frac{-(E_j^a - E_l^b)}{kT}\right), \quad (3.1)$$

where  $A_{mn}$ ,  $\lambda_{mn}$ ,  $g_n$  and  $E_n$  are the transition probability, the wavelength, the statistical weight and the energy of the upper level respectively;  $U(T)$  is the partition function,  $n_{tot}$  the total density of emitting particles (atoms or ions),  $T$  is the excitation temperature, and  $k$  the Boltzmann constant. By choosing the lines of the two elements with similar upper energy level (i.e.

with similar lower energy level for LIF),  $E_j^a \approx E_l^b$ , the following relation is valid

$$\frac{I_{ij}^a}{I_{kl}^b} = C \frac{n_{tot}^a}{n_{tot}^b} \frac{U^b(T)}{U^a(T)}.$$

This enables the comparison of the element concentrations down to a constant factor.

The signal obtained in a LA-ICP-MS measurement is proportional to the analyte concentration  $n_i$  and a sensitivity factor  $S_i$  which includes ionisation efficiency of the ICP for the given element. Providing the ablated material has the same stoichiometry as the sample itself, the efficiency of the transport from the ablation chamber to the ICP is same for all components, and there are no fractionation effects from the ICP, the ratio of two elements' signals is

$$\frac{I_1}{I_2} = \frac{n_1 S_1}{n_2 S_2} = \frac{n_1}{n_2} S_{12},$$

and the relative sensitivity factor  $S_{12}$  can be determined from the measurement of the standard sample under the same conditions.

### 3.3 Comparison of femtosecond and nanosecond laser ablation

Most of the research and applications of the laser ablation in analytics have been done with nanosecond lasers. Lasers of all wavelengths can be used for reproducible and accurate sampling [34, 38, 44-46]. There are, however, reports of the strong matrix effects in nanosecond laser ablation sampling which make quantitative analysis of certain samples very difficult. Especially problematic are alloys such as brass [34, 47-51] to which part of this thesis is devoted.

As already discussed in Section 2.5, a *nanosecond laser pulse* interacts with different *transient* states of material, as well as with the *plasma* cloud above the sample. The main part of the material evaporates from the molten phase and some of the expelled droplets evaporate later in the hot plasma. Under such ablation conditions, one can expect the preferential (fractional) evaporation to occur. Since the absorption process of inverse Bremsstrahlung is more efficient for longer wavelengths, all the effects connected to the plasma shielding are stronger for the infra-red lasers than for the UV ones. In recent analytical papers, a trend towards UV lasers [39] and lasers with shorter pulse duration [52-57] can be observed.

The time scales of the processes during the *femtosecond laser* ablation enable very efficient energy deposition into the sample and the material does not seem to be removed through the classical melting and evaporation. In addition, the post-heating of the plume can be neglected so that the risk of the fractional evaporation during the ablation process itself is minimised. A careful use of the detection techniques is still a necessary condition for obtaining accurate analytical results.

Another advantage that the ultrashort pulses have for the analytics are the reduced thermal effects that allow better spatial resolution. Analyses of the in-depth profiles with sub-micrometre resolution should be possible, as this thesis will demonstrate.

# Chapter 4

## Instrumentation

The experimental setup for laser ablation consists of a laser, a chamber in which the investigated sample is placed under vacuum conditions or in a noble gas, and in-situ and ex-situ analytical instrumentation. Throughout this work, several complementary techniques were used to study the ultrashort laser ablation of solids: TOF-MS detects ions as direct products of a LA process; optical emission and LIF extracts the information on atoms and ions in LA plasma, e.g., their spatial and temporal behaviour and plasma excitation temperature. ICP-MS analyses the ablated material in the particle form, which can not be studied with the first two methods. Finally, exploring the crater morphology is important for characterisation of the ablation process.

### 4.1 Description of the laser system and the diagnostic techniques

#### 4.1.1 Femtosecond laser

The CPA-10 femtosecond laser system (Clark-MXR Inc., MI, USA) used for the ablation consists of a self-starting mode-locking seed laser (SErF), a pulse stretcher, a Ti-sapphire regenerative amplifier (TRA) and a pulse compressor. Technical data of the system are summarised in Table 4.1. The seed laser is an erbium doped fiber ring laser whose short pulses have to be stretched before entering the amplifier. After passing through the stretcher, the pulses ( $\approx 300$  ps long) are inserted into the Ti-sapphire regenerative amplifier pumped by a frequency

output	$\lambda(\text{nm})$	<b>pulse duration</b> $\tau(\text{fs})$	<b>power/energy</b>	<b>rep. rate (Hz)</b>
seed laser	775	150	5 mW	39 MHz
compressor	775	170-200	0.5 mJ	$\leq 10$ Hz

Table 4.1: Technical data of the CPA-10 fs laser system

doubled Nd:YAG laser. By switching a Pockels cell in the TRA resonator, the strongest pulse of the pulse train is sent towards the compressor. The duration of the output pulses can be adjusted by the grating rotation from 170 fs to a few ps. The repetition rate of the system is determined by the pump Nd:YAG laser. The spatial beam profile is close to TEM<sub>00</sub> Gaussian with 3 mm ( $1/e^2$ ) radius and the beam polarisation is horizontal at the exit from the laser. Without seeding, the regenerative amplifier produces 6 ns long pulses of similar energy, the wavelength and the spatial beam profile being the same as for the ultrashort pulses.

Precise timing is crucial in the ultrashort pulse laser experiments. Therefore, two delay generators with ps precision (DG535, Stanford Research Systems, Inc.) are used for the triggering of the components of the laser system and measuring equipment. The seed laser is used as a master trigger source: a fast photodiode illuminated by one part of the seed laser radiation delivers electrical impulses of 39 MHz repetition rate to the TRA's Pockels cell controller, where the rate is divided by a variable factor. This results in a 9.7 Hz repetition rate of the system, used for most of the experiments. The detailed triggering scheme is presented in Appendix B.

A very important issue is the suppression of the pre- and post-pulses. Pulses that precede the main pulse are heating the sample and can even create a pre-plasma if there is enough energy. That could change the surface reflectivity and therefore the absorption of energy of the main pulse. Instead of the fast heating described in Section 2.3, a slow temperature increase from the prepulses and the main pulse may result in gradual melting similar to the ablation with longer, nanosecond pulses. Heating of the plasma by high post-pulses should also be avoided.

As long as the Pockels cell is open, there is a train of pulses in the TRA, following 10 ns one after another (10 ns being a roundtrip time of the TRA resonator). When seeded with the pulses coming from the stretcher, most of the energy is extracted into the short pulses, and the ns background in a well adjusted amplifier is suppressed. By "closing" the Pockels cell, the pulse that passes through will not run further in the resonator, but will be sent to the compressor. Cutting the pulse train at one pulse after the maximum ensures the optimal energy



extraction from the regenerative amplifier with high stability. Fine adjustment of the Pockels cell position and timing enables good extinction of pre- and post-pulses, with an extinction ratio for pre-pulses of up to 500:1 and for post-pulses 100:1. When focused to a  $10^{-5}$  cm<sup>2</sup> area, 200 fs pulses of 500  $\mu$ J have a peak intensity of the order of 100 TW/cm<sup>2</sup>. It is clear that pre-pulses of 100 GW/cm<sup>2</sup> could precondition the sample and have an influence on the experiment.

#### 4.1.2 Pulse and beam diagnostics

Pulse duration is measured by the intensity autocorrelation technique. The second harmonic generation results in a symmetrical signal so that in order to obtain the real pulse duration one has to assume the temporal shape of the pulse. For Gaussian shape

$$e^{-(t/T)^2} \quad FWHM = 2\sqrt{\ln 2}T$$

the autocorrelation function has the form

$$e^{-1/2(t/T)^2} \quad FWHM = 2\sqrt{2 \ln 2}T.$$

The FWHM autocorrelation time has to be divided by 1.4142 to get the pulse width and the minimal time bandwidth product ( $\Delta t \Delta \nu$ ) equals 0.4412.

Throughout the experiments described in this thesis, the autocorrelation time was between 190 and 250 fs, corresponding to pulse lengths of 135 to 180 fs. The pulse prolongation due to the dispersion of optical elements in the experiments is estimated to be less than 10 fs [58].

The spatial beam profile is measured by a thermoelectrically cooled CCD camera (TE/CCD 1024-EBUV1, Princeton Instruments, Inc.) with a mechanical shutter. Each pixel is 25  $\mu$ m long and wide and there are 256x1024 pixels.

Pulse energy is measured with the pyroelectric sensor LM-P2-09 coupled to a powermeter (Fieldmaster, Coherent Inc.). The pulse to pulse stability in laser energy was highest (5% - 12%) at the maximum repetition rate of the pump Nd:YAG laser (10 Hz).

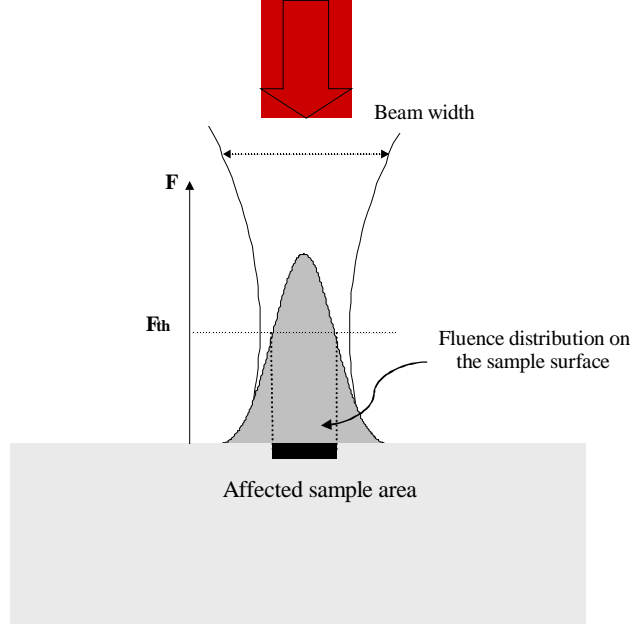


Figure 4-1: The Gaussian laser beam focused close to the sample surface and the fluence distribution on the surface. The bold line indicates the affected area which corresponds to fluences higher than the threshold fluence  $F_{th}$ .

#### 4.1.3 Determination of the focused beam area and threshold fluence

An important quantity for characterisation of a laser ablation process is the fluence (pulse energy per area,  $J/cm^2$ ). The area of a Gaussian beam in the vicinity of the focus plane changes strongly- quadratically with the distance along the beam propagation. For the focal lengths of the lenses used in the experiments (75.6 mm - 200 mm) the Rayleigh range is of the order of only 100  $\mu m$ . Therefore, the area of the beam in the plane of the sample surface has been measured for every experiment, using the following procedure [59, 60]. A beam with a Gaussian fluence distribution

$$F(r, \varphi) = F_0 \exp\left(-\frac{2r^2}{r_0^2}\right) \quad (4.1)$$

will induce damage to the sample surface wherever the local fluence is higher than a threshold fluence value (Figure 4-1). The damage radius is determined by

$$F_{th} = F_0 \exp\left(-\frac{2r_{th}^2}{r_0^2}\right), \quad (4.2)$$

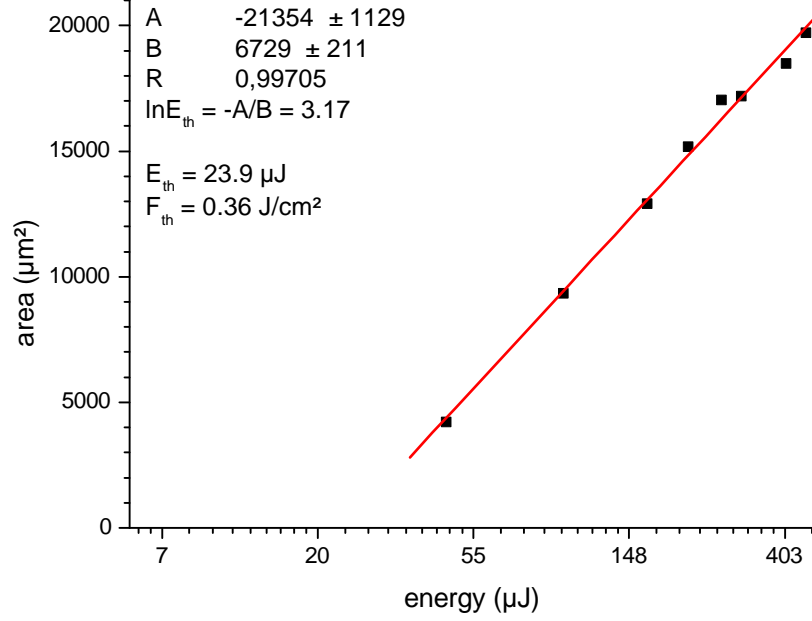


Figure 4-2: Determination of the threshold fluence from the dependence of damaged areas on laser pulse energy. A and B are the coefficients of the linear fit when the energy is plotted on a ln scale (see text); R is the correlation coefficient.

from which it follows for the damaged area

$$r_{th}^2 \pi = \frac{r_0^2 \pi}{2} \ln F_0 - \frac{r_0^2 \pi}{2} \ln F_{th}. \quad (4.3)$$

Since the peak fluence,  $F_0$ , is proportional to the measured total energy of the pulse

$$E = \iint d\varphi dr F(r, \varphi) = F_0 \frac{r_0^2 \pi}{2}, \quad (4.4)$$

the beam size on the sample surface and the threshold fluence can be determined by measuring the energy dependence of the damaged area as illustrated in Figure 4-2. When the area is plotted against  $\ln E$ , the slope B of the line equals  $\frac{r_0^2 \pi}{2}$  and the intercept  $A = -\frac{r_0^2 \pi}{2} \ln E_{th}$ . (Note that  $\ln E$  is a dimensionless quantity so that the line coefficients A and B are expressed in the same units as the area;  $F_{th} = \frac{E_{th}}{B}$ .) The values of the threshold fluences for different materials and fluences used for different experiments were determined by visual inspection of the craters. The criterion for the damaged area was the visibility of a surface modification applying an

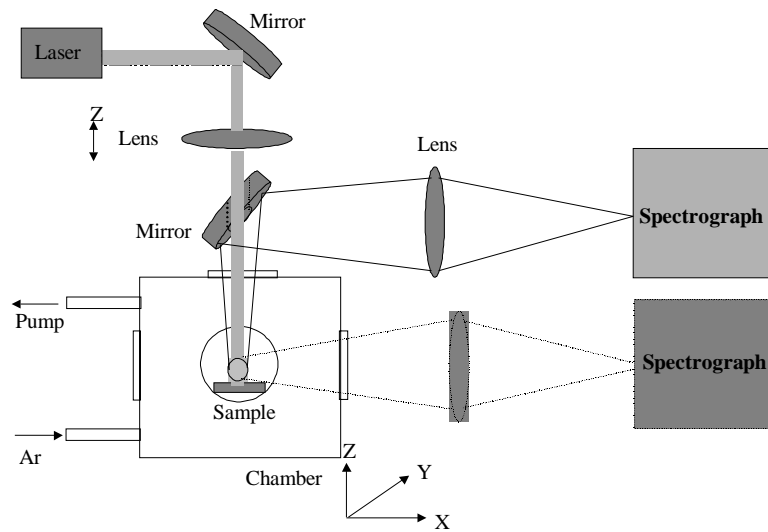


Figure 4-3: Scheme of the experimental arrangement for LIBS measurements. The laser ablation plasma can be imaged on the spectrograph in a side-view or in a top-view configuration. In the latter case a pierced mirror is used.

optical microscope.

## 4.2 LIBS

The ablation chamber with fused silica windows was mounted on  $\mu\text{m}$ -precision translation stages to allow a three axis positioning of the sample with respect to the laser beam. The laser beam was delivered to the sample with normal incidence through a plano-convex lens of 75.6 or 100 mm focal length. The focusing lens was mounted on the chamber holder so that the focusing conditions can remain unchanged when the chamber is translated in  $z$  direction. The distance between the lens and the sample could be adjusted with an additional  $\mu\text{m}$ -precision translation stage. Typically, argon was used as the ambient gas and the obtainable pressure range was 0.01 - 1000 mbar.

The emitted light was collected from the side or from the top (Figure 4-3) and directed to the spectrometer. Early experiments were conducted using a *Czerny-Turner grating spectrophotometer*

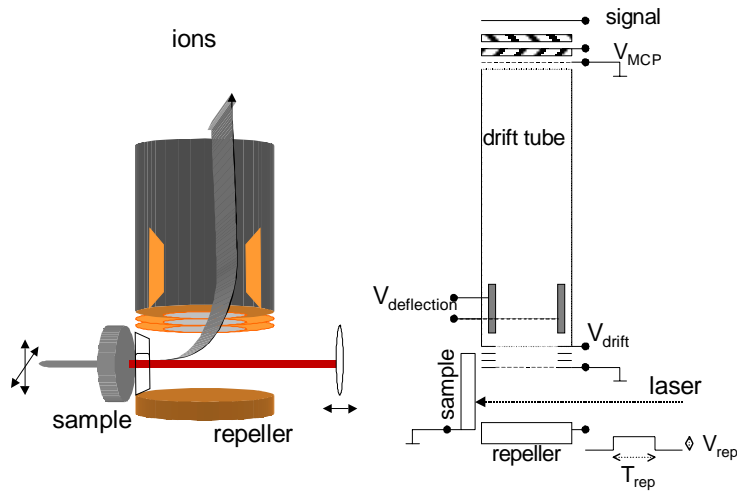


Figure 4-4: Experimental arrangement for the LA-TOF-MS measurements. (a) 3D view of the lower part of the instrument: the sample holder (movable in two directions), the horizontal slit, the repeller plate, the grids with accelerating voltage ( $V_{drift}$ ) and the deflection plates at the beginning of the drift tube, the incident laser beam and the ion trajectories. (b) Electrical connections.

(2400 grooves/mm, spectral range 220-650 nm, reciprocal linear dispersion  $\sim 0.4$  nm/mm at 400 nm). A POSMA (Spectroscopy Instruments, Germany) image-intensified photodiode array (IPDA with 1024 pixels,  $0.025 \times 5$  mm<sup>2</sup> per pixel, spectral interval 10 pm/pixel) was used for the time resolved spectral detection.

Alternatively, an *Echelle spectrograph* (ESA 3000, LLA GmbH, Berlin, Germany) was used for spatial and temporal mapping of atomised elements in the plasma by laser induced fluorescence (LIF) and for some LIBS measurements. It allows a simultaneous detection of the spectral range from 200 to 780 nm, having the linear dispersion of 0.005 nm/pixel (at 200 nm) and 0.019 nm/pixel (at 780 nm).

### 4.3 TOF-MS

The time-of-flight mass spectrometer is shown schematically in Figure 4-4. It is a linear TOF-

drift tube length	500 mm	repeller voltage	250-500 V
sample to tube axis	40 mm	repeller pulse duration	4-20 $\mu$ s
laser beam to 1 <sup>st</sup> grid	14 mm	delay laser pulse- repeller	1-5 $\mu$ s
repeller to 1 <sup>st</sup> grid	27 mm	typical drift voltage	-750 V
acceleration region	15 mm	deflection	300-400 V
deflection plates size	30×30 mm	MCP voltage	-2.4 kV
deflection plates distance	30 mm	ADA-100 card's time resolution	10 ns
focusing lens	200 mm	maximum accumulation time	44 $\mu$ s
pressure	10 <sup>-6</sup> mbar	mass resolution at A/Z=65	300

Table 4.2: Technical data of the time of flight mass spectrometer (ISAS Berlin).

MS device with a two stage micro-channel plate (MCP) detector (Chevron<sup>TM</sup>, Galileo Corp.), developed at ISAS-Berlin. Laser ablation is performed in the TOF high vacuum chamber. No post-ionisation is used. With the analogue data acquisition mode a complete mass spectrum of the sample can be obtained from a single laser shot. The sample is placed vertically at the side of the entrance to the drift tube. The laser beam is focused at normal incidence. A narrow horizontal slit in front of the sample reduces the dispersion of the ion beam in the direction along the drift tube, contributing to a better mass resolution. The technical data are summarised in Table 4.2. All voltages and delays have to be optimised for each sample and for the specific ablation conditions.

A positive rectangular voltage pulse that pushes the ions upwards into the drift tube is given to the repeller plate some microseconds after the laser incidence on the sample. The ions that are passing the positively charged repeller plate are deflected to the 1<sup>st</sup> grounded grid and enter the short acceleration region. The last grid in that region is on the potential of the drift tube,  $V_{drift}$ . The total change of the kinetic energy of the ions in the vertical direction equals the sum of potential energies of the two fields, repelling and accelerating. The tube itself is a field free zone (in the vertical direction) in which the separation of the ions with different mass/charge ratios takes place. The electric field between the deflection plates, placed at the beginning of the drift tube, works against the initial, horizontal motion of the ions. The ions created in the ablation process have a very broad energy distribution (see Section 5.3). Only a small portion of these ions is detected. The deflection field strength determines which ions will reach the detector at the top of the tube. The dynamic range of the MCP detector is about

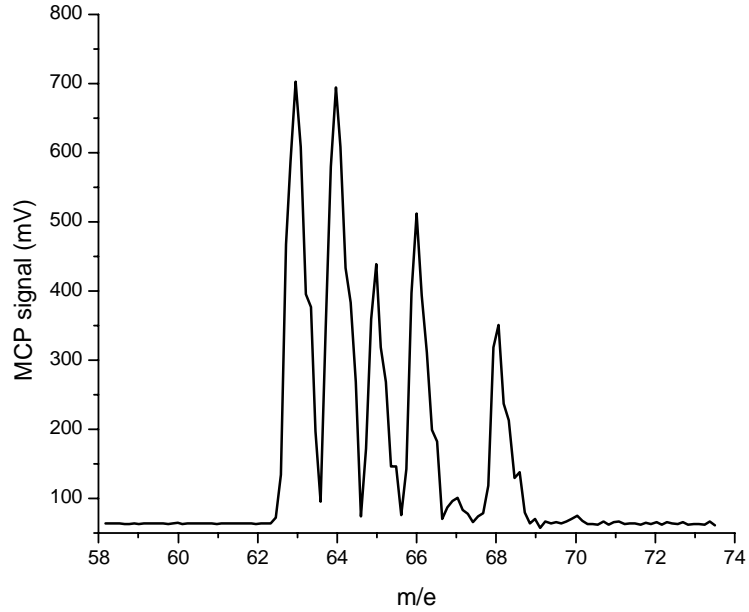


Figure 4-5: TOF mass spectrum of brass. Cu isotopes 63 and 65 and Zn 64, 66, and 68 are well resolved. Fluence  $0.3 \text{ J/cm}^2$ , signal accumulation 20 shots (surface precleaned with 80 shots),  $V_{rep} = 350 \text{ V}$ ,  $V_{drift} = 750 \text{ V}$ ,  $V_{defl} = 360 \text{ V}$ ,  $T_{delay}(\text{rep-fs}) = 2 \mu\text{s}$ .

100, but the amplification can be slightly adjusted by changing the potential of the second stage ( $\pm 50 \text{ V}$  effectively). Well resolved mass spectra can only be obtained for low laser fluences. A high fluence pulse produces too many ions which saturate the detector, higher charged ions are created and peaks of different species merge. An example of well resolved copper and zinc isotopes from the ablation of a brass sample is shown in Figure 4-5.

The ion emission has been studied in a configuration without the repeller (Figure 4-6). The sample was placed directly underneath the drift tube and the laser beam was focused on the sample surface with p-polarisation. The angle of incidence was  $\alpha = 57^\circ$ . The arrival time of the free flying ions was measured (with only the MCP voltage and without the drift voltage applied), as well as the influence of different drift voltages on the MCP signal.

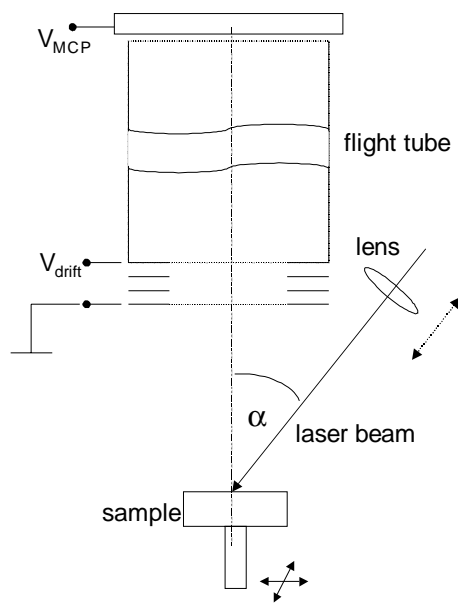


Figure 4-6: The TOF instrument without the repeller. Samples are placed directly below the drift tube and the laser beam is incident at an angle  $\alpha$ . The drift voltage may or may not be applied.



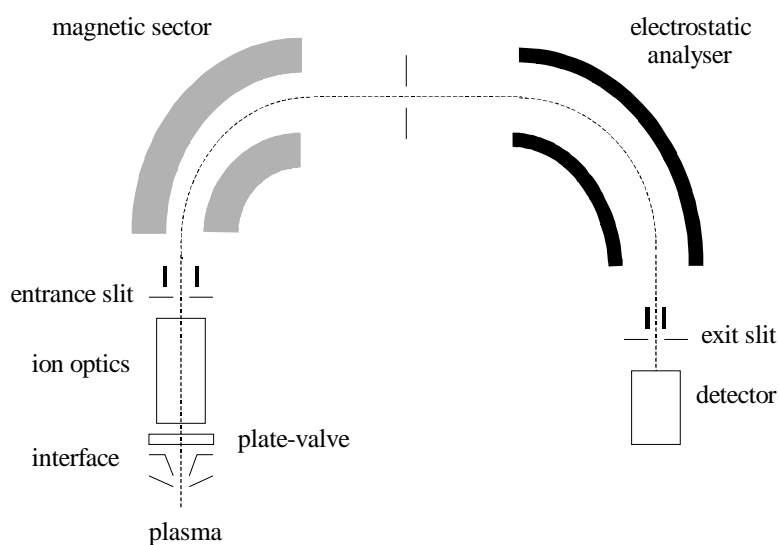


Figure 4-7: Scheme of the ICP- mass spectrometer.

#### 4.4 ICP-MS

ICP-MS is one of the most powerful techniques for elemental analysis. Element concentrations in ppb to ppt range can be detected. Femtosecond laser ablation inductively coupled plasma mass spectrometry (LA-ICP-MS) measurements were performed with a high resolution mass spectrometer, the prototype of the ELEMENT (Finnigan MAT, Bremen) [61-64]. It is a double focussing sectorfield apparatus in inverted Nier-Johnson geometry, where the ions from ICP, after passing through the ion optics, enter the magnetic sector first, and then pass through the electrostatic analyser (Figure 4-7). Samples were placed in a cylindrical teflon chamber with a quartz window at the top. The laser beam was focused with a 200 mm focal length lens. The ablated particles were transported in a gas stream through a polyethylene tube into the ICP-MS. Following the works of Günther et al. [65, and references therein], helium was used as the carrier gas and argon was added downstream from the ablation cell (Figure 4-8). The ICP power was 1250 W.

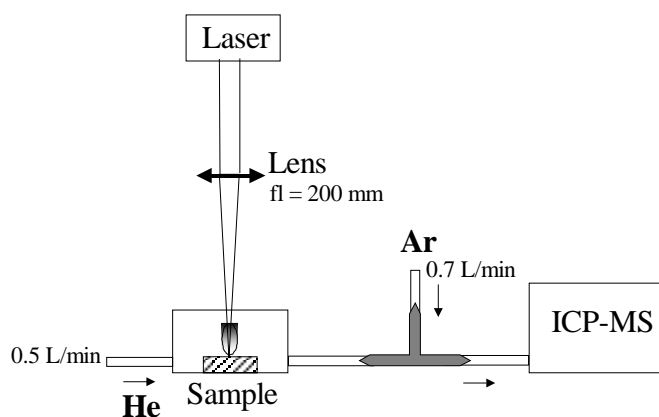


Figure 4-8: Arrangement for LA-ICP-MS measurements.

## 4.5 LIF

Being a very fast process (typically 10 ns), the laser induced fluorescence provides an excellent temporal resolution for studying the dynamics of fast transient plasmas, much better than what is achievable with most of the gated devices. Spatial resolution can be achieved by collimating the beam of the tunable laser that induces the fluorescence.

The experimental arrangement for LIF measurement on femtosecond induced plasmas is shown in Figure 4-9. A copper sample containing 298 ppm magnesium was placed in the ablation chamber filled with argon. The ambient pressure ranged from 0.02 to 1000 mbar. The normally incident fs laser beam was crossed by a collimated dye laser beam, parallel to the sample surface. The dye laser parameters are summarised in Table 4.3. If the dye laser is tuned to a transition wavelength of atoms/ions present in the plasma, fluorescence is observed in the intersection volume of the plasma with the dye laser beam. This volume is imaged to the entrance of the input fiber of the echelle polychromator, at 90 degrees to both laser beams. Vertical displacement of the sample chamber (without change in the fs- laser focusing conditions) allows probing of different plasma regions. A polariser serves to reduce the intensity of vertically

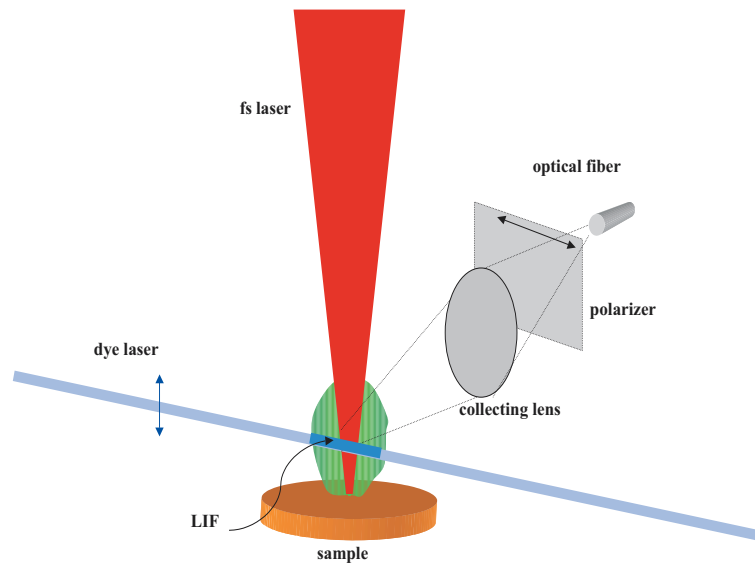


Figure 4-9: Arrangement for laser induced fluorescence measurements.

laser	Cobra-Stretch-GA, Sirah
grating	single, $2400 \text{ mm}^{-1}$
pump laser	Nd:YAG (Continuum); 532 nm
dye/ wavelength range	Rhodamine 6G (558-588 nm)
doubling crystal	KDP
output wavelength	279-294 nm
pulse duration	9 ns
energy	$\leq 13 \text{ mJ}$
diameter of collimated beam	0.2 mm

Table 4.3: Dye laser technical data

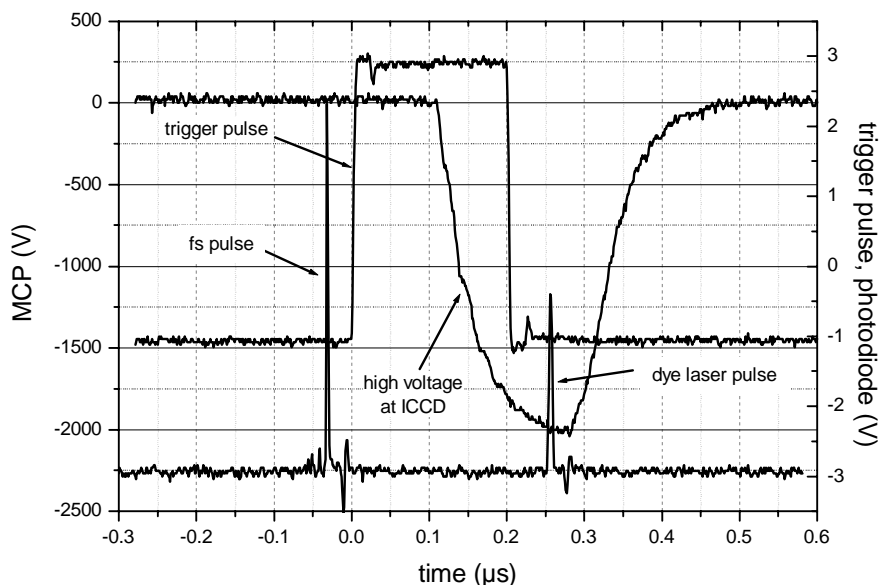


Figure 4-10: A time sequence of the pulses in LIF experiment: the fs laser pulse is followed by the dye laser pulse (variable delay). The trigger pulse for the echelle ICCD detector is timed in such a way that the maximum MCP amplification coincides with the dye laser pulse.

polarised scattered light that reaches the detector. This is necessary when the fluorescence of the pumped line is measured. Based on the scattered light intensity, interesting conclusions about the size distributions of ablated particles can be drawn (Section 5.2.1).

For the optimal signal to noise ratio, the dye laser pulse immediately followed by LIF signal has to coincide temporally with gate of the echelle ICCD detector. Simultaneously, the gate of the detector has to be as short as possible in order to reduce the contribution of plasma emission to the total signal. This is especially important at small delays after the fs pulse. As illustrated in Figure 4-10, the optimal gate pulse duration is 200 ns. The maximum of the high voltage response overlaps with the dye laser pulse. Changing the delay between the ablating fs-laser and the dye laser, results in a series of time of flight measurements for several heights above the sample. The temporal precision is limited by a jitter of  $\pm 25$  ns inherent to the fs-laser system (see page 134). For each measurement the light of 40 pulses was accumulated, after the sample surface was cleaned by the same number of pulses. At least three different heights above the sample surface were probed for each argon pressure. The power of the dye laser was

adjusted to about 70% of the optical saturation of the transition studied. The absolute values of the used power differed considerably for different pressures.

## 4.6 Microscopes

For the visual inspection of laser craters an optical microscope with 16x magnification and a scanning electron microscope (SEM) were used. Crater depths were measured by a scanning white light interferometer (New View 5000, produced by Zygo Lot). It measures microstructure and topography of surfaces in three dimensions. Equipped with a 20x Mirau objective, the system has a magnification of 400x. The numerical aperture is 4.7, lateral resolution  $0.88 \mu\text{m}$ , the field of view  $0.35 \times 0.26 \text{ mm}^2$ , and the depth resolution is few nanometres.

## Chapter 5

# Basic Investigation of Ultrashort LA

### 5.1 Crater morphology

Exploring the morphology of the crater can give the first insight into the laser ablation process. The structure of the crater depends on the material properties, pulse duration, energy and wavelength of the laser, the ambient conditions, and the number of the pulses applied. In this thesis, the ultrashort laser ablation of metals and semiconductor materials was investigated. There is a striking difference between the craters obtained with sub-picosecond and nanosecond laser pulses. Figure 5-1 shows two craters in a brass sample created by 45 pulses each, the same focusing geometry and at 40 mbar argon pressure with the (a) 200 fs laser pulses (775 nm,  $0.7 \text{ J/cm}^2$ ); and (b) 6 ns laser pulses (775 nm,  $2.7 \text{ J/cm}^2$ ) [55]. In each case, the fluences were about 2-3 times larger than the threshold fluence. While the ns-crater shows the typical structure of a re-solidified melt with a number of re-deposited droplets, the fs-crater has a well-defined brim, and shows only very small indication of melting. Another characteristic of the ns-craters, the elevated expulsion rim as seen in Figure 5-2, can be avoided when the ultrashort pulses are used. Smoother and better defined structures can be produced due to reduced thermal diffusion effects (determined by the electron diffusion) and the nature of the phase transition (Chapter 2) [7, 8, 23, 67].

The crater bottom has a very fine structure which can considerably vary if the experimental conditions are changed. Figure 5-3 shows the details of two craters in a copper sample as seen by the SEM (magnified 10000 times): (a) the bottom of a single shot crater ( $7.4 \text{ J/cm}^2$ , 0.6

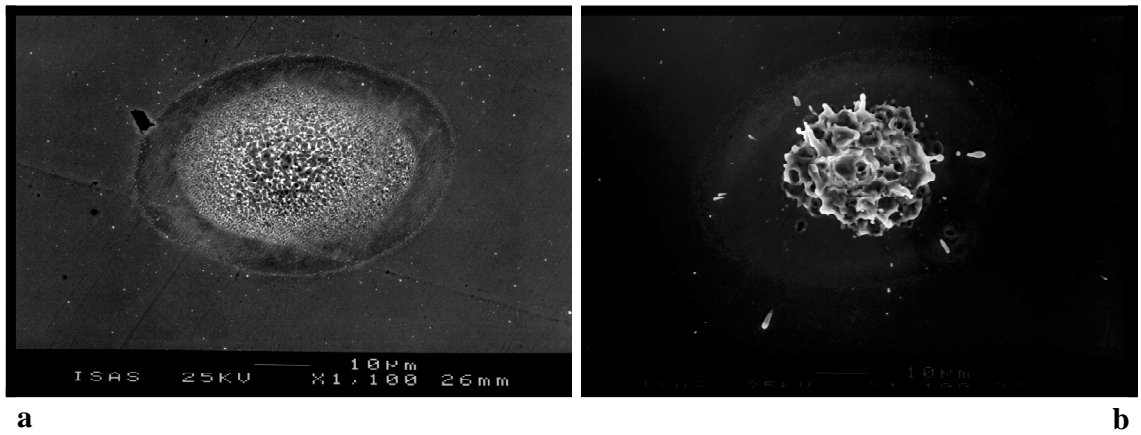


Figure 5-1: Laser craters on a freshly polished brass sample surface: (a) after 45 pulses with the 200 fs laser ( $0.7 \text{ J/cm}^2$ ); and (b) after 45 pulses with the 6 ns laser ( $2.7 \text{ J/cm}^2$ ). The ablation was performed in Ar ( $p= 40 \text{ mbar}$ ).

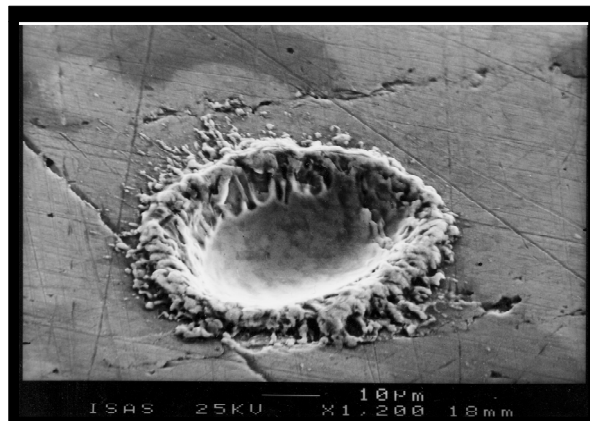


Figure 5-2: 6 ns-laser crater on polished copper surface created in an argon ambient (140 mbar) with 10 pulses of  $30 \text{ J/cm}^2$  fluence.

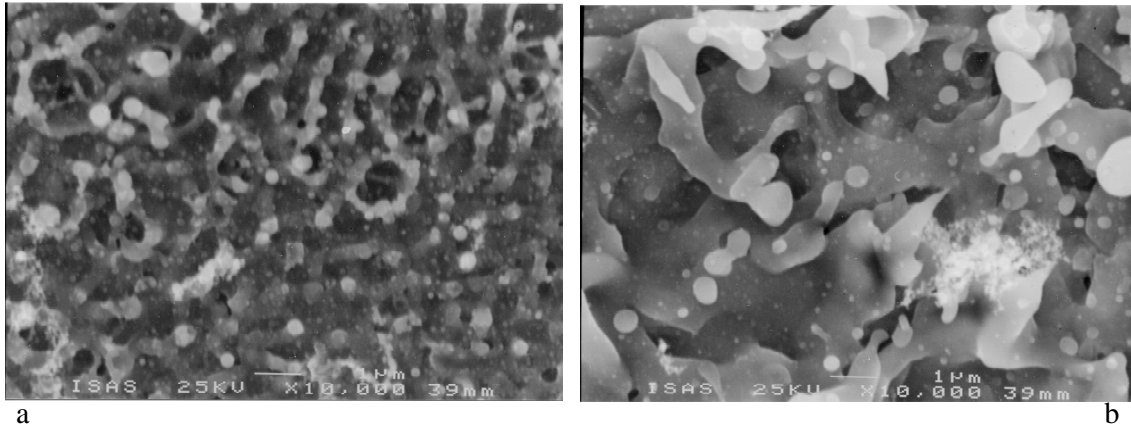


Figure 5-3: Details of the two craters in a copper sample as seen by the SEM (magnified 10000 times): (a) the bottom of a single shot crater and (b) details of the 77-shots crater, both created by  $7.4 \text{ J/cm}^2$ , 0.6 mbar Ar, 200 fs laser pulses.

mbar Ar, 200 fs); and (b) details of the 77 shots-crater ( $7.4 \text{ J/cm}^2$ , 0.6 mbar Ar, 200 fs). Fine, sub-micrometre shapes that can be observed in Figure 5-3 a, become larger when multiple pulses are applied on the same surface (Figure 5-3 b). The roughness of the crater bottom increases.

At certain conditions, ripple structures are formed on the crater surface. Examples of the ripple structures formed after 200 fs laser irradiation are shown in Figure 5-4: (a) TiAlN/TiN sample, 400 pulses,  $0.6 \text{ J/cm}^2$ ; and (b) the edge of the crater on Cr-film on silicon, 40 pulses,  $2.2 \text{ J/cm}^2$ . The Ar pressure was 40 mbar in both measurements. The spots on Figure 5-4 (a) are sample imperfections- areas of enrichment of certain trace elements.

The ripples are often oriented perpendicularly to the incident electric field direction. If their periodicity is of the order of the laser wavelength they can be attributed to interference effects [13, 60, 66, and references therein].

### 5.1.1 Ablation rate and threshold fluence

The depths of craters created in a polished copper sample ("Cu424") at vacuum conditions (0.05 mbar) were measured with the white light interferometer in order to calculate the ablation rates. The crater shape reflects the exact fluence distribution across the beam, the deepest point being at the place of the fluence maximum.



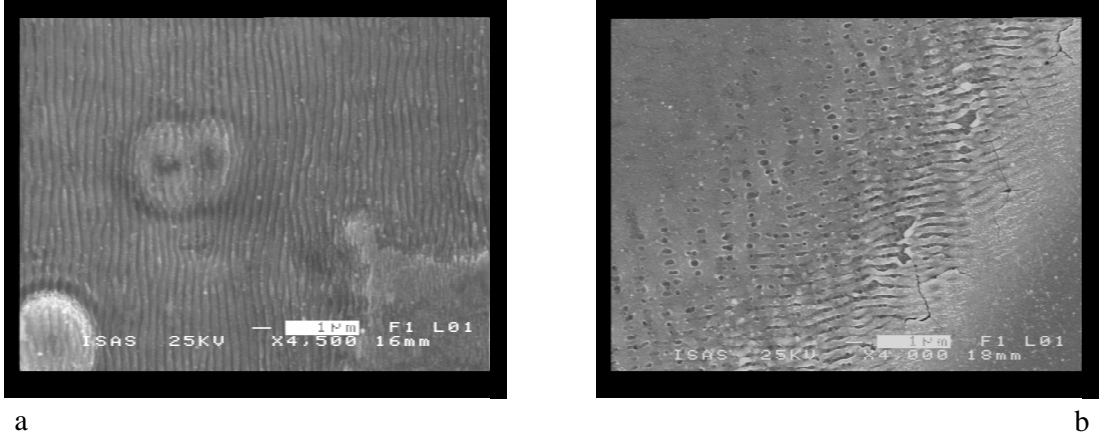


Figure 5-4: Ripple structures formed after 200 fs laser irradiation: (a) TiAlN/TiN sample, 400 pulses,  $0.6 \text{ J/cm}^2$ ; and (b) the edge of the crater on Cr-film on silicon, 40 pulses,  $2.2 \text{ J/cm}^2$ .

In these measurements, the laser focus was 2 mm below the surface, excluding the possibility of inducing a plasma breakdown in the gas above the sample. The beam radius ( $1/e^2$ ) at the sample surface was  $60 \mu\text{m}$ . In Figure 5-5 the maximum crater depth is shown as a function of the number of shots for different fluences. The ablation depth grows linearly with the number of pulses applied. The ablation rate (nm/pulse) for each of the applied fluences is shown in Figure 5-6, where the abscissa has a logarithmic ( $\ln$ ) scale. In this fluence range ( $F > 0.8 \text{ J/cm}^2$ ) the slope  $l$  of the logarithmic dependence

$$L \simeq l \ln \frac{F}{F_{th}}$$

is the effective electronic heat penetration depth (Section 2.2). Extrapolation of the linear fit in Figure 5-6 to the zero ablation rate yields the threshold fluence  $F_{th}$ . From the fit, the values  $l = (53 \pm 4) \text{ nm}$  and  $F_{th} = (0.40 \pm 0.05) \text{ J/cm}^2$  are obtained.

These results can be compared to the measurements by Nolte *et al.* [8]. They estimated  $l$  from the material properties to amount  $60 - 80 \text{ nm}$ , and reported the values of  $l = 80 \text{ nm}$  and  $F_{th} = 0.46 \text{ J/cm}^2$  for measurements with 150-fs 780 nm pulses on a polycrystalline 1-mm-thick copper foil at  $10^{-4} \text{ mbar}$ . They also observed that the ablation rate is independent of the laser pulse duration from 150-fs to 5 ps.

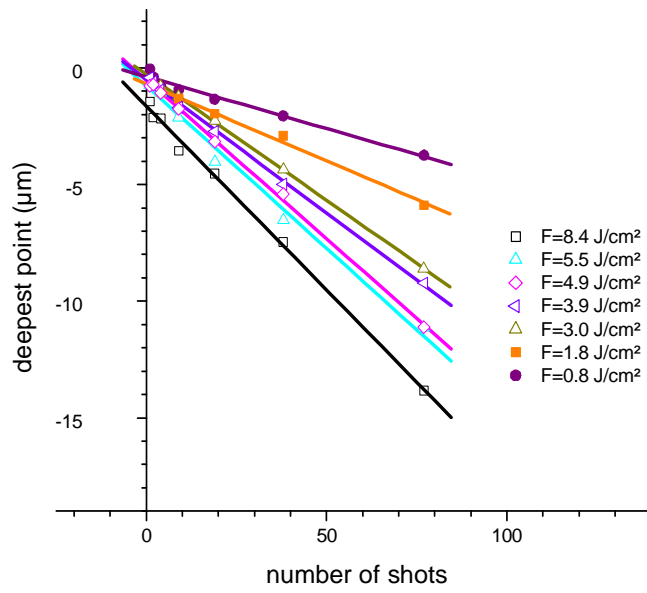


Figure 5-5: Depths of craters on copper sample measured with white light interferometer for different numbers of applied pulses and different laser fluences. The argon ambient pressure was 0.06 mbar.

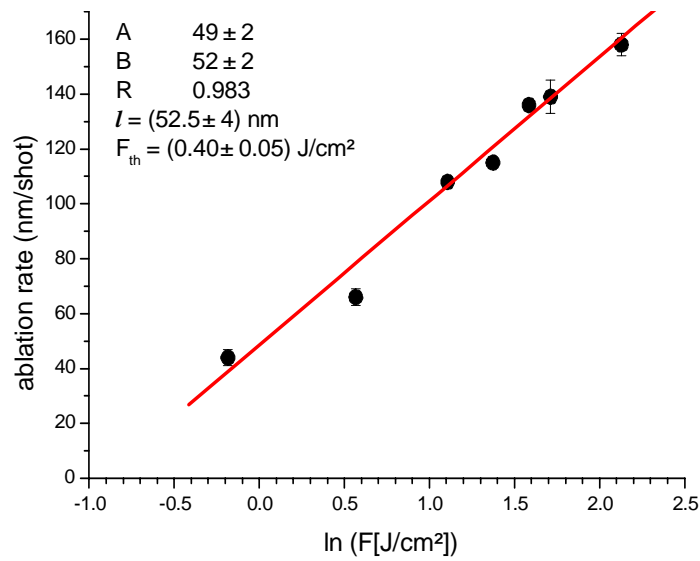


Figure 5-6: The ablation rates calculated from the measurements in Figure 5-5 plotted against the logarithm of fluence. A and B are the coefficients of the linear fit and R is the correlation coefficient.  $l$  is the electronic heat penetration depth and  $F_{th}$  is the threshold fluence (see text).

There are several factors that might contribute to the difference between the two measured results for the electron heat penetration depth  $l$ . If the pressure dependence of the ablation rate (see Section 5.1.2) is extrapolated to  $10^{-4}$  mbar, the heat penetration depth increases for 3 nm. The differences in sample properties might have an additional effect: the sample "Cu424" contains 0.3 % impurities of 15 elements in concentrations from 1 to 370 ppm, and it can be expected that its electrical resistivity is slightly higher than for the pure copper investigated in [8]. It can be shown that the electron heat penetration depth  $l$  is inversely proportional to the resistivity (see Section 6.1.2 and eq. 6.9). The electron heat penetration depth measured here is indeed lower than for the pure copper, in consistence with equation 6.9. However, the main reason for this discrepancy is probably due to the accuracy of the depth determination by optical microscopy used in [8]. Accurate depth measurement of craters with 25-75  $\mu\text{m}$  diameter and 20 to 30  $\mu\text{m}$  depth is rather difficult. The white light interferometer gives more accurate results.

The small differences in the threshold fluence can also be expected since  $F_{th}^l = \rho\Omega l$  (eq. 2.4). The value obtained here for the sample "Cu424" of  $(0.40\pm 0.05)$  J/cm<sup>2</sup> is smaller than 0.46 J/cm<sup>2</sup> reported in [8].

In the measurements described above, the depth was proportional to the number of applied pulses. As the aspect ratio of the crater (depth/diameter) becomes higher, the ablation rate drops. That is mainly due to the lower efficiency of the material expulsion and the enlargement of the energy absorbing area. These effects are significant for depths of 100  $\mu\text{m}$  or more, and were not relevant for the investigations presented in this thesis [67, 68].

When the threshold fluence is determined from the damaged area, as described in Section 4.1.3, another interesting aspect of the ablation process is revealed. The threshold fluence is lower for a higher number of pulses on the same spot, indicating the existence of a damage accumulation process. Figure 5-7 shows a semi-logarithmic plot of crater areas for several numbers of laser pulses, depending on the pulse energy. The crater area increases with the number of successive pulses. As given by eqs. 4.3 and 4.4, the slope of the lines is proportional to the beam area, and the intercepts with the  $\ln E$  axis determine the threshold energies. The threshold fluence dependence on the number of pulses can be presented in an accumulation plot. The accumulation plot is a plot of the accumulated fluence  $N * F_{th}(N)$  against the pulse

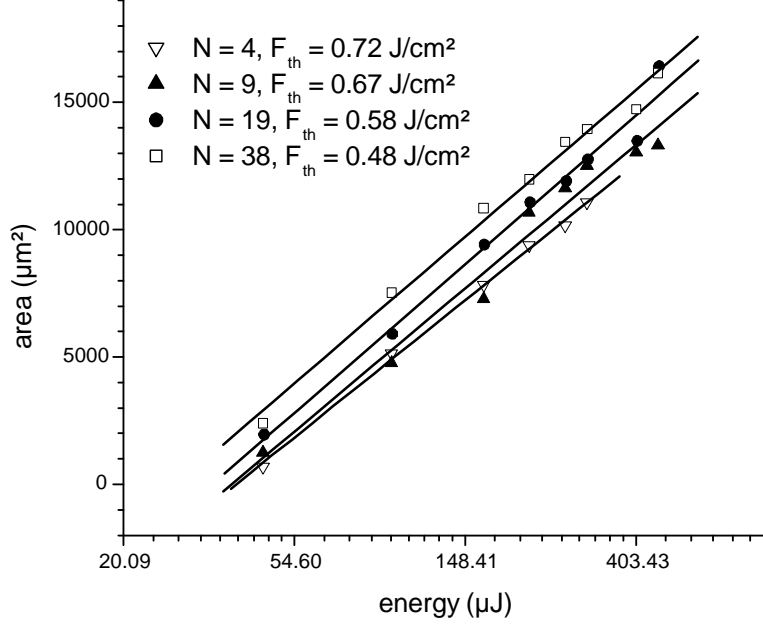


Figure 5-7: Crater areas in dependence on pulse energies for different numbers of the applied pulses ( $N$ ). Copper sample at low argon pressure of 0.06 mbar.

number  $N$  on logarithmic scales. One of these plots is shown in Figure 5-8. The slope of the accumulation plot represents the exponent in the relation

$$N * F_{th}(N) \sim N^B.$$

If the slope of this plot equals 1, there are no accumulation effects and the threshold fluence is equal for any number of pulses. The values greater than 1 indicate hardening of the material, and smaller than 1 are a sign of the damage accumulation. Jee et al. discussed this effect for Cu and Al monocrystals exposed to the repeated nanosecond laser irradiation and they have explained it as a plastic strain accumulation [69]. The induced stress amplitude  $\sigma$  is proportional to the temperature variation  $dT$

$$\sigma = -E\alpha \frac{dT}{1 - \nu}.$$

$E$  is here Young's modulus,  $\alpha$  is the thermal expansion coefficient, and  $\nu$  is Poisson's ratio.

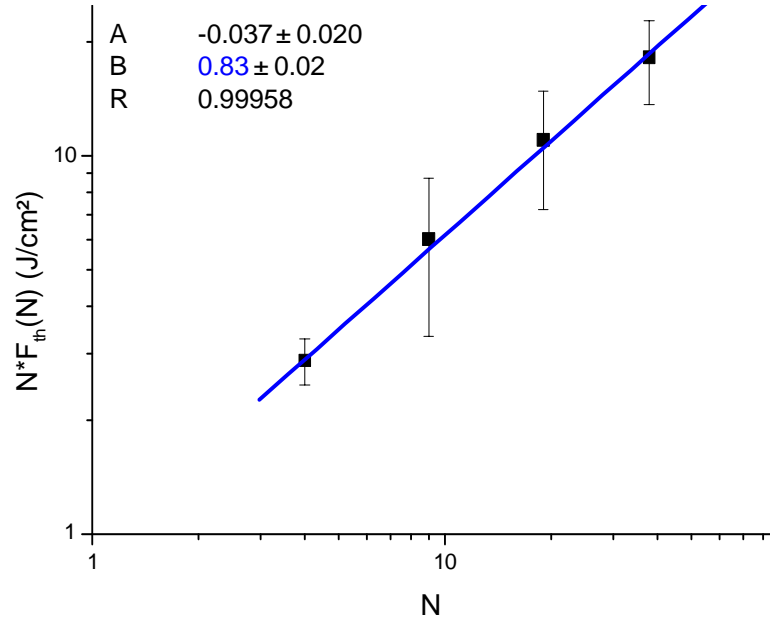


Figure 5-8: The accumulation plot (see text) for fs laser ablation of copper sample at 0.06 mbar Ar pressure. A and B are the linear fit coefficients and R is the correlation coefficient.

If this amplitude is bigger than a plastic yield point, a plastic strain will be produced. The temperature change can be approximated by the attainable lattice temperature  $T_i$  from the two-temperature model. For the "Cu424" sample, the slope of the accumulation plot is equal to  $0.83 \pm 0.02$ . That is lower than the values reported in [69] and [70] for ns ablation which vary between 0.85 and 0.95 (depending on the surface crystallographic orientation), but within the limits of the fatigue theory of metals [71].

It should be mentioned that the threshold determination from the extrapolation of the crater area measurements is limited by the power of the microscope used and the judgement of the investigator on the borders of the visible damage area. In this sense, the threshold determination from the ablation rates is more accurate, also because the depth resolution of the white light interferometer (5 nm) is much better than the lateral resolution (500 nm). Nevertheless, the area method is important in the routine measurements for determination of the laser beam area on the sample surface and for the fluence calculation.

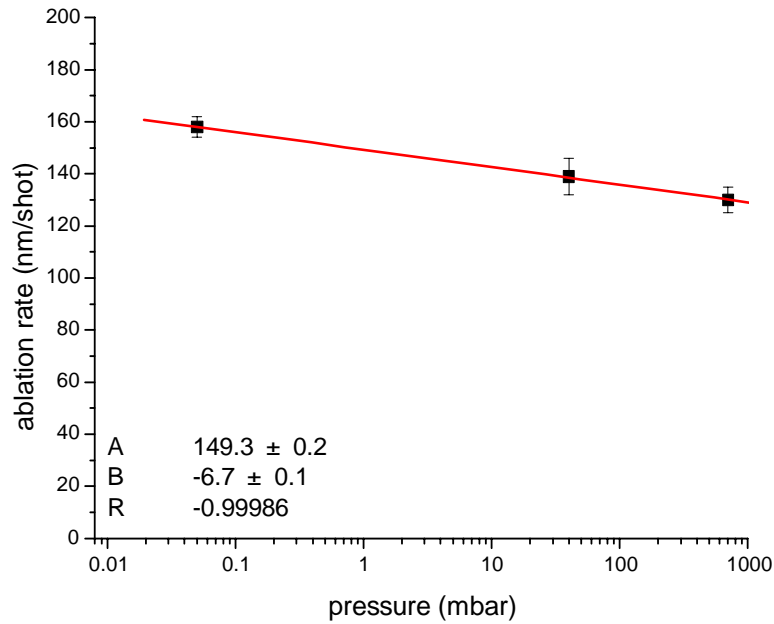


Figure 5-9: The pressure dependence of the femtosecond ablation rate of copper. Note the log scale of the abscissa. A and B are the coefficients of the linear fit ( $y=A+Bx$ ) and R the correlation coefficient.

### 5.1.2 The influence of ambient pressure on the ablation rate

An increase of the ambient pressure causes a decrease of the ablation rate. Figure 5-9 shows the decrease of the ablation rate of copper for  $8.4 \text{ J/cm}^2$  in argon atmosphere for pressures of 0.05, 40 and 700 mbar. Inspection of craters with the SEM reveals much more debris around the craters with higher pressure, as seen in Figure 5-10. The two craters were created by the same number of pulses of the same fluence under two different ambient pressures of argon gas: (a) 0.06 mbar, and (b) 700 mbar.

## 5.2 Laser ablation plasma properties

An important part of the laser ablation process is the creation of a small, transient plasma above the sample surface that can be studied by spectroscopic methods. The plasma dynamics depends on the ambient conditions, the sample properties, and the laser parameters: wavelength, energy and pulse duration. Its contents are atoms, ions and electrons as well as droplets and clusters.

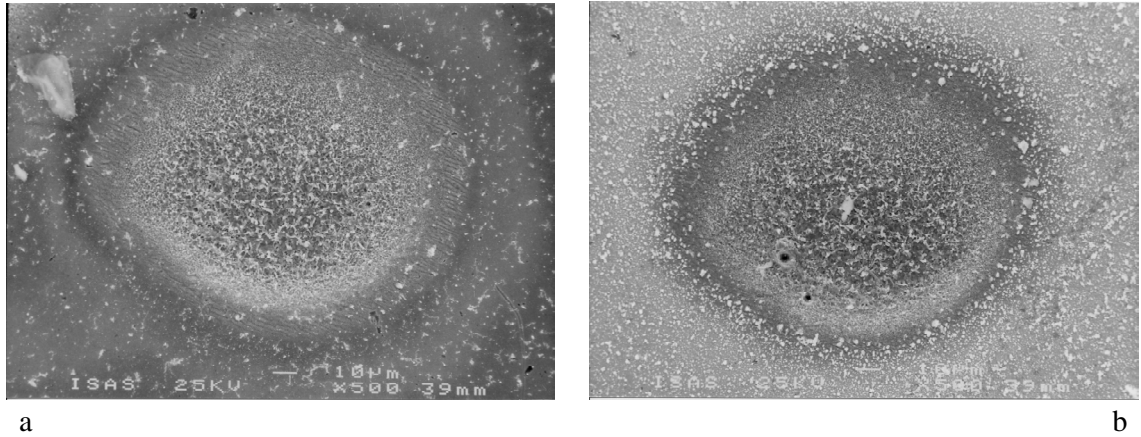


Figure 5-10: Craters created by 77 pulses (200 fs, 775 nm, 7.4 J/cm<sup>2</sup>) on polished copper sample surface. The argon ambient pressure was (a) 0.6 mbar; (b) 700 mbar.

While the nanosecond laser ablation plasma has been a subject of many investigations in the past [3, 5, 29, 72-79], at the beginning of this project the femtosecond laser ablation plasmas (in the intensity range 10<sup>12</sup> - 10<sup>14</sup> W/cm<sup>2</sup>) were practically unexplored from the spectroscopic point of view. LIF, LIBS and direct TOF measurements were undertaken to study different aspects of their evolution. From the obtained results, the conditions for reliable analytical applications were deduced. Comparison of the LIBS spectra of plasmas induced by femtosecond pulses with those of more familiar nanosecond ones helped in understanding the underlying processes.

Unless vacuum conditions are required for a given analytical application, a noble gas should be chosen as the ambient gas in order to reduce the probability of chemical reactions with the sampled species. This choice will influence the plasma expansion dynamics and the diffusion properties of ablated particles. The ionisation energy and the plasma ignition threshold (laser intensity) are lower for argon than for helium and neon. The argon plasma temperature is therefore higher than the temperatures of the He and Ne plasmas induced by the same laser intensities [72, p. 37]. The choice of the other experimental parameters, such as the laser intensity, the ambient gas pressure, the delay and duration of the gate width for data acquisition will be discussed in later sections.

### 5.2.1 Laser Induced Fluorescence

For studies of plasma dynamics a technical copper sample was ablated under different conditions. Whereas the optical emission spectroscopy facilitates the monitoring of the population of excited atomic and ionic states, laser induced fluorescence can visualise atoms and ions in the ground state as well. Even a long time after the ablation, when the emission signal has died out, the plasma expansion can be followed by inducing the fluorescence.

#### Plasma expansion

After a large amount of laser energy has been applied almost instantaneously on a very small area ( $10^{-5}$  cm<sup>2</sup>), the material released through an explosion expands into a homogeneous gas atmosphere creating a shock wave and subsequently cooling down. As will be seen, the development of the plume front follows the predictions of the spherical expansion model presented in Section 2.4.

The plume expansion at different ambient gas pressures was studied employing the unique properties of the LIF technique: high temporal resolution given by the short duration of the fluorescence, spatial resolution determined by the excitation volume, and the ability to screen the species also in their ground state. The experimental setup and procedure are described in Section 4.5. The measurements were done for several argon pressures in the range from 0.01 mbar to 1 atm, covering the conditions in which the analytical applications of the laser ablation sampling are conducted [80].

The resonant fluorescence of copper atoms at 282.4 nm and magnesium ions at 279.6 nm was observed. Suitable copper ionic lines were out of the range of the dye laser as it was used in these experiments. The laser light scattered on the ablated particles and on the chamber walls is superimposed on the LIF signal. Its intensity can be determined by detuning the dye laser wavelength off resonance, as illustrated in Figure 5-11. It shows the LIF signals at  $p_{Ar} = 50$  mbar, 1.5 mm above the sample, and 3.6  $\mu$ s after the fs ablation pulse. The dye laser power was the same at both excitation wavelengths, as well as off-resonance. That off-resonance signal indicates the amount of light scattered mainly on the ablated particles that is detected despite the polariser. Without the polariser, the scattered intensity would completely hide the fluorescence signal. The pure emission signal obtained in such measurements is negligible due to



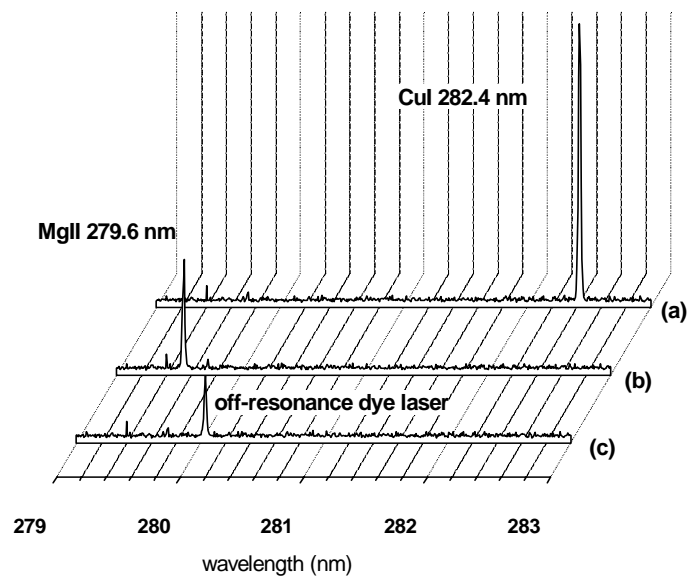


Figure 5-11: Spectra of the fs-laser produced plasma with the dye laser beam at the height of 1.5 mm above the sample. The dye laser energies at wavelengths of the (a) CuI, (b) MgII line, and (c) off resonance were the same. The fluorescence of Cu 282.4 nm and Mg 279.6 lines is superimposed to the background scattering. Argon pressure: 50 mbar. Delay between the fs pulse and the dye laser pulse: 3.6  $\mu$ s.

very short acquisition times and a low transmittance of the polariser (20% for the light linearly polarised in its polarisation direction and 0.5% for the perpendicular polarisation, at 280 nm). Even in the earliest moments after the start of ablation, when the plasma is very hot and the emission intensity at its highest (Section 5.2.2), it does not amount to more than 10% of the fluorescence.

Apart from the direct fluorescence of the Mg II 279.6 nm line, the collisionally induced fluorescence at 280.27 nm can be observed for early delays after the femtosecond pulse. The ratio of the line intensities  $I_{280.27}/I_{279.6}$  decays much faster than it was observed for the fluorescence measurements on the nanosecond laser induced plasmas [81]. A thorough investigation of this difference was out of the scope of this thesis.

For nanosecond laser ablation, the scattered intensity is 100 times lower than for the femtosecond, and there is no need to use the polariser. According to the Mie scattering theory this might be an indication for the particle size distribution dominated by much smaller particles in the case of the femtosecond ablation than of the nanosecond one. It is interesting to compare the approximate total intensity of the Mie-scattered light from spherical copper particles ( $\lambda = 280$  nm, direction perpendicular to the direction of propagation) evaluated for two simple particle size distributions:

- $N_{small}$  particles much smaller than the light wavelength (radius  $\sim 1$  nm)
- $N_{big}$  particles with the 120 nm radius.

The total number of particles in each distribution is such that the ablated volume is equal:  $N_{small} \cdot V_{small} = N_{big} \cdot V_{big}$ . The evaluation shows that the distribution of small particles contributes about 100 times more to the scattered intensity than the distribution composed of the big particles [16, p. 633 et seq.].

Typical dependences of LIF signals on time at 50 mbar are shown in Figure 5-12. For each height, about 40 single measurements were performed to cover the time interval in which the atoms pass through the observation volume. An increase of the signal marks the moment in which the plume front, the contact surface between the internal and external shock wave ( $R_c$  in Section 2.4), reaches the observed height above the sample. The total measured intensity (a) is corrected by the scattered dye laser radiation (b) to yield the LIF- signal (c). The curves

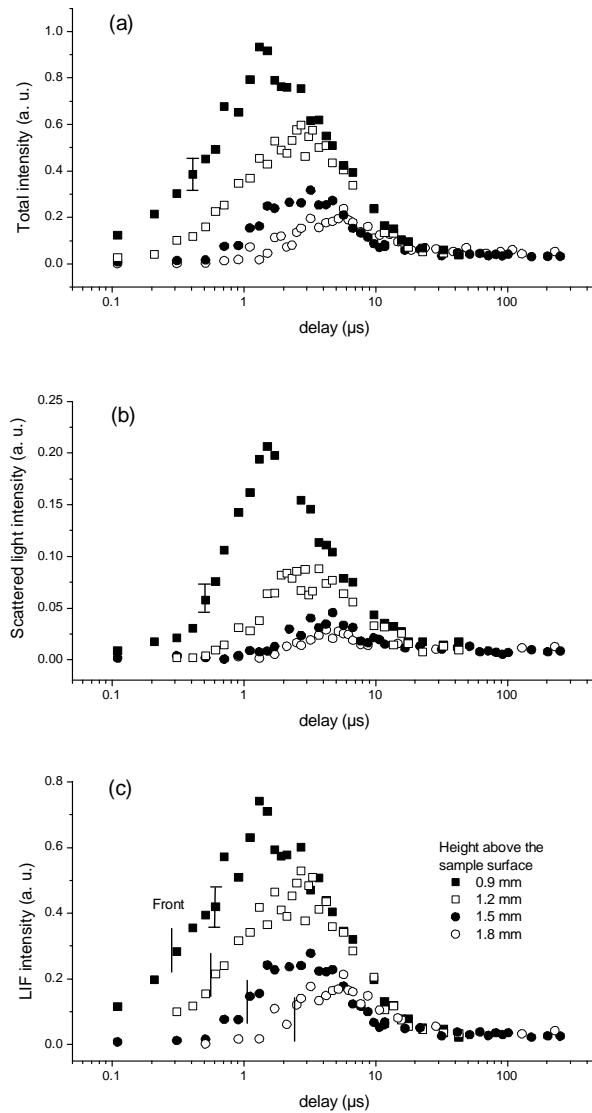


Figure 5-12: Typical intensity vs. time curves measured on the line Cu I 282.4 nm for four different heights in the plasma at 50 mbar argon pressure; energy of the fs-laser 215  $\mu\text{J}$ . (a) Total intensity; (b) scattered light intensity measured off-resonance (the dye laser energy same for (a) and (b)); (c) LIF intensity is the difference between the total and the scattered intensity. Lines mark the times at which the contact front reached the observed heights above the sample.

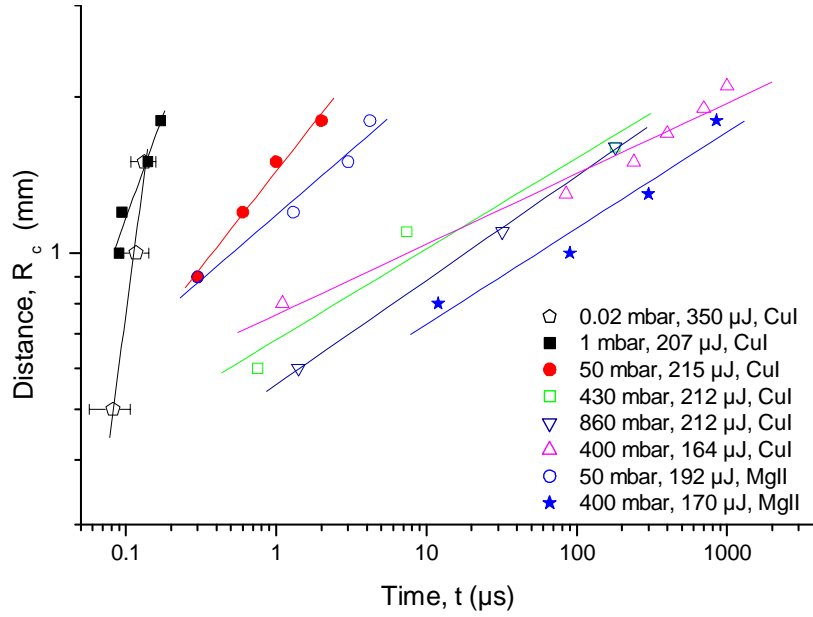


Figure 5-13: Position of the contact surface between the plume and the ambient gas  $R_c$  vs. time in a log-log plot. The fluorescence signals were measured at heights between 0.5 and 1.8 mm above the sample for different pressures and fs-laser energies. Cu I line 282.4 nm was used in all but two measurements, where the fluorescence at Mg II line 279.6 nm was induced. Where not shown, the error bars are smaller than the symbols.

have similar shapes, but the front of the scattering signal is slightly delayed with respect to the fluorescence, indicating that the atoms are leading the expansion, closely followed by the larger particles.

Coordinates of the plume front ( $R=h$ ,  $t$ ) were determined from such measurements by reading the time for which the raising fluorescence intensity is at  $1/e$  of its maximum value. The results are summarised in Figure 5-13. This logarithmic  $R_c(t)$  plot shows that the shock wave radius grows approximately as a power of time, different for each pressure. The exponent should be 1 for the free expansion in vacuum and should be falling with the pressure, indicating deceleration and, eventually, plume stopping. Much clearer is a dimensionless presentation of the same results in Figure 5-14 which enables a comparison with the spherical expansion model (Section 2.4). Quantities in the dimensionless coordinates are the ambient pressure ( $p$ ), the sound velocity in the given medium ( $c_g$ ), and the absorbed laser energy  $E=(1-R)E_{laser}$  as a measure of the total energy of the plume. The factor 2 corrects for the hemispherical

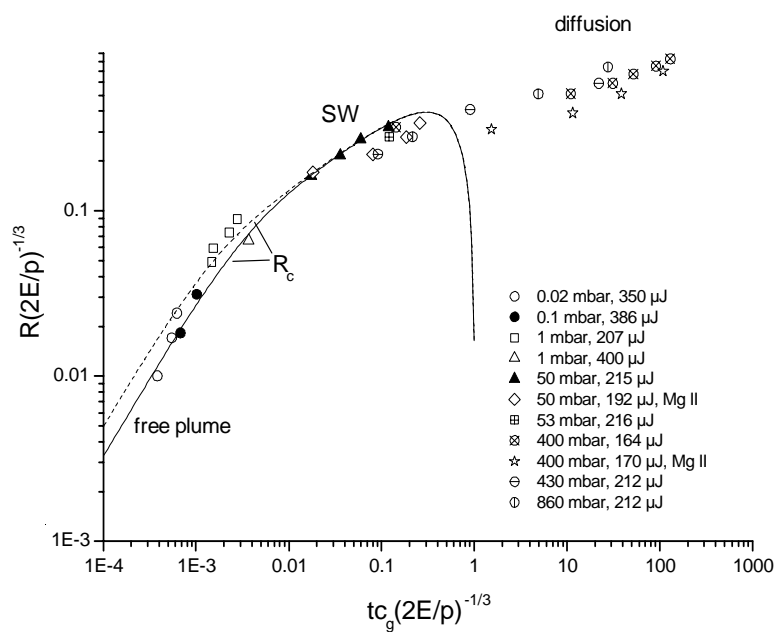


Figure 5-14: Dimensionless distance vs. time representation of the position of the plume front. The fluorescence signals were measured at heights between 0.5 and 1.8 mm above the sample for different pressures and fs-laser energies. Cu I line 282.4 nm was used in all but two measurements, where the fluorescence at Mg II line 279.6 nm was induced. The solid and the dashed lines are calculated according to the spherical expansion model for initial plume velocities of 10400 m/s and 16500 m/s respectively (section 2.4). SW: shock wave.

geometry since the model considers spherical expansion. Kieffer et al. [15] have measured that the reflectivity of Cu for 1 ps pulses ( $\lambda = 1 \mu m$ ) of the intensity of  $10^{14} \text{ W/cm}^2$  amounts to  $R \approx 0.5$ . This value was used in calculating the femtosecond laser energy absorbed by the sample. The dashed and the solid lines in the plot are numerically calculated (see 2.4) for initial plume velocities of 16500 m/s and 10400 m/s, respectively. In the shock wave region is the dependence on the initial plume velocity of minor importance. The measured results correspond well with the theoretical, up to the stopping point where the plume front velocity approaches zero. The model fails there because of the transition from an explosion driven expansion to diffusion. The velocity of the plume front in the diffusion regime is of the order of 1-10 m/s.

At higher pressures, such as at 855 mbar for which the time dependence of the Cu(I) fluorescence signal is shown in Figure 5-15, evidence of plume splitting can be found: at least two distinct maxima can be seen in the signal for each of the three heights. (For the lowest position,  $h=0.6 \text{ mm}$ , the times of the two maxima are 12 and 30  $\mu s$ .) Due to collisions of the ablated species with the atoms of the ambient gas, the internal shock wave starts propagating inwards, while the front part of the plume continues the expansion into the ambient. As the plume slows down, the internal shock wave is reflected from the substrate surface and through this process the plume temperature and mass density homogenise. Observations of plume splitting have been reported previously for nanosecond laser pulses at low pressures [82, 83].

These measurements are very instructive for further plasma studies. The consistency with the point blast model permits estimation of the dynamics and spatial and temporal extension of short pulse laser ablation plasmas for other samples and ambient conditions. It also helps to understand other spectroscopic measurements on transient plasmas. The fs- laser induced plasmas studied here are really small- the heights above the sample for which the measurements were made were between 0.5 and 1.8 mm. In the low pressure range they extend several millimetres further, but for conditions close to atmospheric (which are very interesting for many practical analytical applications) the plume expansion is stopped very close to the sample and the plasma equilibrates much faster with the surroundings. Correspondingly, the emission signal decays much faster ( $\approx 5 \mu s$ ), reducing the detection power of the optical emission spectroscopy compared to the lower pressure conditions. Nevertheless, the fluorescence signal remains high even 1 ms after the ablation onset (for certain heights above the sample), indicating that the

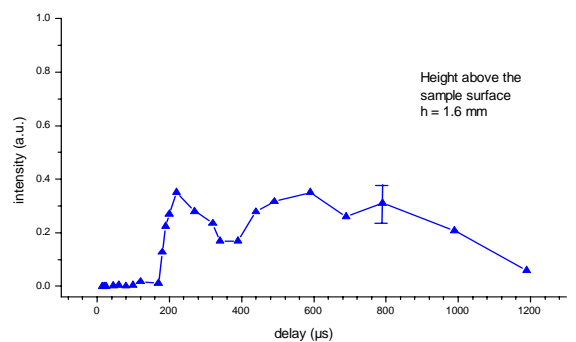
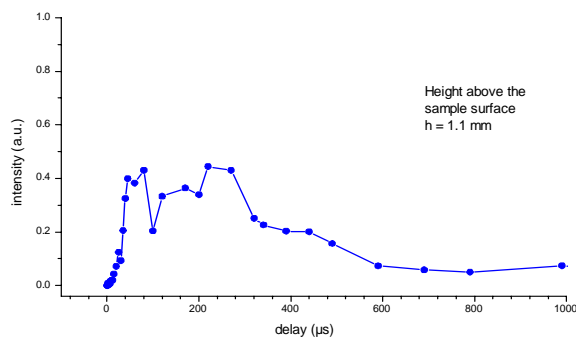
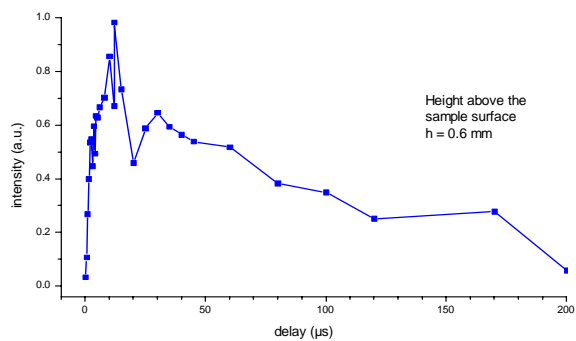


Figure 5-15: Fluorescence intensity versus time measured at Cu I line 282.4 nm at three heights in the plasma. Argon pressure: 855 mbar, fs-pulse energy: 212  $\mu\text{J}$ . Note the different scales of the abscissa axes.

atoms and ions in long living low states ( $\text{CuI } 3d^9 4s^2$ ) or ground states ( $\text{MgII}$ ) remain in the vicinity of the sample, only slowly diffusing away. In these circumstances an application of LIF as an analytical means might be useful.

### 5.2.2 Laser Induced Breakdown Spectroscopy

Prior to employing the femtosecond LIBS method for elemental analysis of solids, the properties of the laser induced plasma as a source of emission were studied on a technical copper and a brass sample. The samples were polished and the surface was always cleaned by several laser shots before the measurement. The description of the experimental arrangement is given in Section 4.2. In some experiments, the femtosecond laser system was operated also in the nanosecond modus (giving 6 ns pulses), for comparison.

#### Pressure dependence of emission signal (LIBS)

The emission signal can be taken from the side of the plasma or from the top (see Figure 4-3). Figure 5-16 shows the pressure dependence of the intensity of the copper atomic line ( $\lambda = 521.82 \text{ nm}$ ) integrated over the first 5  $\mu\text{s}$  and over the complete plasma volume from different views [55, 57]. The two views on the fs- plasma can be compared, as well as the influence of the pulse length (6 ns, 200 fs) in the side view configuration (all the other parameters were the same). The maximum line emission intensity of the fs- plasma is reached for argon gas pressures of 40-50 mbar. At lower ambient pressures and in vacuum, the plasma expands faster. The atomic and ionic densities of analytes are lower and so are the emission signal intensities. The decrease of the line emission intensity with increasing pressure in the range above 50 mbar is mainly due to faster cooling of the plume at higher pressures. The top-view configuration seems to be less sensitive to the pressure differences, but the absolute signal was lower than for the side-view (cannot be seen from the Figure 5-16). This was mainly due to the losses on the pierced mirror (see Section 4.2). Also, the dependence of the line emission intensity on the pressure at these first stages of the plasma evolution is much less pronounced in the ns- than in the fs- case. That is a consequence of the plasma shielding: the buffer gas plasma above the sample surface formed during the nanosecond pulse absorbs a part of the laser pulse energy. Such heating of the ns- plasma, that does not occur with ultrashort pulses (see Chapter 2),



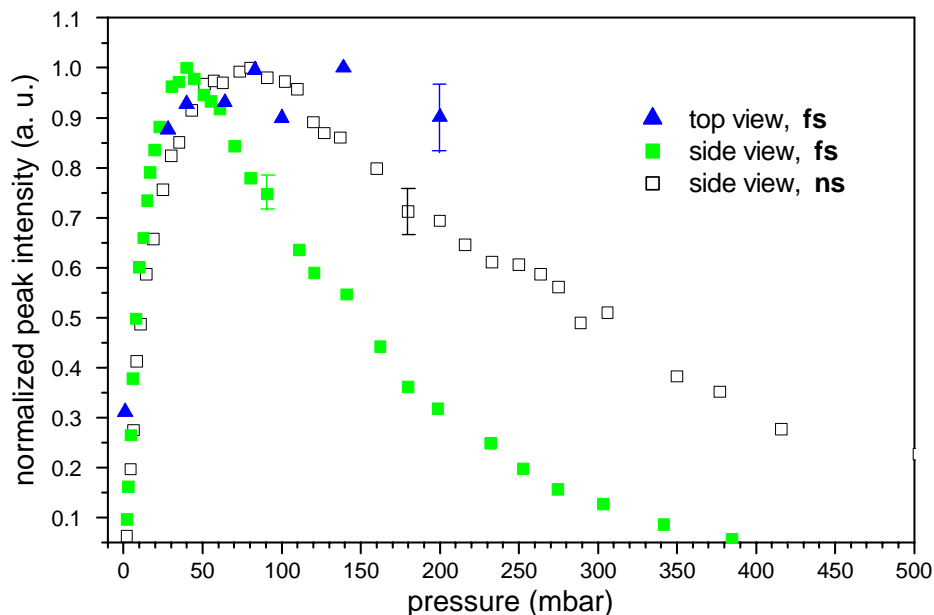


Figure 5-16: Pressure dependence of the normalized peak intensity of the Cu I 521.82 nm line from the fs- and ns- laser induced plasma viewed from the side and from the top.

makes the cooling by ambient gas slower than for fs pulses. The temperature and therefore the emission line intensity decay slower than for the femtosecond plasma.

Most of the following measurements were performed under the pressure conditions for which the line emission had its maximum and for which the best detection limits in the elemental analysis of solids can be obtained, at 40-150 mbar.

### Spatial distribution in emission

It is interesting to compare the spatial distribution of the excited atoms and ions in a fs- and a ns-induced plasma. Figure 5-17 shows the line emission of atomic and ionic lines of Cu and Mg as a function of the height above the sample. The line intensities in argon buffer gas at 140 mbar were measured with an integration time of 500 ns and a delay of only 200 ns after the laser pulse. A spatial resolution of 250  $\mu\text{m}$  was realised by moving a horizontal slit of the same width in front of the entrance slit of the spectrograph. (Plasma was imaged 1:1 on the entrance slit.) The spatial distribution of the emission line intensities reflects the density of ions/atoms and temperature distribution within the plume (compare eq. 3.1). An asymmetrical emission

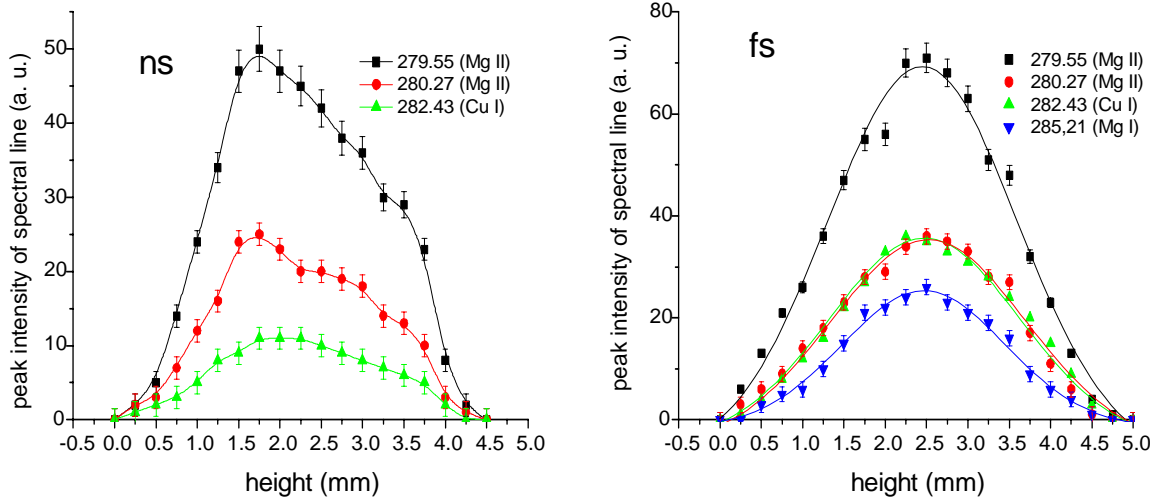


Figure 5-17: Spatially resolved ionic and atomic emission lines from ns- and fs- laser induced plasma integrated from 0.2 to 0.7  $\mu\text{s}$  after the pulse. Argon pressure 140 mbar; pulse energy 400  $\mu\text{J}$ ; technical copper sample.

distribution of the ns-plasma is in accordance with the laser-sustained detonation model [84, p. 146]: the strong compression of the front of the plume at an initial stage of the plasma evolution creates an efficient absorbing zone for the laser light, which results in a temperature rise at the rear of the plume front [75, 85]. In contrast, the fs-plume follows an expansion without additional heating.

The spatially resolved emission of Ar(II),  $\lambda = 434.81 \text{ nm}$  and Cu(I),  $\lambda = 437.81 \text{ nm}$  lines for fs- and ns-ablation is shown in Figure 5-18. Here, the argon pressure was 40 mbar, vertical resolution 100  $\mu\text{m}$ , delay 100 ns, and gate 100 ns. It is visible from the high argon ion line intensity that a considerable part of the ns-pulse energy (under certain conditions up to 100% [13]) is absorbed by the plume and used for the buffer-gas ionisation. The deposition of the femtosecond pulse energy into the sample is by far more efficient.

### Emission line dynamics

The temporal evolution of the line emission was studied imaging the whole plasma (or its central part) to the entrance slit of the spectrometer. The optimal time window for the analytical measurements had to be found.

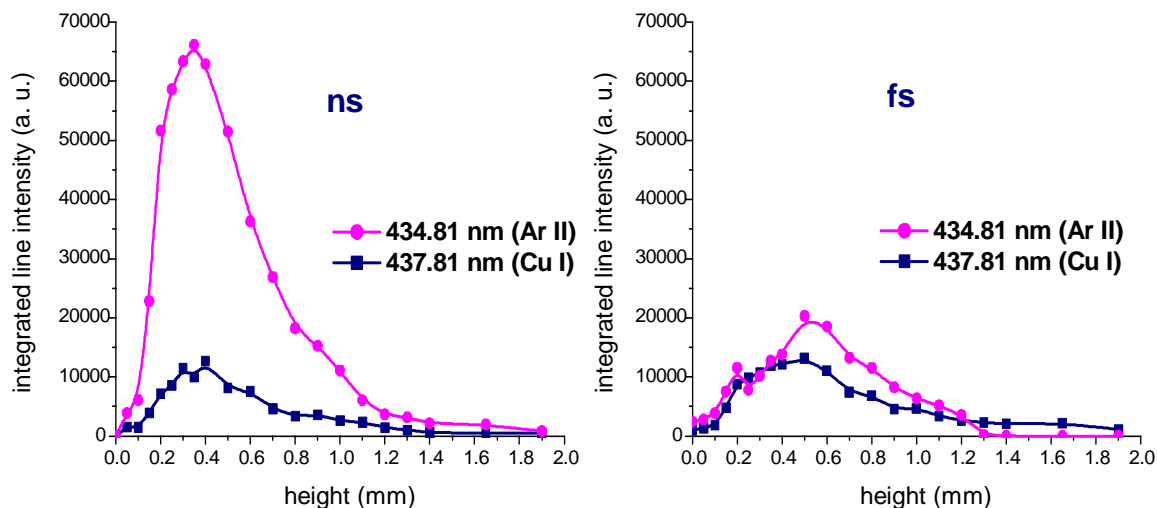


Figure 5-18: Spatially resolved argon ionic and copper atomic line emission intensity from the ns- and fs- plasma. Argon pressure 40 mbar; delay 100 ns; gate 100 ns; laser energy 400  $\mu$ J.

As the high intensity laser pulse hits the sample, prompt photoelectrons are created and are the first to leave the sample surface. Still in the early part of the first nanosecond after the pulse, they are followed by the main part of the very hot ablated material in the form of the atoms, ions and electrons, but also as bigger particles or droplets. The expansion described in the previous sections is accompanied by the recombination and relaxation processes within the plasma as it rapidly cools down. The very beginning of the plasma creation cannot be studied by the line emission measurements, not only because the gated detectors are still too slow to resolve the processes shorter than 1 ns. The more fundamental reason is the high background continuum radiation that dominates during the first 10-100 ns after the pulse, covering the atomic and ionic lines.

What happens during the first microsecond of the femtosecond laser induced copper plasma in an argon atmosphere (40 mbar) can be seen from the emission spectra in Figure 5-19. A side-view configuration of light collection from the central part of the plasma was used. The intensities of the ionic and atomic lines of Cu and Mg were measured with a time-gate of 100 ns for three different delays. The intensities of Mg and Cu *ion lines* (*Mg(II)*,  $\lambda = 279.55$  nm,  $\lambda = 280.27$  nm; *Cu(II)*,  $\lambda = 283.73$  nm) have their maxima near to zero delay and rapidly decrease with time. This could be expected, since the laser pulse is over before the plume of the

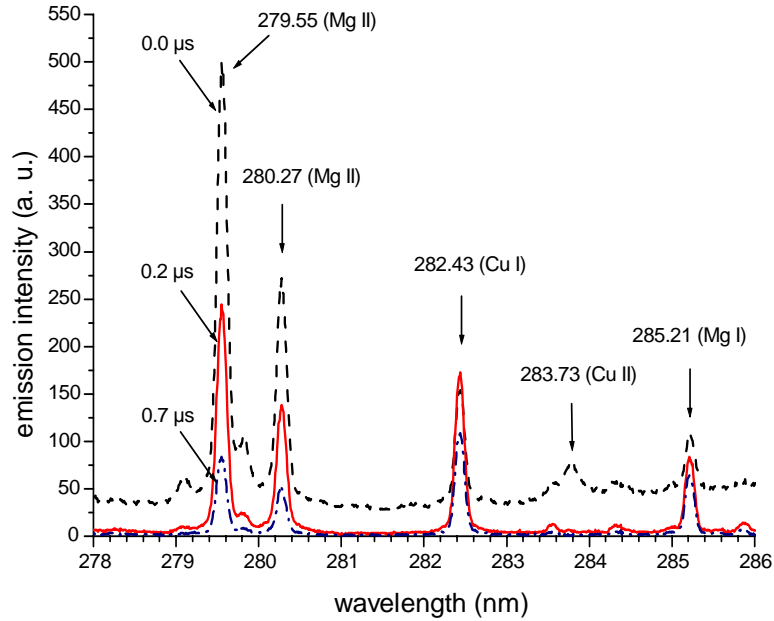


Figure 5-19: Fs- laser induced plasma spectra for three delays: close to 0, 0.2, and 0.7  $\mu\text{s}$  after the pulse. Gate 100 ns; argon pressure 40 mbar; sample technical copper; 400  $\mu\text{J}$  pulse energy.

ablated material is formed and there is no possibility for any further heating. The intensities of *neutral lines* (Cu(I),  $\lambda = 282.43\text{nm}$ ; Mg(I),  $\lambda = 285.21\text{nm}$ ) *slightly increase within the first 200 ns and slowly decrease later on*. This increase can be attributed to an increase in the number of excited neutrals due to the ion recombination. After that, the emission intensity monotonously decreases as the plasma expands and cools down.

Figure 5-20 (a) shows the time decay of the Cu and Zn atomic line intensities (on a logarithmic scale) during the femtosecond ablation of a brass sample (“TD02”) in an argon atmosphere (40 mbar) with the laser fluence of  $17\text{ J/cm}^2$ . Prior to each measurement, the sample was cleaned by 32 laser pulses, and the signal of next 32 pulses was accumulated. The lines in the plot are fits to the double exponential decay. Difference in the slopes for the two emission lines (between 5-20  $\mu\text{s}$ ) indicates strong cooling of the plume. The relative change of the excitation temperature between 5  $\mu\text{s}$  and 20  $\mu\text{s}$  after the pulse is about 20% (taken that  $T_{exc}=5000\text{ K}$  at 5  $\mu\text{s}$  delay- see the next section).

In Figure 5-20 (b) is the time dependence of the ratio of the two line intensities. 2-5  $\mu\text{s}$

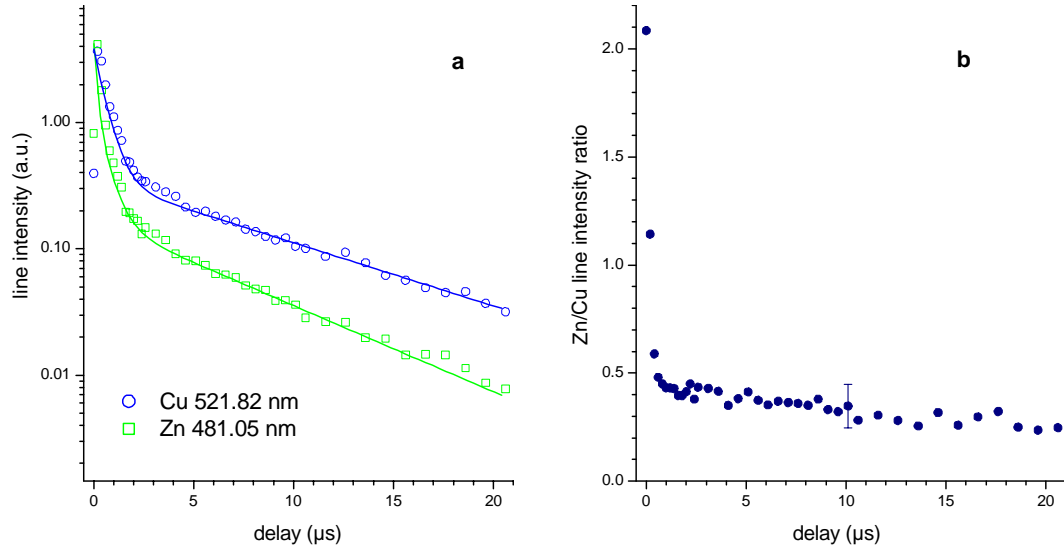


Figure 5-20: Time dependence of (a) the Cu and Zn atomic line intensities emitted from a femtosecond laser induced plasma and (b) the ratio of the two intensities. Sample: brass TD02; 40 mbar argon; 17 J/cm<sup>2</sup>; 32 shots accumulation.

after the laser pulse the ratio approaches a value that remains constant within the experimental error bars during the following 15-20  $\mu\text{s}$ . For higher ambient pressures the line intensities decay faster and the ratio reaches the constant value also during the first microseconds. Therefore, for the analytical measurements of plasma line emission, the light was accumulated from 2-20  $\mu\text{s}$  after the pulse.

### Excitation temperature

Plasma excitation temperature can be determined from the emission intensities of one element's lines that belong to transitions with a common lower energy level. Assuming the validity of the local thermodynamic equilibrium conditions, the line intensity is given by

$$I = c \frac{Ag}{\lambda} \exp\left(-\frac{E_{up}}{kT_{exc}}\right),$$

line set/ $E_{low}$ [ $\text{cm}^{-1}$ ]	<b>Zn1</b>	32890.352	<b>Cu</b>	13245.423	<b>Zn2</b>	32311.350
$\lambda$ [nm]/ $E_{up}$ [ $\text{cm}^{-1}$ ]	<b>307.2061</b>	65432.333	<b>327.9812</b>	43726.191	<b>328.2328</b>	62768.756
$\lambda$ [nm]/ $E_{up}$ [ $\text{cm}^{-1}$ ]	<b>334.5015</b>	62776.993	<b>353.0379</b>	41562.895	<b>468.0134</b>	53672.280
$\lambda$ [nm]/ $E_{up}$ [ $\text{cm}^{-1}$ ]	<b>334.5570</b>	62772.029	<b>570.0237</b>	30783.686		
$\lambda$ [nm]/ $E_{up}$ [ $\text{cm}^{-1}$ ]	<b>481.0528</b>	53672.280	<b>578.2127</b>	30535.302		

Table 5.1: Three sets of atomic lines used for determination of the plasma excitation temperature of brass samples.

where  $A$  is the transition probability,  $g$  the statistical weight and  $E_{up}$  the energy of the excited level,  $\lambda$  the line wavelength, and  $T_{exc}$  the excitation temperature. A plot given by

$$\ln \frac{I\lambda}{Ag} = -\frac{1}{kT_{exc}} E_{up} + \ln c$$

$$Y = BX + A$$

is called the Boltzman plot, its slope  $B$  being inversely proportional to the excitation temperature.

The temporal evolution of the fs- plasma excitation temperature was measured for six brass samples used for the analytical study (Section 6.1). Experimental conditions were as follows. The laser energy and focusing conditions ( $F=2.1 \text{ J/cm}^2$ ) were kept the same for all samples, placed in the argon atmosphere of 40 mbar. The central part of the plasma was imaged side-on to the optical fiber coupled to the echelle spectrometer. The light of 40 successive pulses was accumulated, after the surface had been cleaned by 80 laser shots. Boltzman plots were made for three sets of Zn and Cu atomic lines given in Table 5.1. Figure 5-21 shows the temperature for one of the samples. The big differences between the values obtained from the three different sets of lines at the early moments of plasma development indicate the absence of the local thermodynamic equilibrium. It is possible that the LTE is established after few hundred nanoseconds, which would coincide with the stabilisation of the line intensity ratio shown in Figure 5-20 (b). However, that can not be concluded from these measurements only.

Le Drogoff et al. [86] studied femtosecond plasma from ablation of Al alloys in air ( $F=20 \text{ J/cm}^2$ ). They reported electron densities (determined from Stark broadening) decreasing from over  $10^{18} \text{ cm}^{-3}$  to  $10^{17} \text{ cm}^{-3}$ , and the excitation temperature (from 8 Fe(I) lines) decreasing from 8000 K to 5000 K within the first microsecond after the pulse. The ionisation tempera-

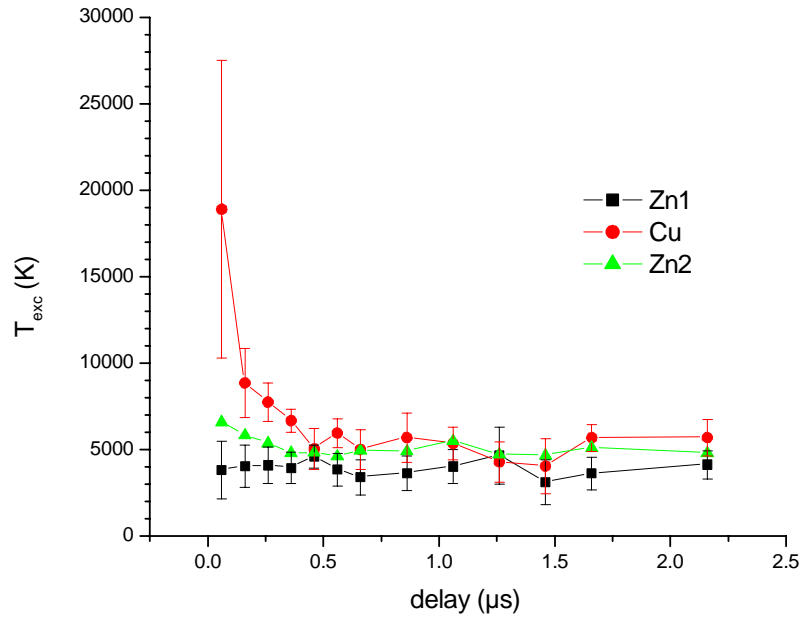


Figure 5-21: Time dependence of the brass plasma excitation temperature from the two sets of Zn lines and a set of Cu lines.

tures, determined from the Saha equation and magnesium lines, are systematically higher than the excitation temperatures, but their error bars overlap for delays longer than  $1 \mu\text{s}$ . These differences between the measured excitation and ionisation temperatures for delays longer than  $1 \mu\text{s}$  were explained by spatial averaging over the plume, rather than by the absence of the LTE [86].

Mean temperatures for all of the brass samples (in the same experimental conditions) are plotted in Figure 5-22. Within the accuracy of the measurement, no differences in the excitation temperature of the brass samples with different compositions could be observed at more than  $0.5 \mu\text{s}$  after the pulse. Figure 5-23 shows the averaged temperatures from  $0.56$  to  $2.16 \mu\text{s}$  for the six samples. The result that the excitation temperature of the femtosecond laser ablation plasma does not differ for the samples of different composition is important for the discussion of the non-linear calibration graphs of brass in Chapter 6.1.2.

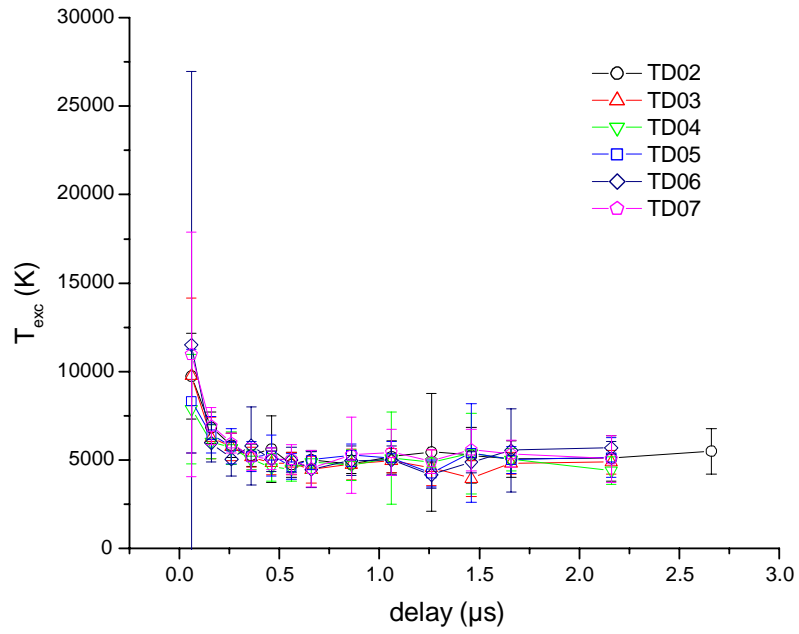


Figure 5-22: Excitation temperatures of the fs- laser induced plasmas from six brass samples (TD02-TD07). Each point is the mean of the three values from different line sets.

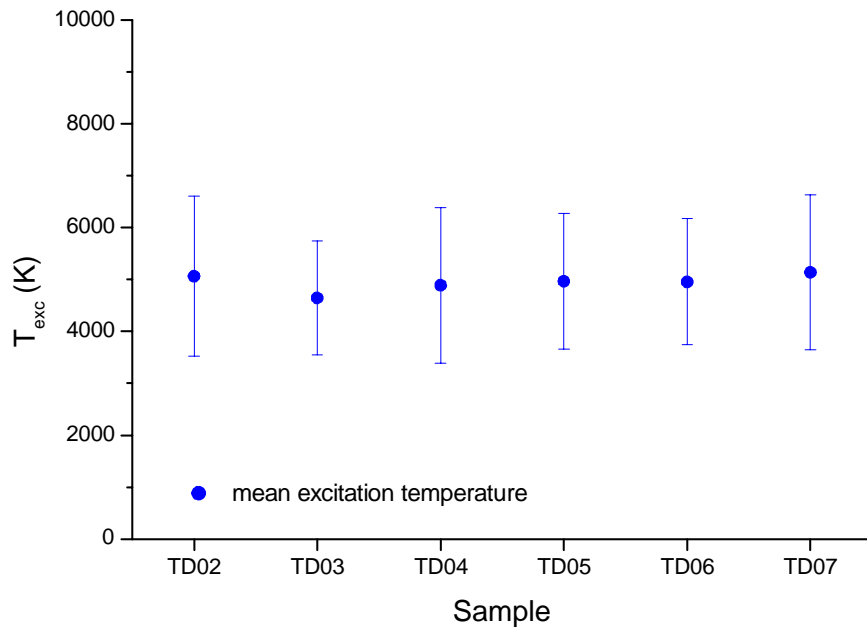


Figure 5-23: Averaged plasma excitation temperatures from 0.56 to 2.16  $\mu s$  after the fs- pulse for the six brass samples.



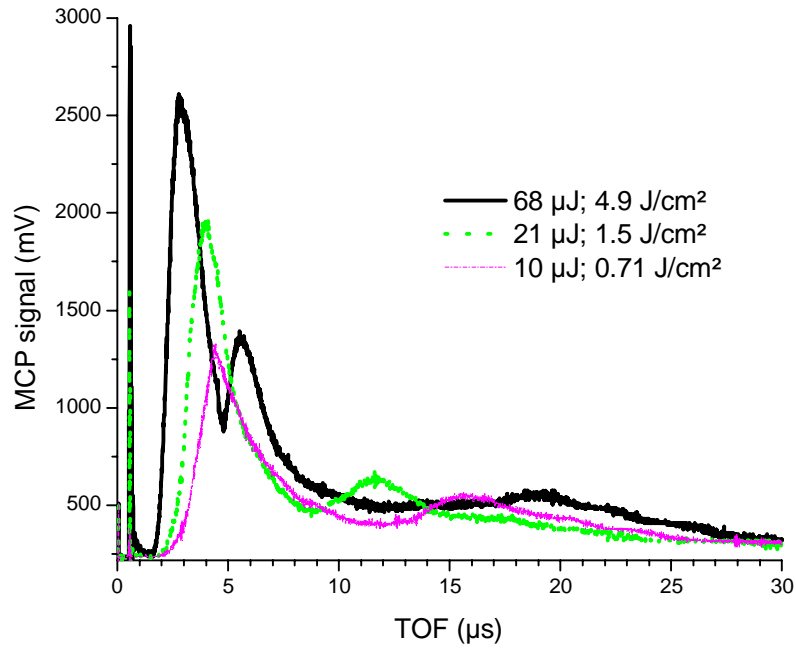


Figure 5-24: Direct time of flight of ions created in the laser ablation of aluminium sample for three different fluences of the fs laser.

### 5.3 Ion emission- direct TOF

Under high vacuum conditions in which the LA-TOF-MS measurements are performed, the plume expands freely, without resistance of the ambient gas. Measuring the time of flight of the particles over a given distance provides direct information on the initial velocity. The following experiment describes only the dynamics of ionic species induced by the laser- sample interaction. That information should be distinguished from the LIBS and LIF measurements that were performed in the presence of argon gas.

Aluminium and silicon samples were placed in the TOF chamber (pressure  $10^{-6}$  mbar) in the configuration presented in Figure 4-6. Only the voltage on the MCP detector was applied, and the time of free flight across the 0.585 m distance between the sample and the detector was measured. The surface was pre-cleaned by 40 laser shots and the signal was accumulated from 10 shots. The results for Al with several different laser energies are presented in Figure 5-24. The very first spike at  $0.5 \mu\text{s}$  are the photons, marking the actual beginning of the event. Characteristic for these signals are two pronounced peaks. The first ion peak for laser

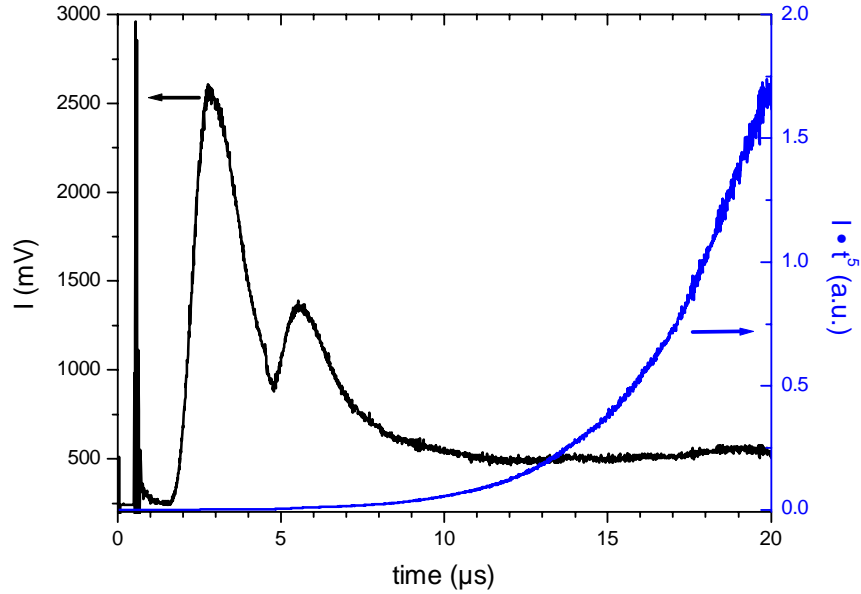


Figure 5-25: TOF signal and the function proportional to the ion velocity distribution.

fluence  $4.9 \text{ J/cm}^2$  corresponds to a velocity as high as  $250000 \text{ m/s}$ , or the  $\text{Al}^+$  kinetic energy of over  $9 \text{ keV}$ . The second component is also extremely fast-  $117000 \text{ m/s}$  ( $\approx 2 \text{ keV}$ ). For lower laser energies, the ions are slower.

In order to obtain the real velocity distributions from such measurements, the signals from Figure 5-24 should be multiplied by  $t^5$  (see Appendix C). That follows from the geometrical considerations: the flux through the detector plane of faster ions is larger than the flux of the slower ones with the same lateral velocity [87]. Figure 5-25 shows a TOF signal ( $4.9 \text{ J/cm}^2$ ) and a function  $I(t) \cdot t^5$ , proportional to the associated velocity distribution. The total number of ions in these fast peaks is small in comparison to the number of later, slower ions. The long distance between the sample and the detector favours the detection of faster ions.

These fast ions cannot be of the thermal origin since their kinetic energies correspond to the temperatures of more than  $10^6 \text{ K}$ . The possibility that the fast component comes from the electrons could be excluded: applying a positive potential on the drift tube extinguished the signal, while the negative voltage accelerated the particles and narrowed the signal, as demonstrated in Figure 5-26.

Figure 5-27 shows the peak velocities in dependence on laser fluence. Data for three

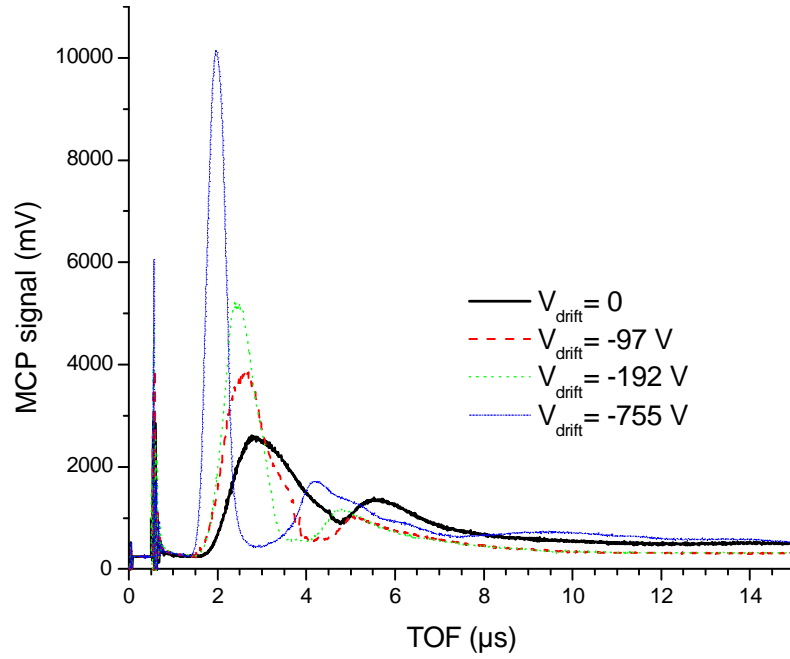


Figure 5-26: Direct TOF signals created during the fs laser ablation of Al in vacuum ( $F = 4.9$   $\text{J}/\text{cm}^2$ ) with additional acceleration at the entrance to the drift tube.

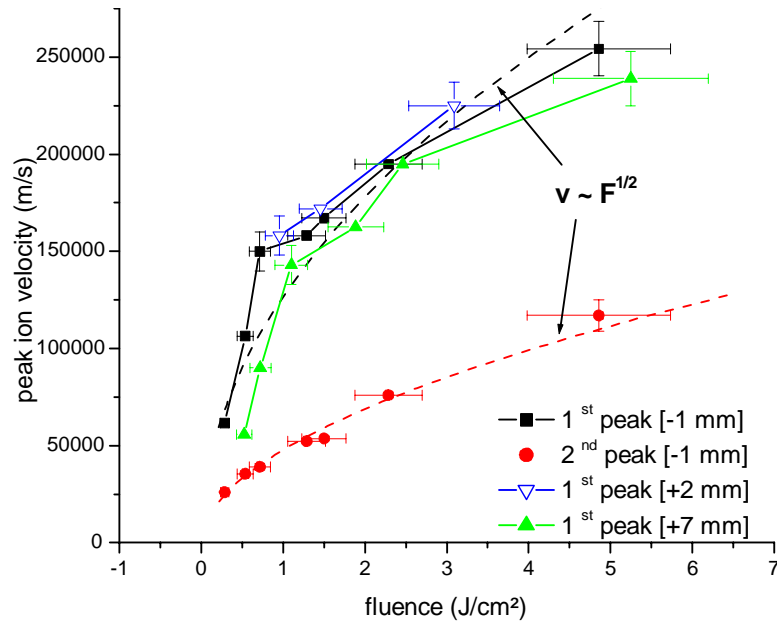


Figure 5-27: Al ion velocities corresponding to the first and the second peak in Figure 5-24 vs. laser fluence.

different focus positions are presented: 1 mm below the surface and 2 and 7 mm above the sample surface. They overlap, taking into account the fluence error bars. The broken lines are the best fits from the log-log plots resulting with the slopes  $\approx 0.5$ . The ion kinetic energies are proportional to the laser fluence. Ions with similar velocity distributions were observed also for silicon (not shown). The fastest ions that have resulted from the nanosecond laser excitation in the same experimental arrangement had the energies of the order of 100 eV.

Which mechanism during the femtosecond ablation of metals produces ions with several keV energy is not clear. Highly energetic ions were observed in fs ablation of sapphire, but not in the measurements on metallic Al done in the same laboratory [20, 59]. For dielectric materials, such phenomenon is explained by an impulsive Coulomb explosion from a highly charged surface. During the first ps after the pulse, after the prompt electrons have left the surface, there is a strong electrostatic repulsion among the *surface* ions due to which they can leave the sample with high energies. In metals and semiconductors, the charge neutralisation in the electron depletion zone is much faster, making the probability of a Coulomb explosion process lower than for dielectrics [20].

Recently, a nonthermal ion emission during the femtosecond laser ablation of metals (Al, Au, Cu) has been reported by Amoruso et al. [88]. The fluence range was (0.3-1.5 J/cm<sup>2</sup>), and the distance from the sample to the TOF- detector 70 mm. The signal forms resemble those reported here and the ion energies are of the same order of magnitude. Moreover, it can be seen from their measurements that the fast ion emission is more pronounced for p-polarised light (used here) than for the s-polarised. The explanation suggested in [88] is the negative space-charge-induced acceleration of ions. This process is termed ambipolar diffusion (AD) in the field of plasma physics [89].

If a plasma contains highly energetic particles and the pressure inside is higher than that of the ambient, its constituents tend to diffuse out. This diffusion is ambipolar if the number densities of positively and negatively charged particles is similar. The smaller and lighter electrons have longer mean free path and higher velocities than the ions, so that they can leave the plasma sooner which makes it electron-depleted. The effective space-charge separation induces an electric field which then limits the number of electrons that can leave the plasma. The depletion is possible in the plasma sheath, the thickness of which equals the Debye length,

and only the ions from the sheath can be accelerated. The electric field can be approximated by that of a capacitor. The maximal kinetic energy that an ion can acquire is given by

$$\Delta E_{kin} = Ze^2 N_{el} \lambda_D / \epsilon_0 S.$$

$e$  is the charge of an electron and  $Ze$  the charge of the accelerated ion,  $N_{el}$  is the number of the escaped electrons,  $\epsilon_0$  the permittivity of vacuum,  $S$  the area of the ‘‘capacitor’’, and  $\lambda_D$  the Debye length:

$$\lambda_D = \sqrt{\frac{\epsilon_0 kT}{2n_{e,i} e^2}}.$$

$n_{e,i}$  are the number densities of the charged particles and  $T$  is the plasma temperature.

At the early moments after the laser pulse the gitter temperature is of the order of  $10^4$  K (see Section 2.3.4) and the electron density  $10^{18}$ - $10^{19}$   $cm^{-3}$  [86], giving a Debye length  $\approx 10$  nm. The laser spot area is typically  $S \approx 10^{-5}$   $cm^2$ . Amoruso et al. estimated the number of the escaped electrons to be  $\sim 10^{11}$  [90], which is sufficient to accelerate the single charged Al ions to the energies higher than 1 keV.

An attempt to assign the two peaks to the ions of different charges/masses has been made: the set of measurements with additional acceleration by an electrical field (shown in Figure 5-26,  $F=4.9$  J/cm<sup>2</sup>) shows that the ratio of the charge number and the relative atomic mass  $Z_1/A_1 = 0.44 \pm 0.05$  for the first peak, and  $Z_2/A_2 = 0.07 \pm 0.02$  for the second peak. Assuming that  $A_1 = A(Al) = 26.98$ , the first peak is formed by highly charged ions with  $Z_1 = 12 \pm 1$ . (Note that  $Z=13$  is the limiting ionisation state of aluminium.) The second peak can be assigned to  $Al^{2+}$  ions. Any clusters that would fit to the results for  $Z/A$  would have to carry more charges, which is only less probable. The analysis can be continued by noting that the ratio of the two ratio values reported above  $\frac{Z_1 A_2}{Z_2 A_1} = 6 \pm 2$ . From the fits in Figure 5-27 that shows the peak velocities dependence on laser fluence, it can be deduced that the ratio of squared velocities of the ions of the first and the second peak  $\frac{v_1^2}{v_2^2} = 6.9 \pm 0.6$  (for all fluences applied). Assuming that the masses of ions in both peaks are equal  $A_1 = A_2$ , the ratio of kinetic energies  $\frac{E_{k1}}{E_{k2}} = \frac{v_1^2}{v_2^2} \simeq \frac{Z_1}{Z_2}$ . This indicates that the same mechanism (involving charge acceleration in an electric field) might be responsible for creation of both peaks, contrary to the interpretation by Amoruso et al. that the second peak is of thermal origin [90]. Further investigation is necessary to illuminate this

phenomenon. It might seem contradictory that the highest signal comes from such a high ionisation state. The reason for that is the fact that the flux of ions is being measured so that the fastest ions result with the highest signal intensity (see Figure 5-25 and Appendix C). Contributions from all the other ionisation states are probably contained in the signal as well. The creation of  $Al^{2+}$  might be a lot more probable than of the higher states so that it appears in the TOF signal as a separate peak. The majority of the ions produced is in  $Al^+$  state, but they are slower. Therefore, the signal associated to them in this experimental arrangement is much lower than for the multiple-charged ions.

Whichever mechanism creates such velocity distributions, these have consequences for the optimisation of TOF-MS instrument when the repeller is used and mass resolution is obtained. The repeller field is too weak to redirect the fastest ions into the drift tube. Which velocity class of ions can reach the detector depends on their mass and charge. In the mean mass/charge range of 25-65, ions with initial velocities from the interval  $\langle 1500\frac{m}{s}, 15000\frac{m}{s} \rangle$  could be detected (not all at the same time). A question arises for complex samples: in which relation are the initial velocities of ions of different species? Such a study, especially for the fastest ions, would require substantial modifications of the TOF instrument and is out of the scope of this stage of the research. These observations are also of interest for the analytical applications. If the interaction of the femtosecond laser pulse with a solid could be optimized to result in a fast ions production, even better control of the layer by layer material removal (analogous to the ion sputtering) could be established, enabling high resolution in-depth profiling (see Chapter 7).

## Chapter 6

# Laser ablation sampling for bulk elemental analysis of solids

In this chapter, the first element analysis applications of femtosecond laser ablation of solid samples are presented. It was already anticipated in Chapter 3 that one of the most interesting questions related to the fs laser ablation is whether fractionation effects can be reduced in comparison to the ns lasers or perhaps completely avoided. This investigation was performed with three sets of known samples: brass, aluminium, and glass. The two widespread analytical techniques, LIBS and LA-ICP-MS, were used.

### 6.1 Analysis of brass

Brass seems to be a system with the most pronounced fractionation effects in nanosecond ablation [47, 51, 91, 92]. The calibration graphs (signal to concentration) are strongly non-linear, and even the internal standardisation method does not always lead to correct analytical results. Since the dominating processes during the nanosecond laser material removal are melting and boiling, later accompanied by resolidification, these difficulties were explained by significant differences in vapour pressures of the main components. The evaporation temperatures of Zn and Cu are 907 °C and 2567 °C, respectively. In 1970 Baldwin has studied Q-switched laser sampling of Cu/Zn alloys and showed that the vapour and resolidified material contain increased amounts of Zn [91]. Cromwell and Arrowsmith [47] demonstrated changes in relative LA-ICP-

Sample	$c_{\text{Cu}}$ ( $m_{\text{Cu}}/m_{\text{Brass}}$ )	$c_{\text{Zn}}$ ( $m_{\text{Zn}}/m_{\text{Brass}}$ )	$x_{\text{Cu}}$ ( $n_{\text{Cu}}/n_{\text{Brass}}$ )	$x_{\text{Zn}}$ ( $n_{\text{Zn}}/n_{\text{Brass}}$ )
TD02	80.25	19.71	80.74	19.26
TD03	70.20	29.76	70.83	29.17
TD04	65.50	34.46	66.18	33.82
TD05	63.12	36.84	63.82	36.18
TD06	60.55	39.41	61.27	38.73
TD07	58.05	41.91	58.78	41.22

Table 6.1: Composition of brass samples used in the study.  $c$  are the concentrations with respect to the mass and  $x$  with respect to the amount of substance  $n$ .

MS signal intensities for different laser fluences, and different numbers of successive pulses on the same sampling area. More recently, non-linear calibration graphs and fractionation effects have been reported by Gagean and Mermet for LA-ICP-AES (atomic emission spectroscopy) [92], and by Borisov et al. for LA-ICP-MS [51]. Lasers of different pulse durations and wavelengths were used, and the non-linear calibration curves were in common to them all. The samples from different suppliers showed big deviations from the calibration curve, suggesting the influence of metallurgical pretreatment. Fractionation effects were reduced for UV lasers and for high laser intensities ( $>1 \text{ GW/cm}^2$ ). For example, Ko et al. obtained good LIBS calibration graphs with internal standardisation with IR ns laser intensity of  $60 \text{ GW/cm}^2$  [34].

The question is whether the femtosecond laser ablation can be a solution for these difficulties that occur also for many other matrices. To examine this, a series of LIBS experiments was performed on a set of known brass samples. Both femtosecond and nanosecond pulses were used for ablation, under otherwise similar conditions [55].

The samples used for this study, delivered by the Wieland Werke (AG Metallwerke, Ulm), were of pure technical grade. The sample compositions are listed in Table 6.1. They were polished with  $1\text{-}\mu\text{m}$  grade diamond paste to guarantee a smooth, flat surface.

### 6.1.1 Comparison of femtosecond and nanosecond LIBS

Convenient lines for this study were Cu(I)  $521,820 \text{ nm}$  ( $4d \ ^2D_{5/2} - 4p \ ^2P_{3/2}^0$ ) and Zn(I)  $481.053 \text{ nm}$  ( $5s \ ^3S - 4p \ ^3P_2^0$ ). Both lines have comparable transition probabilities and the energy difference between their upper levels is relatively small ( $\sim 3700 \text{ cm}^{-1}$ ), making them suitable for internal standardisation. Their intensities were high in comparison to some other lines that decayed too fast, and there were no problems with self-absorption. The light was collected from



the side and the pressure of the buffer gas argon was chosen to be 40 mbar and 900 mbar. The 40 mbar value was chosen because of the maximum emission intensities in the fs case. With ns-pulses, the difference between the maximum signal at 80 mbar and the signal at 40 mbar was less than 10 % (compare Figure 5-16). A pressure of 900 mbar was selected since it is close to the atmospheric pressure used in LA-ICP-OES/MS. Care has been taken to ensure that the laser energy and focusing conditions were the same for all of the samples, since any differences would influence the relative line intensities and change the  $I_{Zn}/I_{Cu}$  ratio. The highest intensities were obtained when the laser beam was focused slightly below the sample surface. That means that the number of atoms populating the upper levels for the measured lines was maximal in the volume and time observed.

The best integration time for line intensity measurements could be deduced from the temporal behaviour of Cu and Zn line intensities and intensity ratios for ns- and fs-modes of ablation. These temporal profiles were measured with a gate time of 100 ns by changing stepwise the delay between the laser pulse and a detector gate-pulse. After about 2-5  $\mu$ s, the intensity ratio of the lines  $I_{Zn}/I_{Cu}$  is constant within the experimental error bars. 15-20  $\mu$ s after the laser pulse the line intensities of both elements are too low and the extended integration of the emission does not provide any improvement in the sensitivity. Therefore, the line intensities were integrated between 2 and 20  $\mu$ s.

*An enhancement in the emission signal of one component due to fractional evaporation of the sample during the ablation process should be accompanied by a depletion of that component in the laser affected zone.* To check for preferential evaporation, the ratio  $I_{Zn}/I_{Cu}$  was measured for successive laser shots on the same spot of the sample. Figures 6-1 and 6-2 show representative results for two different pressures and two different energies, for fs and ns pulses respectively. After a definite number of pre-shots (which are indicated as the argument values on the abscissa in Figures 6-1 and 6-2) the line intensities of the subsequent 10 shots were accumulated and processed. The selected lines of Cu and Zn were sequentially measured in two different spectral windows of the Czerny-Turner grating spectrograph. The procedure was repeated twice for each element. Error bars were calculated from the data sets of the two measurements. Higher laser energies had to be used in the high pressure range to improve the signal-to-noise ratio. Differences in measured ratios for different experimental conditions (laser energy, pressure) can

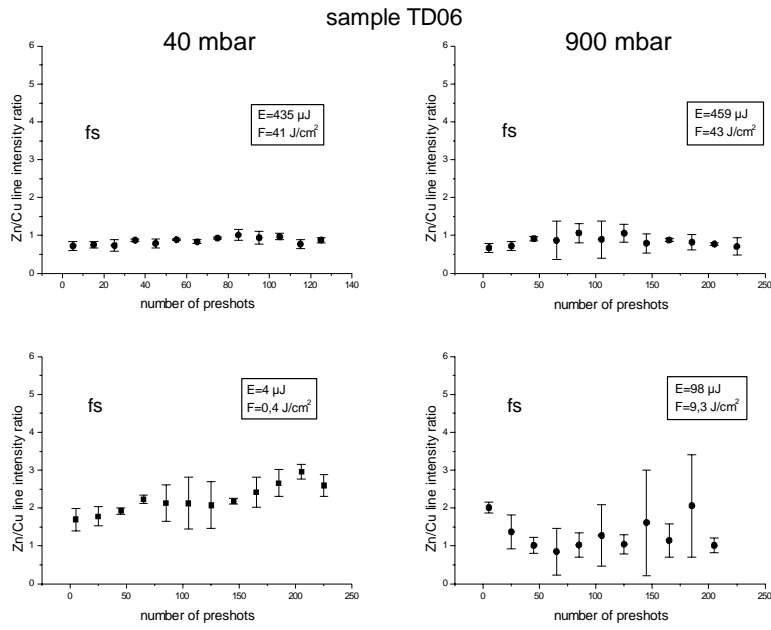


Figure 6-1: Intensity ratio of Zn and Cu atomic lines (see text) vs. the number of preshots for two fs- laser pulse energies at 40 mbar and two at 900 mbar argon pressure.

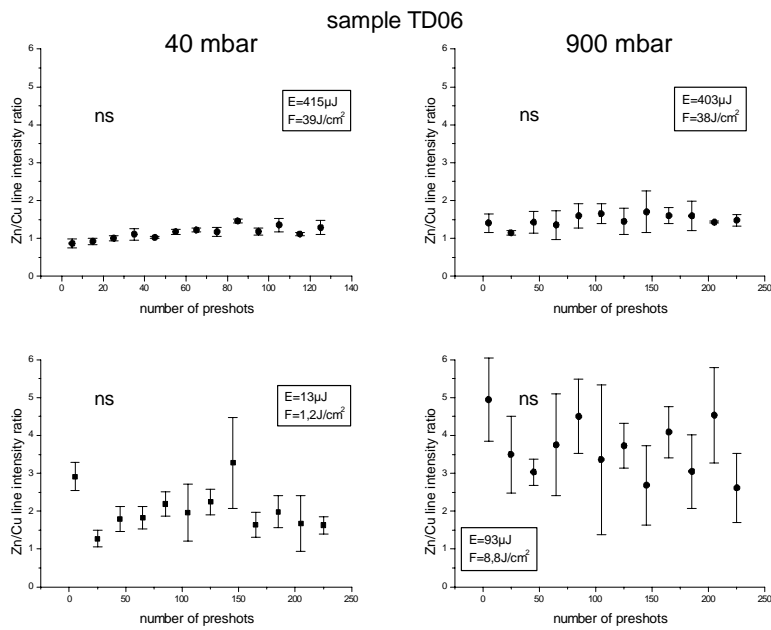


Figure 6-2: Intensity ratio of Zn and Cu atomic lines (see text) vs. the number of preshots for two ns- laser pulse energies at 40 mbar and two at 900 mbar argon pressure.

be explained by different excitation temperatures.

*Fractionation should appear as a variation of the  $I_{Zn}/I_{Cu}$  ratio in depending on the number of shots. Within the experimental error bars, no change of the intensity ratio on the number of shots was detected neither for fs- nor for ns-laser pulses.* This result corresponds well with the published data [34, 51, 92] for ns-lasers with intensities larger than 1 GW/cm<sup>2</sup>. For the fs-pulse energy of 4  $\mu$ J (0.4 J/cm<sup>2</sup>), which was the lower limit for detection of line intensities in the setup used, there is some indication of the effect (see Figure 6-1). However, within the given precision a final statement can not be given.

Despite the fact that at higher pressure the line intensity decreases faster in the fs-case than in the ns-case (see Figure 5-16), the precision of the intensity ratio is still higher with fs- than with ns-pulses. Such a trend has been already observed in the comparison of ns- and ps-ablation [93].

*The calibration graphs for Zn and Cu were measured under the same pressure conditions and with similar laser energies. As before, the light was collected from 2-20  $\mu$ s after the pulse. After 40 cleaning pulses, the signal was accumulated for 10 pulses. This procedure was repeated five times for each Cu and Zn line. Each line was integrated, and the average value and the standard deviation were calculated from the five measurements. Cu was used as the *internal standard* (Section 3.2.2). The resulting calibration graphs for Zn/Cu ratios are shown in Figures 6-3 and 6-4 for fs and ns pulses, respectively.*

Linear calibration curves were obtained in all cases. For measurements is favourable to use higher laser energies since then more material is sampled, and low pressures which enable longer measuring times and higher signal intensity. The linear regression shows that the correlations for ns- ablation at higher pressure or at lower energies are poor. In general, the calibration curves for different pulse energies and pressures in the fs-case have better correlation coefficients. A numerical evaluation of the precisions of the fs and ns LIBS analysis can be done taking one of the samples as an unknown. For the sample TD03 (Zn/Cu ratio 0.424) the obtained values are  $(0.41 \pm 0.03)$  and  $(0.42 \pm 0.07)$  in fs and ns case, respectively. The confidence intervals were calculated for a confidence level of 0.95, and it is two times larger for the ns than for the fs sampling.

This shows that, even at optimal pressure and energy conditions, *the precision of femtosec-*

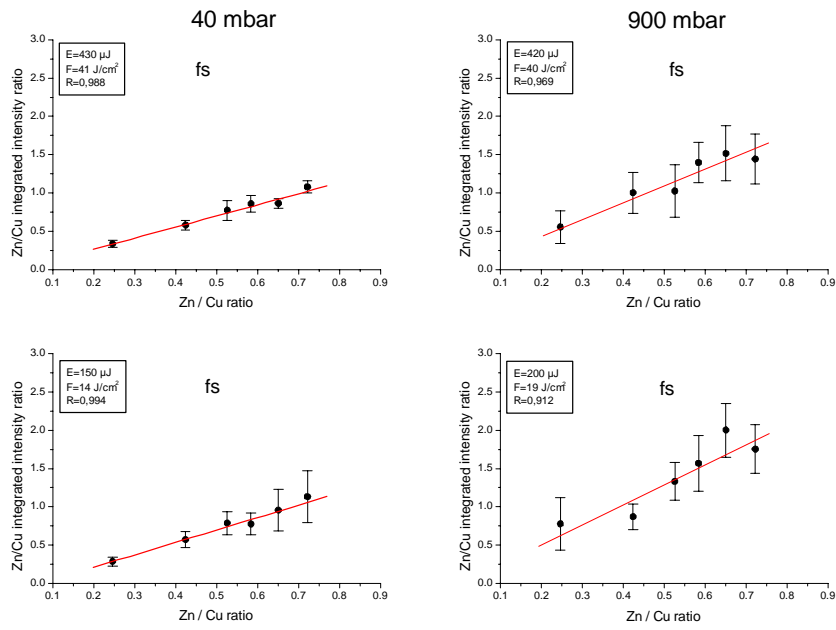


Figure 6-3: Calibration for the Zn/Cu ratio at different pressures and laser energies for fs laser pulses.

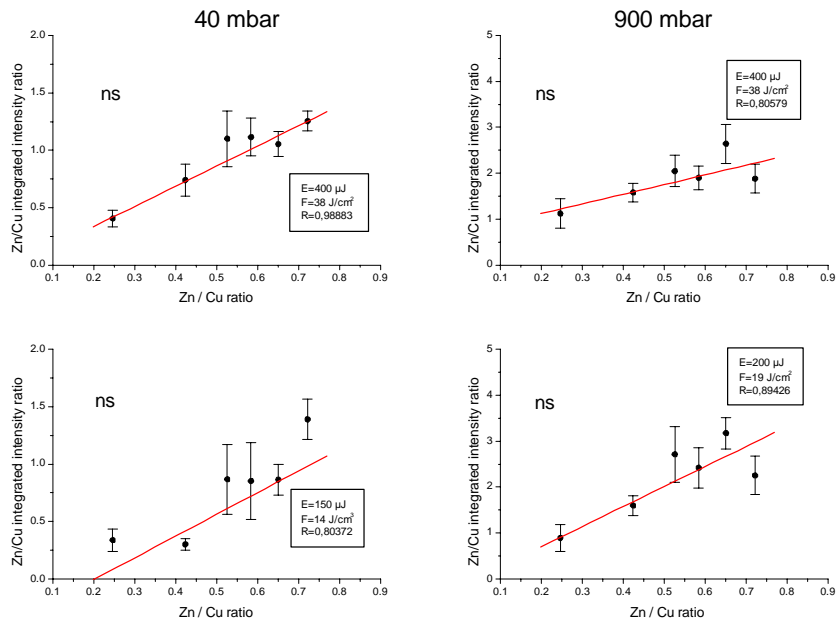


Figure 6-4: Calibration for the Zn/Cu ratio at different pressures and laser energies for ns laser pulses.

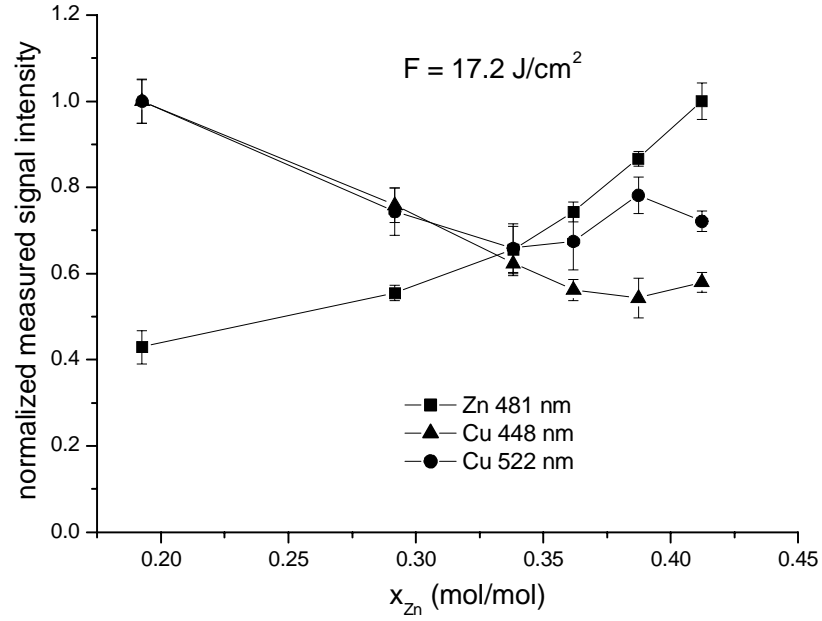


Figure 6-5: Calibration curves for Cu and Zn lines at low argon pressure (40 mbar) plotted as normalized line intensities vs. zinc concentration. Fs laser fluence  $17.2 \text{ J/cm}^2$ .

and LIBS is better than of the nanosecond.

### 6.1.2 Modelling of non-linear calibration graphs

Without the internal standardisation, the calibration graphs are non-linear. Figure 6-5 shows the measured intensities of two Cu and one Zn lines obtained with fs-pulses at low pressure. They were measured at 40 mbar with the fluence of  $17.2 \text{ J/cm}^2$  ( $100 \text{ TW/cm}^2$ ).

Similar observations were reported for ICP-MS and ICP-OES studies with ns and ps laser sampling in [51] and [92], showing that the brass calibration curves are non-linear for any laser pulse duration and wavelength. Such behaviour was explained by the structural differences between the samples which influence the melting temperature [92] and the reflectivity [51] of the sample surface so that the mass ablation rate is a function of the Zn/Cu ratio. Another possible explanation to account for the non-linearity of the calibration graphs is that *the plasma conditions* are influenced by differences in the ablated mass and therefore by changes in the bulk stoichiometry. This could be ruled out by the findings of Fernandez et al. [94]: a strong

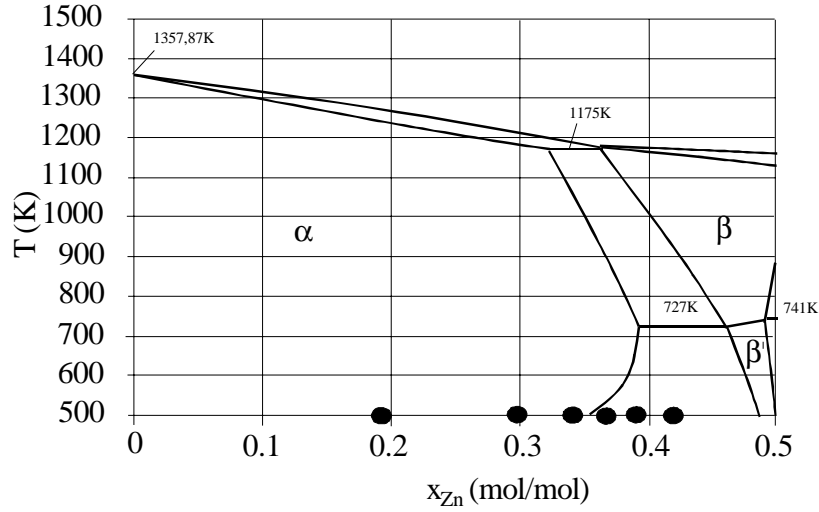


Figure 6-6: Cu-Zn phase diagram for the range 0-50% Zn. The dots indicate the composition of the brass samples that are used in this study.

correlation of the spectral emission intensity of spectral lines from an inductively coupled plasma coupled to a laser ablation cell and the directly measured emission intensity of the LIBS plasma of brass has been established [94]. Because the excitation conditions in both plasmas are very different, a good correlation between the measured line emissions indicates that differences in line intensities in LIBS or ICP measurements of brass must be solely due to the laser radiation-solid interaction. They cannot be explained by different excitation temperatures of the LIBS and ICP plasmas due to changes in the ablated mass.

The amount of the femtosecond pulse energy deposited in the sample is known since the laser interacts only with the sample and not with the plume. This permits the evaluation of the relative ablated mass from basic material constants based on the model presented in Section 2.2. It will be shown that the differences in the ablated mass observed in the studies of non-linear calibration curves can be related to changes in the phase and composition of the material [56].

Figure 6-6 shows the part of the phase diagram of the Cu-Zn system that is pertinent to these investigations together with the samples used in this study. The data have been taken

from Landolt - Börnstein [95]. Three samples have the  $\alpha$ -phase crystal structure (fcc), and three are of the mixed  $\alpha\beta$  structure ( $\beta$ -bcc). To find the desired connection the ablated mass has to be calculated as a function of the composition or a related parameter.

Assuming that, according to [94], there are no significant changes in the plasma conditions, the measured LIBS line intensities are proportional to the ablated mass:

$$I_{Zn} \sim x_{Zn} \frac{\rho_{brass}}{M_{brass}} L_{\alpha}^{\delta,l} \quad (6.1)$$

$$I_{Cu} \sim (1 - x_{Zn}) \frac{\rho_{brass}}{M_{brass}} L_{\alpha}^{\delta,l} \quad (6.2)$$

$M_{brass}$  and  $\rho_{brass}$  are the molar mass and the density of the sample,  $x_{Zn}$  is the atomic percentage of zinc, and  $L_{\alpha}^{\delta,l}$  is the ablation depth per pulse defined by one of the equations 2.3 and 2.4, depending on the applied laser fluence:

$$L_{\alpha}^{\delta} \cong \delta \ln\left(\frac{(1-R)F}{F_{th}^{\delta}}\right) [m], \quad F_{th}^{\delta} = \rho\Omega\delta \left[ \frac{J}{m^2} \right] \quad (6.3)$$

$$L_{\alpha}^l \cong l \ln\left(\frac{(1-R)F}{F_{th}^l}\right) [m], \quad F_{th}^l = \rho\Omega l \left[ \frac{J}{m^2} \right] \quad (6.4)$$

( $\rho$  is the density  $\left[ \frac{kg}{m^3} \right]$ ,  $\Omega$  the enthalpy of evaporation  $\left[ \frac{J}{kg} \right]$ ,  $R$  reflectivity,  $F$  the laser fluence,  $\delta$  the optical penetration depth, and  $l$  the electron heat penetration depth). It has been shown in Section 5.2.2 that *the excitation temperature* of the femtosecond laser ablation plasma of brass does not depend on the sample composition, so that the temperature dependent term in the emission line intensity (compare eq. 3.1) has no influence on the non-linearity of calibration curves.

All values necessary to calculate the right sides of expressions 6.1 and 6.2, except the penetration depths and the reflectivity, are tabulated in literature or can be interpolated from known data with sufficient precision. *The optical penetration depth and the optical reflectivity as a function of the composition can be calculated from the classical Drude model for metals* (Section 2.1.1). The idea behind the approach is the interdependence of optical constants and electrical conductivity as it arises directly from Maxwell's equations.

In the Drude model the square of the complex refractive index  $\mathbf{n}^2 = n^2 - k^2 + i2nk$  can be

expressed as [14]:

$$\begin{aligned} n^2 - k^2 &= 1 - \frac{N_e e^2}{m_e \varepsilon_0} \left( \omega^2 + \frac{1}{\tau^2} \right)^{-1}, \\ 2nk &= \frac{N_e e^2}{m_e \varepsilon_0} \frac{1}{\omega \tau} \left( \omega^2 + \frac{1}{\tau^2} \right)^{-1} \end{aligned} \quad (6.5)$$

where  $N_e$  is the effective free electron density,  $e$  and  $m_e$  are the charge and the mass of an electron, respectively,  $\varepsilon_0$  dielectric permittivity of vacuum,  $\omega$  the frequency of the incident electromagnetic wave, and  $\tau$  the electron relaxation time (or transport time [9]). The effective free electron density  $N_e$  in brass alloys can be approximated on the basis of an average number of conduction electrons (valence electrons) per atom by [96]

$$\begin{aligned} N_e &= N_{average} N_A \frac{\rho_{brass}}{M_{brass}} \\ N_{average} &= 2x_{Zn} + x_{Cu} = 1 + x_{Zn} \\ N_A &= \text{Avogadro's number.} \end{aligned}$$

For normal incidence, the reflection coefficient is

$$R = \frac{(n-1)^2 + k^2}{(n+1)^2 + k^2}.$$

The optical penetration depth (or the skin depth) is given by

$$\delta = \frac{c}{2nk\omega}, \quad (6.6)$$

and  $\tau$  is connected to the steady current resistivity  $\rho_0$  [14]

$$\tau = \frac{m_e}{N_e e^2 \rho_0}. \quad (6.7)$$

The resistivity  $\rho_0$  of brass is tabulated as a function of composition [97]. Note that for the visible region ( $\omega \gg 1/\tau$ ) and for good conductors the optical absorption depth is in good approximation inversely proportional to the steady current resistivity  $\rho_0$  (compare equations



6.5 and 6.6):

$$\delta \approx \left( \frac{m_e \omega}{N_e e^2} \right)^2 \frac{\varepsilon_0}{\rho_0} = \text{const.} \frac{1}{\rho_0}.$$

Below, the optical absorption depth  $\delta$  is calculated from eq. 6.6 without any approximation. The electron heat penetration depth that governs the ablation rate in the high fluence regime can be approximated by eq. 2.2:

$$l = \sqrt{D\tau_a}.$$

The electron diffusion constant  $D$  can be estimated by [9]

$$D = \frac{1}{3} v_F^2 \tau. \quad (6.8)$$

$v_F$  is the Fermi velocity of the electrons which can be taken to be constant and  $\tau$  is again the electron relaxation time as it is used in eq. 6.5.  $\tau_a$  is the time which is necessary for the electrons to transfer their energy to the lattice. It can be estimated by

$$\tau_a \approx \tau \frac{M_{ion}}{m_e}$$

where  $M_{ion}$  and  $m_e$  are the ion and electron masses. Inserting  $\tau_a$  into 2.2 and using relations 6.8 and 6.7 results in

$$l \approx \text{const.} \frac{1}{\rho_0}. \quad (6.9)$$

This is reasonable since the electric resistivity is a sensitive measure both for the free electron subsystem of a metal and for the interactions of this subsystem with the lattice due to collisions [9]. Not all the necessary data are available to calculate the constant factor in formula 6.9, but the ratio  $\delta/l$  can be calculated on the basis of energy dependent ICP-MS measurements as it is shown in Figure 6-7. The low- and the high- energy region are distinguished by different slopes of the signals which can be used to determine the ratio between the constants (see equations 6.3 and 6.4).

With this simple model it is now possible to calculate the ablated mass and normalise the measured intensity to the calculated values. The values used for these calculations are listed in Table 6.2. The tabulated data [97-99] were interpolated to the sample compositions that are

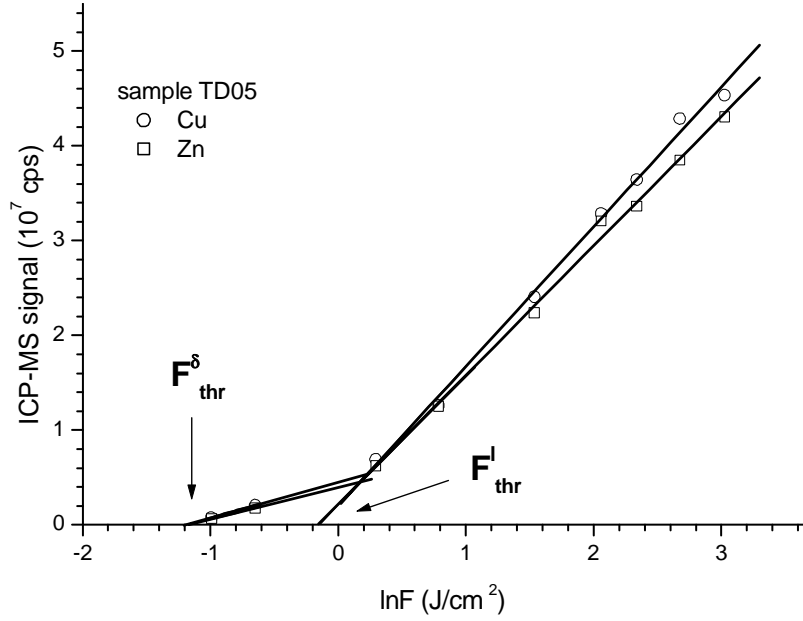


Figure 6-7: The ICP-MS signals as functions of the laser fluence on a logarithmic scale. From the slopes and the threshold values for the high and low fluence ablation regimes the ratio of the electron heat penetration depth and the optical penetration depth can be determined.

$x_{Zn}$	$N_e [m^{-3}]$	$\rho [gcm^{-3}]$	$M [gmol^{-1}]$	$H_b [kJmol^{-1}]$	$\rho_0 [10^{-8}\Omega m]$
19.26	9.6093E28	8.550	63.90	-5.67660	5.3379
29.17	1.0275E29	8.465	64.08	-7.82288	6.2573
33.82	1.0579E29	8.424	64.17	-8.63010	6.5147
36.18	1.0734E29	8.405	64.21	-8.99095	6.6030
38.73	1.0888E29	8.375	64.26	-9.34390	6.4196
41.22	1.1031E29	8.342	64.31	-7.90466	5.6440

Table 6.2: Effective free electron densities, densities, molar masses, evaporation enthalpies and steady current resistivities of the brass samples used in the study of non-linear calibration curves

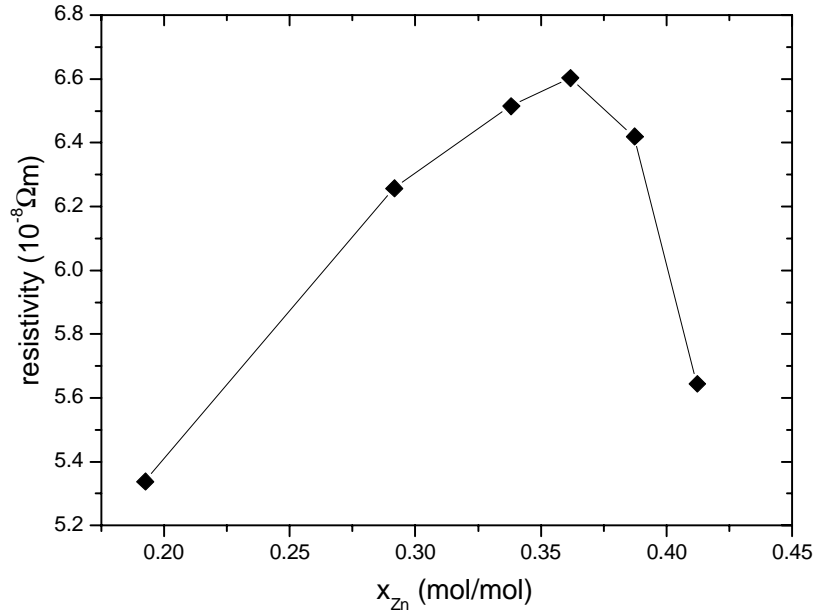


Figure 6-8: The electrical resistivity as a function of the Zn content. The values are interpolated from tabulated values [97].

used in this work. Figure 6-8 displays the calculated resistivity as a function of composition.

The complex refractive index for the six brass samples, shown in Figure 6-9, was calculated from the values given in Table 6.2 and relations of the Drude model. The calculation of the optical constants is in principle only valid for perfect surfaces, but here only their relative changes due to differences in the elemental concentration ratio are of interest. It is assumed that the increasing roughness with the number of laser shots has no significant influence on the relative value of the optical constants. The ablation depths were calculated for the low and the high fluence regime taking into account the optical absorption depth. The results are shown in Figure 6-10. For two different incident laser fluences the normalised simulated Zn and Cu - “signals” (eqs. 6.1 and 6.2) are compared in Figure 6-11. This figure displays the functional dependence of the calibration graphs as they have been found in the different measurements. The measured emission intensities from Figure 6-5 are now normalised to the calculated masses, as shown in Figure 6-12. Fairly good regression coefficients ( $>0.97$ ) indicate that this simple model describes the background of the observed effect well.

It should be emphasised that *the resistivity of an alloy is not only a sensitive measure of the*

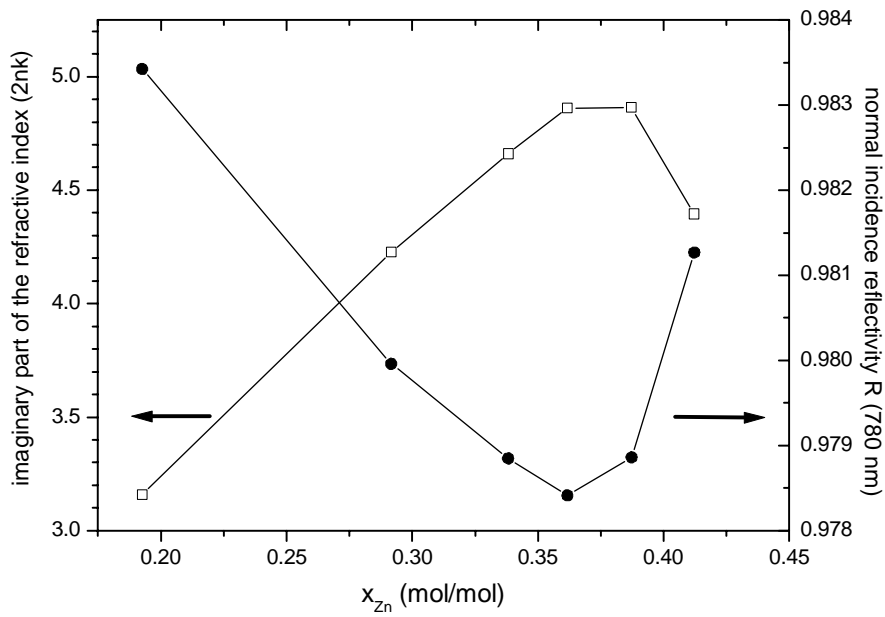


Figure 6-9: Optical constants calculated from the Drude model and tabulated values for resistivity as functions of the Zn content.

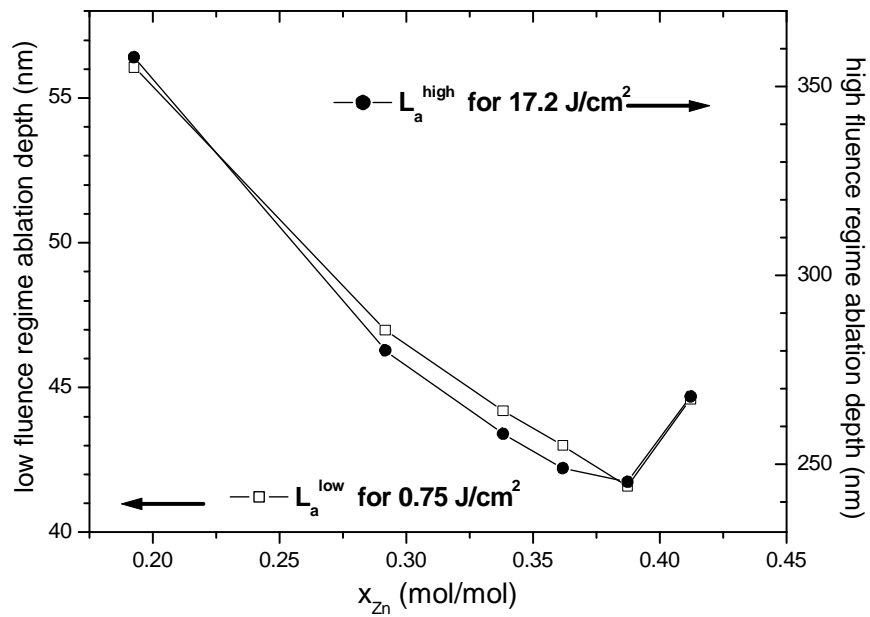


Figure 6-10: Calculated ablation depth as a function of the Zn content for the high and the low fluence regime (see equations 2.3 and 2.4).

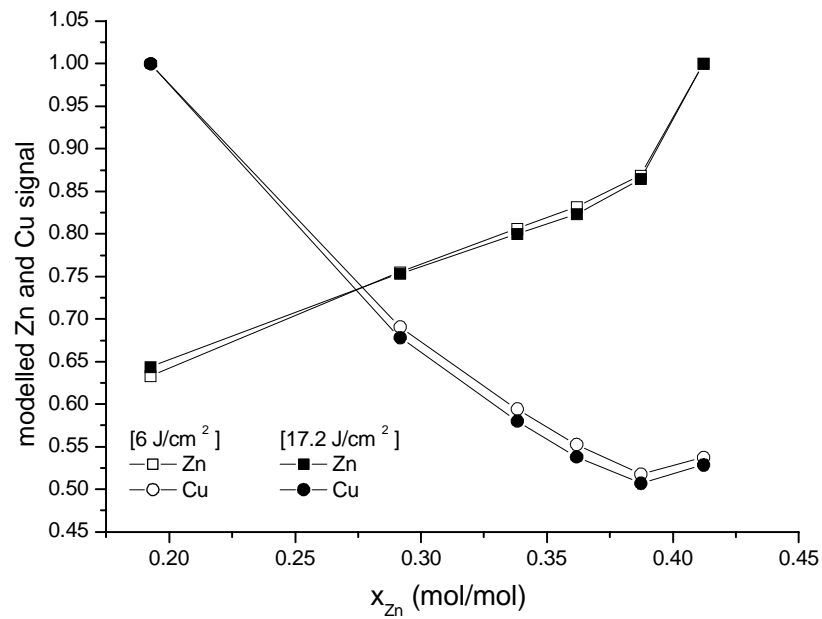


Figure 6-11: Simulated and normalized Zn and Cu calibration curves for the high and low fluence regime (see equations 6.1 and 6.2).

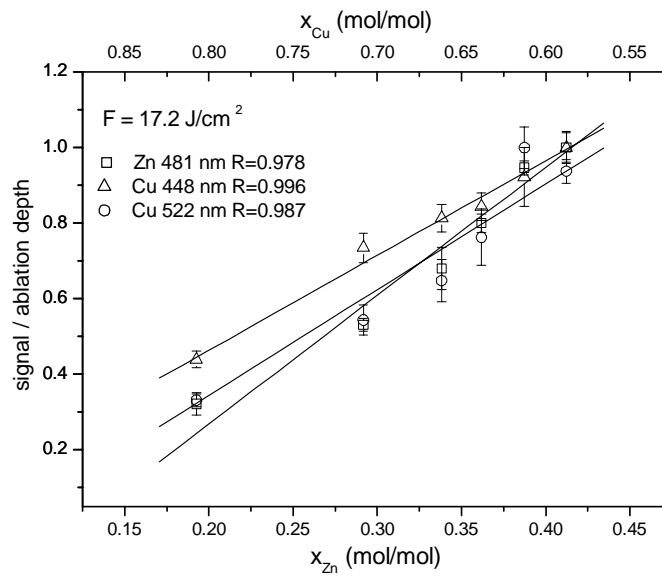


Figure 6-12: The measured Cu and Zn signals normalized to the calculated ablation depth at a laser fluence of  $17.2 \text{ J/cm}^2$ . The regression coefficients demonstrate a good agreement with the linear fit.

*stoichiometric composition, it is also sensitive to structural changes such as a change in the  $\alpha/\beta$ -phase distribution caused by different thermal treatments.* This might explain the observations described in the paper by Gaegan and Mermet [92] that the measured data for the samples from different suppliers strongly deviated from the calibration graphs. Also, it is a possible source of error in the present calculations, because it is known that the sample treatment is consistent within the brass series, but not which distribution of  $\alpha/\beta$  crystallographic phases resulted.

To summarise, it has been shown that concentration dependent changes in the electronic subsystem of brass alloys govern the differences in the ablated mass. The only relevant, basic parameter to describe this behaviour is the steady current resistivity. On this basis, it is possible to calculate the ablated mass as a function of composition and establish the connection with the non-linearity of calibration graphs.

## 6.2 Femtosecond LA-ICP-MS

The previous section dealt with one aspect of the laser ablation sampling for bulk elemental analysis- matrix effects in binary alloys. It has been shown that with femtosecond pulses the fractionation effects are reduced compared to the lasers with longer pulses. The non-linearity of calibration graphs is connected to the different ablation rates of different matrices. These results were confirmed with the fs-LA-ICP-MS measurements of the same samples. Whereas in LIBS the information on elemental composition comes from the atoms and ions in the plasma, in ICP-MS the ablated particles are subjected to analysis. The absence of preferential vapourisation observed in LIBS should be characteristic for the particulate matter as well, providing the fractionation effects are not produced during the transport of the particles to and within the ICP.

Calibration graphs for the series of brass samples (with internal standardisation), obtained with different laser energies are shown in Figure 6-13. Fluences in the range of 0.4 to 20 J/cm<sup>2</sup> result in linear calibration graphs (correlation coefficients of 0.99) that almost overlap. Isotopes <sup>65</sup>Cu and <sup>66</sup>Zn were measured.

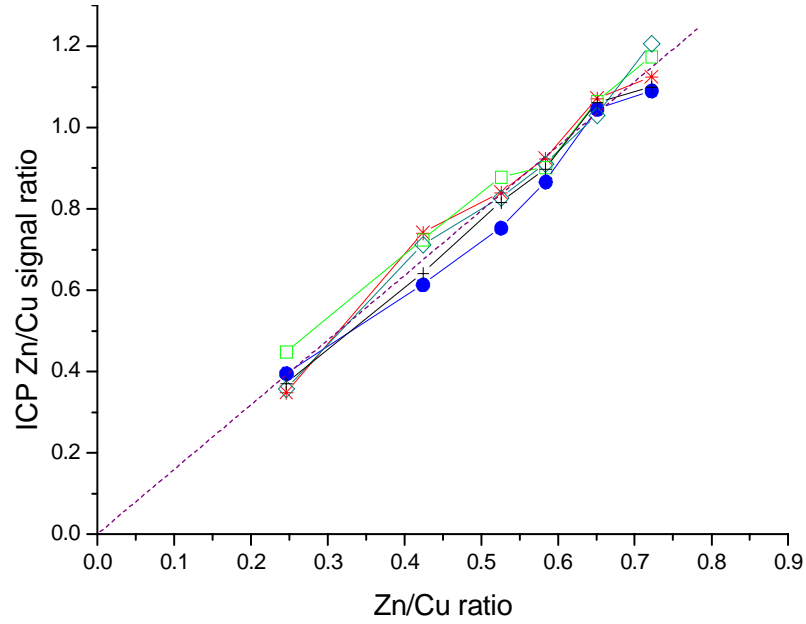


Figure 6-13: Calibrations for the Zn/Cu ratio from the LA-ICP-MS measurements of the six brass samples with different laser fluences (in the range of 0.4 to 20 J/cm<sup>2</sup>).

### 6.2.1 Analysis of Al samples

Besides the measurements of the main components as in the case of binary alloys, a common task in analysis of solid samples is the determination of trace elements concentrations, for which fractionation can also occur. The performance of the femtosecond laser in that field was tested on a set of aluminium company standards (Alusuisse, Schweizerische Aluminium AG, Neuhausen am Rheinflal). Their composition is given in Table 6.3. Figure 6-14 shows typical signals for six trace elements. Before each measurement, the sample surface was pre-

sample	Mn	Mg	Cr	Zn	Pb	Sn	V	Ti
S124	0.049	0.051	0.05	0.061	0.022	0.02	0.054	0.058
S132	0.0035	0.16	0.0025	0.018	-	0.003	0.008	0.0025
S134	0.0013	0.001	0.0002	0.001	0.0011	0.0003	0.001	0.0002
114/02	0.0027	0.0015	0.0005	0.0013	0.0015	0.0010	0.0012	0.0005
115/01	0.0025	0.0038	0.0028	0.0025	0.0005	0.0010	0.0025	0.0015
116/01	0.005	0.008	0.0045	0.0055	0.0012	0.0020	0.0041	0.0037

Table 6.3: Trace element concentrations in the aluminium samples applied (percent).

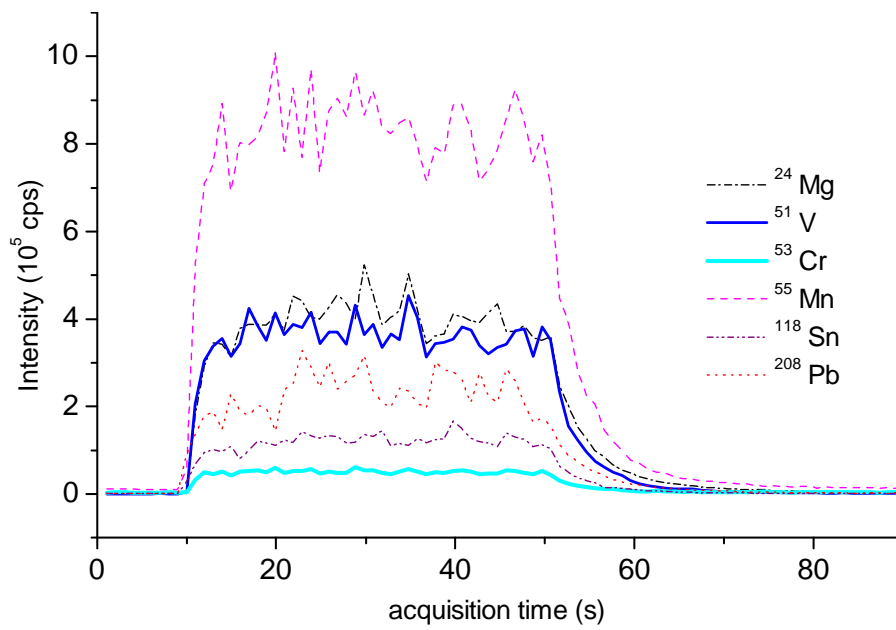


Figure 6-14: LA-ICP-MS signal intensity in counts per second vs. the acquisition time for one isotope of each trace element in the aluminium sample "115/01". Laser fluence: 17.2 J/cm<sup>2</sup>, repetition rate: 9.7 Hz.



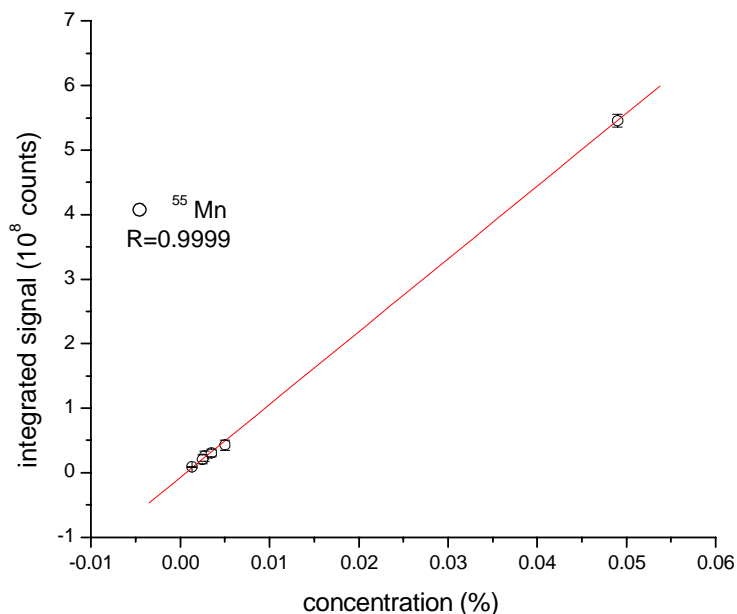


Figure 6-15: Integrated LA-ICP-MS signal of Mn vs. its concentration in the analyzed aluminium samples.

cleaned with 80 laser shots. For optimal focusing conditions (focus slightly below the sample surface), 40 seconds of continuous ablation on the same spot (390 laser shots) were possible before the signal intensity decreased, due to lower ablation rates at high aspect ratio craters. In order to calculate trace element concentrations, the signals were integrated (leaving the rising and the decaying part out) and corrected for natural abundances of the measured isotopes. The calibration curve for manganese is shown in Figure 6-15. It is linear across two orders of magnitude in the trace element concentration, which means that these samples are similar in structure and the ablation rates do not differ. For analysis of samples with higher portion of trace elements and for calculation of the concentrations, the internal standardisation method should be employed. Calibration graphs for these samples with the  $^{24}\text{Mg}$  as an internal standard are presented in Figure 6-16. The dashed lines mark  $\pm 10\%$  deviation from the slope 1. The limits of detection are in the ppb range.

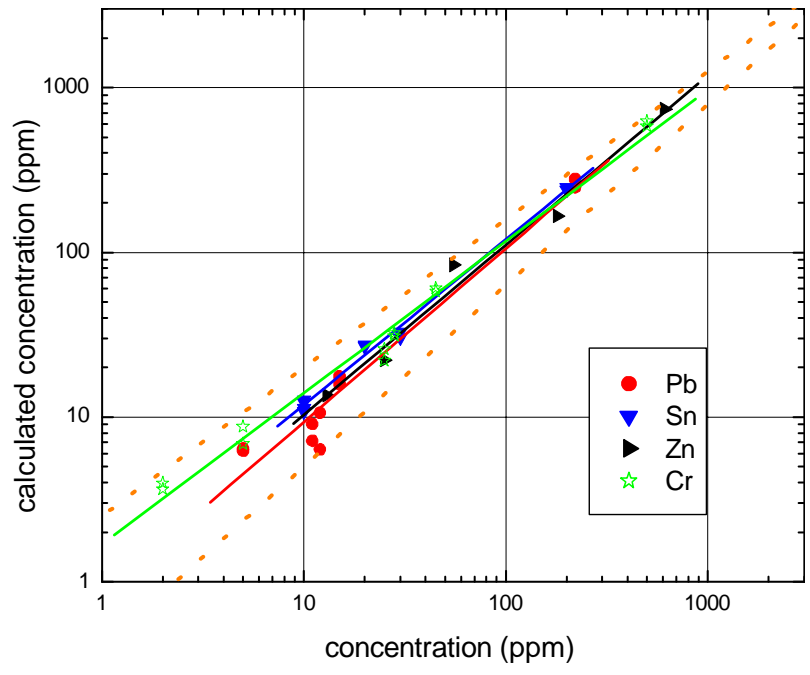


Figure 6-16: Calibration lines of Pb, Sn, Zn, and Cr in aluminium. Internal standard  $^{24}\text{Mg}$ ; 2 measurements per sample. Dashed lines mark  $\pm 10\%$  deviation from the slope 1.

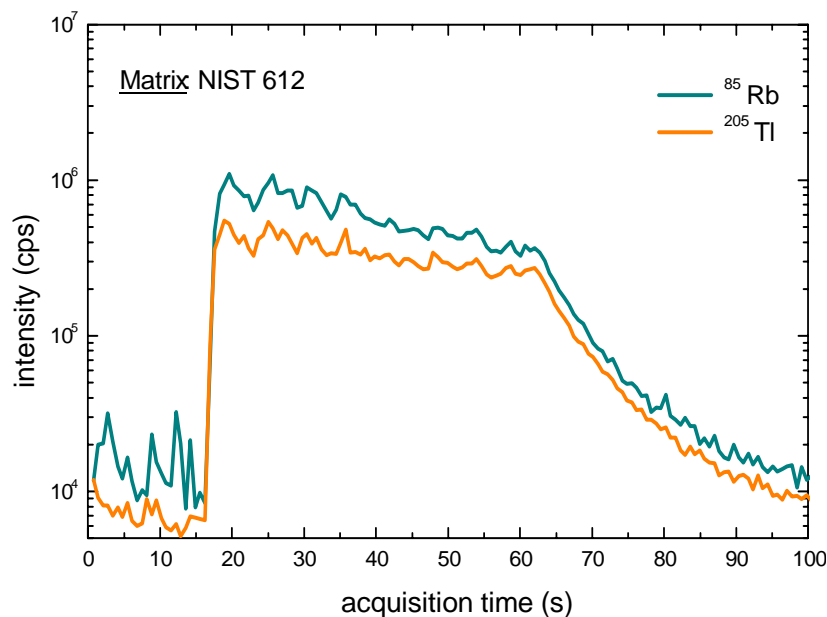


Figure 6-17: LA-ICP-MS signal intensity of  $^{85}\text{Rb}$  and  $^{205}\text{Tl}$  vs. the acquisition time for a NIST glass standard sample. Laser fluence  $50 \text{ J/cm}^2$ ; repetition rate 7 Hz.

### 6.2.2 Analysis of glass standards

In similar manner, measurements of trace elements in NIST glass standards were undertaken. The threshold fluences for ablation of glasses with a laser of 775 nm and 200 fs are typically one order of magnitude higher than for metals ( $1\text{-}2 \text{ J/cm}^2$ ) [60]. During the measurements, the fluence was  $50 \text{ J/cm}^2$ . The sample surface was cleaned with 5 laser shots prior to each measurement. A typical ICP-MS signal from a glass sample is shown in Figure 6-17. The repetition rate had to be reduced to 7 Hz in order to keep the signal intensity constant sufficiently long for the ICP-MS measurement. Apart from that, the routine is the same, and the calibration graphs are linear. Figures 6-18 and 6-19 show the calibration graphs for Rb and Tl respectively.

Three measurements were made per sample, integration time was 40 s and  $^{43}\text{Ca}$  was used as the internal standard. Detection limits in lower ppb range are of the same order of magnitude as obtainable with UV nanosecond lasers, that are conventional in LA-ICP-MS [6].

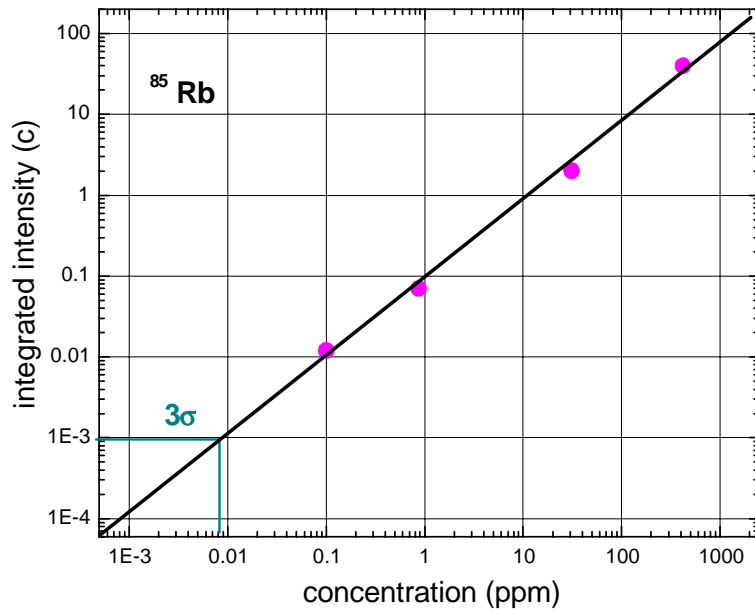


Figure 6-18: Calibration line of Rb in glass. Internal standard  $^{43}\text{Ca}$ ; 3 measurements per sample. Error bars are smaller than the symbols (10% rel.).  $3\sigma$  detection limit is 8 ppb.

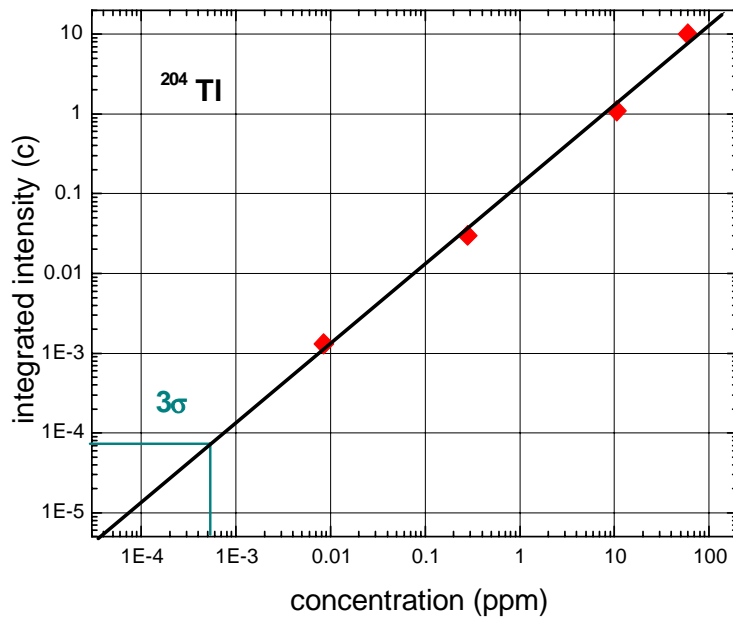


Figure 6-19: Calibration line of Tl in glass. Internal standard  $^{43}\text{Ca}$ ; 3 measurements per sample. Error bars are smaller than the symbols (10% rel.).  $3\sigma$  detection limit is 0.5 ppb.

## Chapter 7

# In-depth Profiling

The reduced thermal diffusion is a valuable property of the ultrashort laser's interaction with solids which enables material removal with sub-micrometre precision. Ablation of less than 10 nm per shot has been demonstrated [8, 54, 100], and that is close to depth resolutions of the best established in-depth analysis techniques, such as SIMS (Secondary Ion Mass Spectrometry) and GD-MS (Glow Discharge- Mass Spectrometry), typically 5-10 nm. At the same time those techniques have different lateral resolutions, in the range from 100 nm (SIMS) to a few mm (GD-MS). The laser focus size is in the middle of that range (normally 10 to 100  $\mu\text{m}$ ), but in principle is the lateral resolution of laser ablation diffraction limited. The best results of LA in-depth profiling could be expected at ultra-high vacuum (UHV) conditions that are necessary for most of the established techniques, as will be discussed below, but laser ablation in-depth profiling could be performed also in the presence of a noble gas and at atmospheric conditions. That is significant for many possible applications where fast, online analysis is needed and UHV should therefore be avoided.

The controlled material removal is not sufficient for LA in-depth profiling. One needs a detection technique suitable for single shot multielement analysis. LIBS with an echelle spectrometer satisfies this condition, but there is a limitation imposed on the ablation rates: the laser fluences should be so high that a dielectric breakdown is reached and a plasma emission can be detected (the removed material should be atomised/ionised and excited). Alternatively, one of the tandem techniques could be used for detection, such as re-excitation with another laser pulse or transport of the ablated material into another plasma. Much lower fluences than

in classical LIBS can be applied for analysis in the TOF-MS, since ionic signals can be observed even for fluences that are below the threshold determined from the visible surface damage inspection (Section 4.1.3) [90, 101].

*In laser ablation in-depth profiling the elemental signals are taken as a function of the number of applied laser pulses.* The real depth information has to be obtained from an independent depth measurement. Alternatively, for materials for which the ablation rate dependence on fluence is known, the depth could be calculated from experimental parameters.

## 7.1 The goal of the study

Laser ablation in-depth profiling with nanosecond lasers has been demonstrated recently. Vadillo et al. [102] analysed metal coatings (Cr, Ni, Cu and Zn) with thicknesses 2  $\mu\text{m}$  per layer and 12  $\mu\text{m}$  thick Zn coating on steel by LIBS. García et al. [103] reported LIBS measurements on 500 nm- 1.5  $\mu\text{m}$  Sn layers as well as 1.5  $\mu\text{m}$  Cr films on Ni substrates. The metal coatings studied by Anderson et al. [104] (LIBS) were 0.5 to 5  $\mu\text{m}$  thick. Plotnikov et al. [105] reported the LA-ICP-MS measurements of 1.5-7  $\mu\text{m}$  thick Ti-containing hard coatings.

The idea of developing a laser ablation in-depth profiling method is so attractive since it could, in principle, be used for any sort of material. Potential advantages relative to glow discharge techniques include small crater size and rapid analysis. Opposed to the ion sputtering techniques (SNMS, SIMS, RBS), which have a depth range of the order of 1  $\mu\text{m}$ , LA can be performed in the atmospheric conditions and its depth range amounts tens of micrometres (depending on the lateral resolution).

*The goal of this study is to investigate the limits of feasibility of the femtosecond laser ablation in-depth profiling.* It shows that much thinner layers than those mentioned above can be resolved. The thin metallic films used here are difficult samples for laser ablation in-depth profiling. Due to their good electrical and thermal conductivity, the electron heat penetration depth and therefore the ablation depth (see Section 2.2) is higher than of dielectric materials, which limits the achievable depth resolution. However, they represent problems that are important for practical applications. Hard and non-conducting Ti-containing coatings [105, 106], as well as some other transition-metal nitrides and carbides [107] can be microstructured

with high precision with ultrashort lasers, so that a better depth resolution can be expected. At this stage of research, the quality of sampling with laser ablation is of main concern. Therefore, only qualitative elemental analysis of layered structures will be performed.

The laser crater geometry, directly connected to the beam intensity distribution, has a decisive influence on the profiling results. Several methods of beam shaping will be discussed in Section 7.6.

## 7.2 Definition of depth resolution

Results of in-depth profile measurements should be the element concentrations ( $c$ ) as functions of the depth ( $z$ ). The depth resolution ( $\Delta z$ ) for step-like profiles is given by [108]:

$$\Delta z = \frac{\Delta c}{\left(\frac{dc}{dz}\right)_{\max}}$$

Since the signal intensity  $I$  is proportional to the concentration and the depth to the number of applied laser pulses  $N$  (assuming constant energy and ablation rate  $L_\alpha$ ), the following relation is valid:

$$\Delta z = \Delta N * L_\alpha = \frac{\Delta I}{\left(\frac{dI}{dN}\right)_{\max}} * L_\alpha. \quad (7.1)$$

According to [105],  $\Delta N_{layer}$  and  $\Delta N_{substrate}$  can be determined as shown in Figure 7-1. It is possible that the plateau of the substrate signal is not reached. In that case the depth resolution can be estimated by [105]

$$\Delta z = \Delta N_d * L_\alpha \quad (7.2)$$

where  $\Delta N_d$  is the difference between the pulse numbers for which the signals of elements in the layer and in the substrate start to rise.

There is a clear distinction between the ablation rate and the depth resolution. A low ablation rate is necessary for good depth resolution, but the detection method (e.g. signal accumulation from several pulses and apparatus response) as well as the thickness of the interface between the two layers and geometry of the crater will influence the depth resolution.

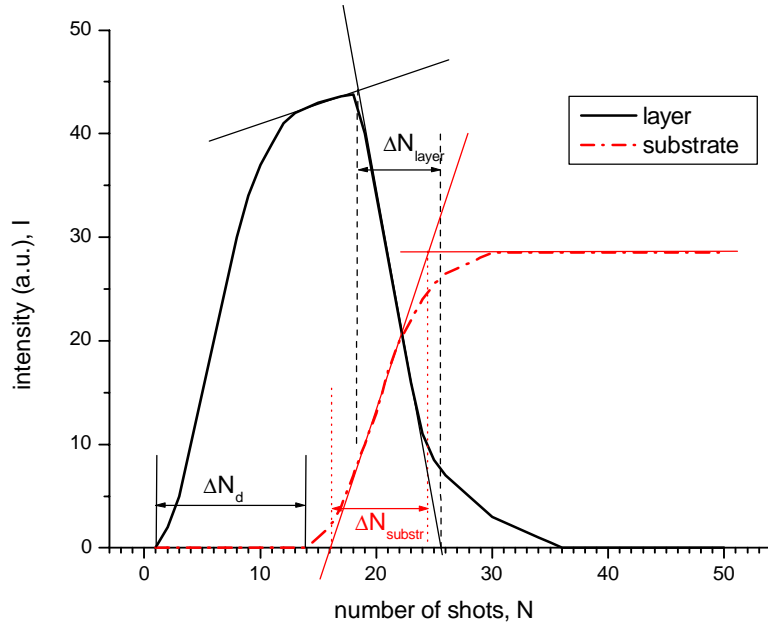


Figure 7-1: Depth resolution for laser ablation in terms of the number of pulses  $\Delta N$  is evaluated from the  $I(N)$  profiles for the surface layer (full curve) and the substrate (dot-dashed curve).

### 7.3 Cu-Ag layers on Si - LIBS

The first fs-LIBS in-depth measurements of multilayered structures were performed on double and triple Ag-Cu sandwich layers on a silicon substrate. These and the Cr and Ni layered samples (Section 7.7) were prepared by thermal vapour deposition in vacuum (Balzers, BA 710 V) at ISAS-Dortmund. For better adhesion, a 2 nm layer of Cr was initially deposited on a clean silicon surface. The thickness of each Cu and Ag layer was about 600 nm. An example of the line intensities obtained during ablating through the triple Cu-Ag sandwich sample under argon atmosphere is shown in Figure 7-2. In order to obtain a better depth resolution, the laser fluence was kept low but it had to be high enough to reach the dielectric breakdown and for LIBS signals to be detected. The value of about  $1 \text{ J/cm}^2$  satisfied the later condition. The light from each ten subsequent pulses was accumulated and the signals were **normalised to the sum**, as it is customary for in-depth profiling. The normalised line intensities of each element ( $I_{el}^{norm}$ ) are divided by the sum of the normalised intensities of all the elements detected for a



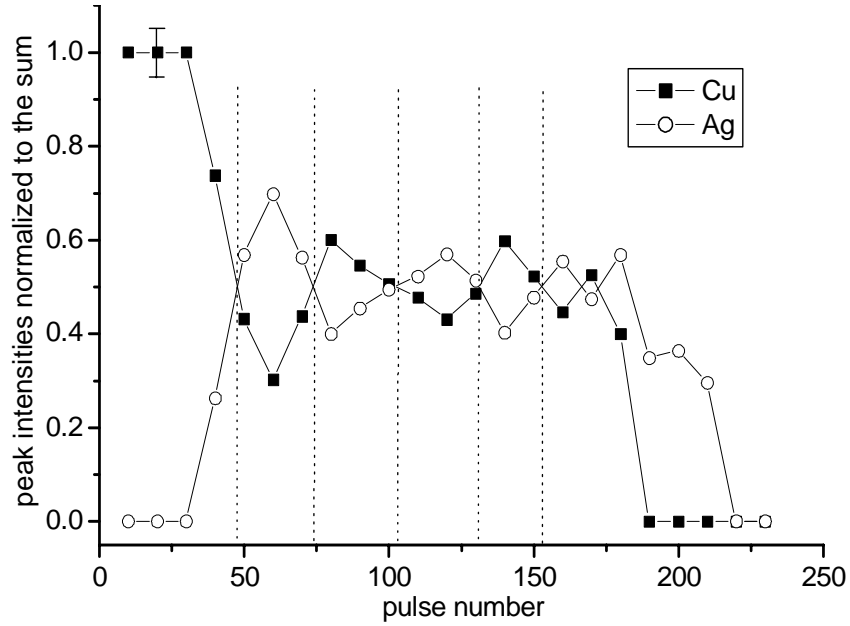


Figure 7-2: Depth profiling of three Cu-Ag sandwich layers on a silicon substrate by femtosecond LIBS. The dashed lines indicate approximate boundaries of the layers.

given depth or a pulse number:

$$I_{el}^{norm.sum}(N) = \frac{I_{el}^{norm}(N)}{\sum_{all\ el} I_{el}^{norm}(N)}.$$

As seen from the Figure 7-2, only the first two layers can be well discriminated. The silicon line intensity was detected after about 180 laser pulses, giving for *the mean ablation rate in the crater centre* about 20 nm per pulse. Applying the equation 7.1 to the top Cu layer gives a depth resolution of 500 nm. The facts that the intensity of the Cu line does not fall down to the background level after the first layer of copper and that the contrast ratio declines with the number of layers is attributed to the Gaussian profile of the laser beam. A SEM image of a crater in a Cu-Ag single sandwich sample obtained after 80 pulses of 0.9 J/cm<sup>2</sup> at the argon pressure of 30 mbar is shown in Figure 7-3. The upper Cu and the successive Ag layer, both 600 nm thick, are totally ablated in the centre of the crater while only partially removed in the outer regions. There are no traces of melting or mixing of the layers - the resolution for deeper layers is lost mainly because after the first layer has been removed in the middle of the crater,

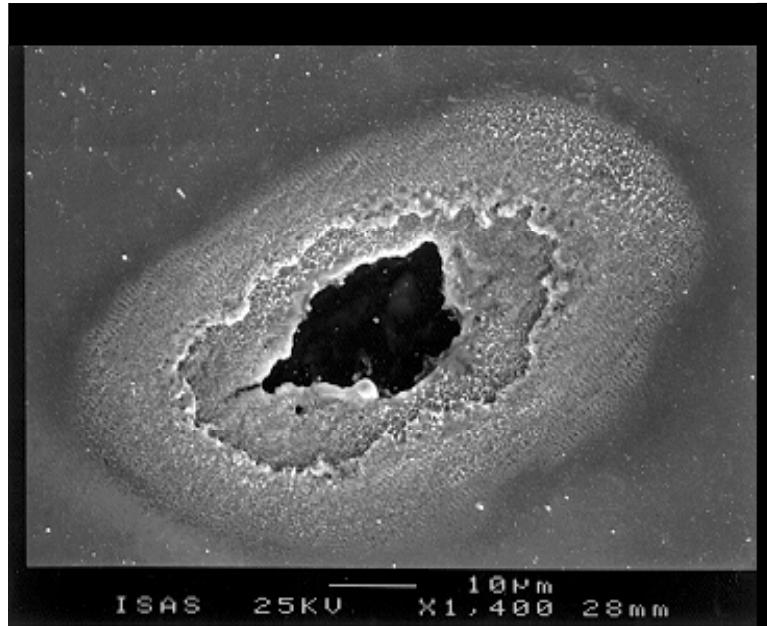


Figure 7-3: SEM image of a crater in a Cu-Ag single sandwich sample obtained after 80 pulses of  $0.9 \text{ J/cm}^2$  at the argon pressure of 30 mbar.

there are still contributions from the crater edges to the signal during the subsequent pulses.

#### 7.4 TiAlN-TiN on steel - LA-TOF-MS

Quintuple TiAlN-TiN layers on steel (sample DCPB 126 III) were prepared and characterised by the glow discharge (GD) technique at the Institut für Festkörper- und Werkstofforschung (Dresden, Germany). The total thickness of the coatings is  $2.8 \mu\text{m}$  and each single layer is 280 nm thick. Figure 7-4 shows the results of the GD analysis. The nitrogen content is almost constant throughout the layers.

The sample “126 III” was placed in the TOF-MS chamber as shown in Figure 4-4. Ions that are created during the laser ablation process are sent into the TOF spectrometer (Section 4.3). Two typical mass spectra of the TiAlN-TiN-steel sample are presented in Figure 7-5. Signals from eight subsequent laser pulses were accumulated. In the upper spectrum, starting with pulse No. 49, ions of Al and Ti are present. The lower spectrum, starting from pulse No. 617, contains in addition the signals of Cr, V and Fe, indicating that the substrate has been reached.

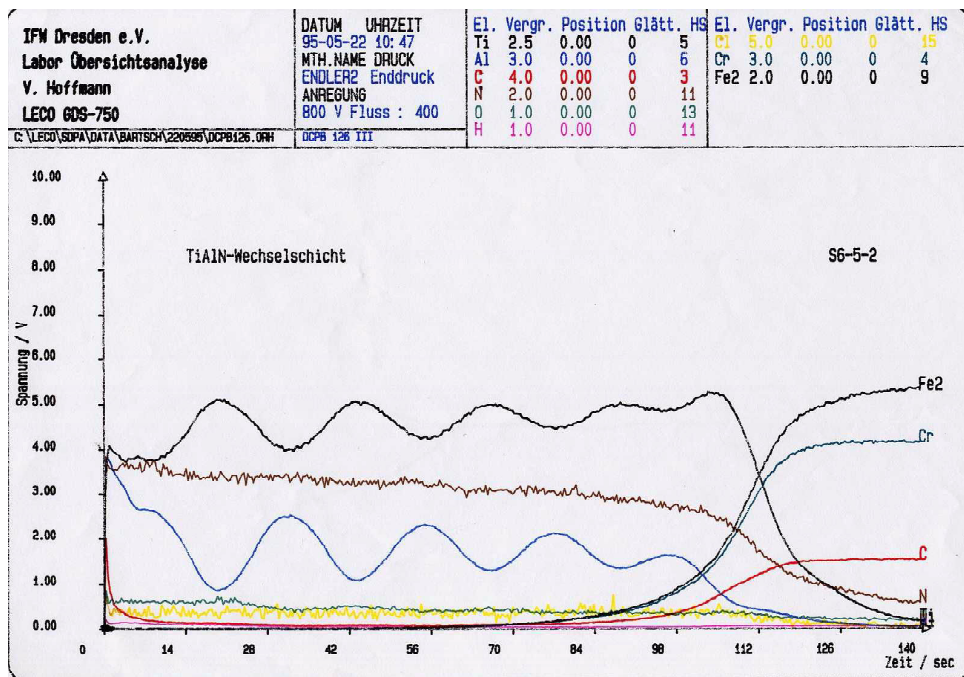


Figure 7-4: Glow discharge depth profile of the quintuple TiAlN/TiN structure (total thickness 2.8  $\mu\text{m}$ ) on steel substrate (sample "126 III") performed at IFW Dresden.

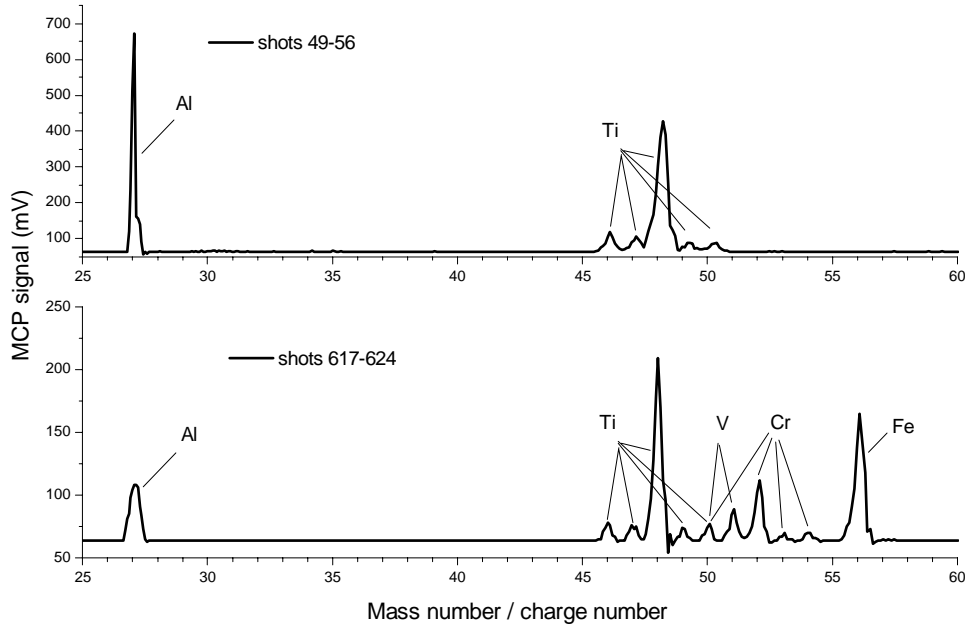


Figure 7-5: LA-TOF mass spectra obtained by fs laser ablation of a TiAlN/TiN sample. upper spectrum: integration of shots 49-56; lower spectrum: shots 617-624.

Figures 7-6 and 7-7 show two depth profiles measured by the described femtosecond LA-TOF-MS. For the applied fluences of  $0.35 \text{ J/cm}^2$  and  $0.37 \text{ J/cm}^2$ , the steel substrate has been reached after 220 and 160 laser pulses, respectively. That corresponds to the ablation rates of 13 and 17 nm per pulse in the crater centre. As in the previous example (Section 7.3), the signals were normalised to the sum of the normalised line intensities. The dashed lines which indicate approximate layer boundaries are shown to guide the eye. Different distances between them are attributed to the differences in ablation rates of the two materials and to pulse-to-pulse energy fluctuations. Each 280 nm thick layer was ablated by about 20-25 laser pulses, giving the mean ablation rate of 11-14 nm per pulse. The depth resolution for these two LA-TOF-MS measurements, according to eq. 7.1, varies from 125 nm for upper layers to 250 nm for lower layers. This is of the same order of magnitude, as in the GD-OES measurement in Figure 7-4 (140 nm to 280 nm). Despite the Gaussian beam profile, all ten layers can be resolved. The experimental conditions have certainly contributed to this result: high sensitivity of the TOF-MS allowed ablation with very low fluences, whereas the UHV of  $10^{-6}$  mbar simultaneously

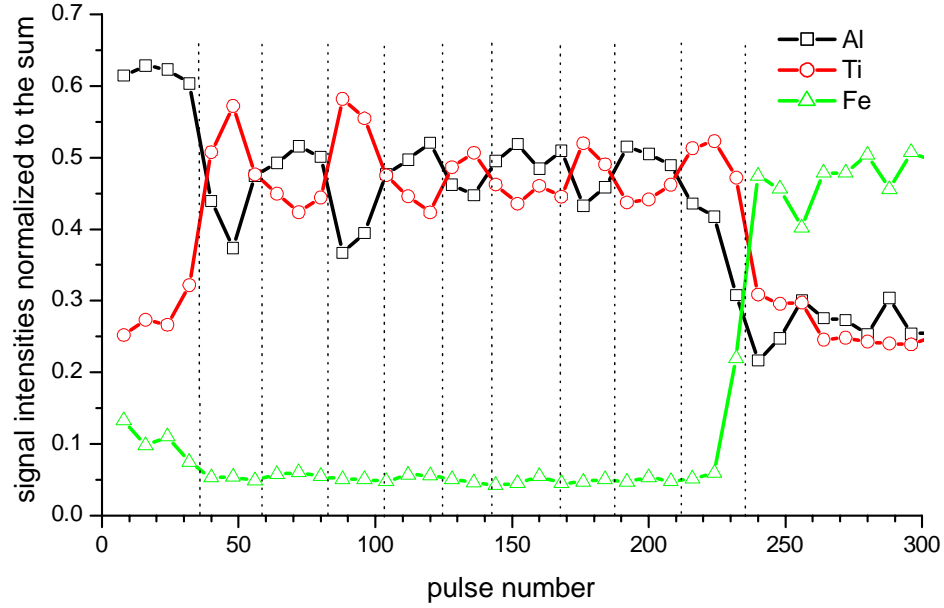


Figure 7-6: Depth profile of the TiAlN/TiN quintuple sandwich sample measured by fs-LA-TOF-MS. The ion signals are normalized to the sum of all ion signals. Laser fluence  $0.35 \text{ J/cm}^2$ . Dashed lines indicate approximate layer boundaries.

guaranteed for the minimal material redeposition. However, it is the very low thermal diffusion of hard coating materials such as TiN and TiAlN (that makes them suitable for fine and high precision microstructuring with ultrashort lasers [106]) that enables the LA in-depth profiling with high resolution. Figure 7-8 shows the SEM image of one of the craters in the analysed sample. It was created by 100 laser pulses (fluence:  $0.35 \text{ J/cm}^2$ ) with a Gaussian beam profile. Several layers can be seen without significant mixing and the ablated surface is very smooth.

## 7.5 Co implanted silicon wafer

A silicon wafer with thin and shallow implanted layer of Co ions ( $10^{17} \text{ ions/cm}^2$ ) has been analysed by fs-LA-TOF-MS. An equal sample has been previously investigated at ISAS by total reflection X-ray fluorescence spectrometry (TXRF) combined with wet chemical etching, as well as by Rutherford backscattering spectrometry (RBS) [109]. The results of these two methods are shown in Figure 7-9. The total depth over which the ions are distributed

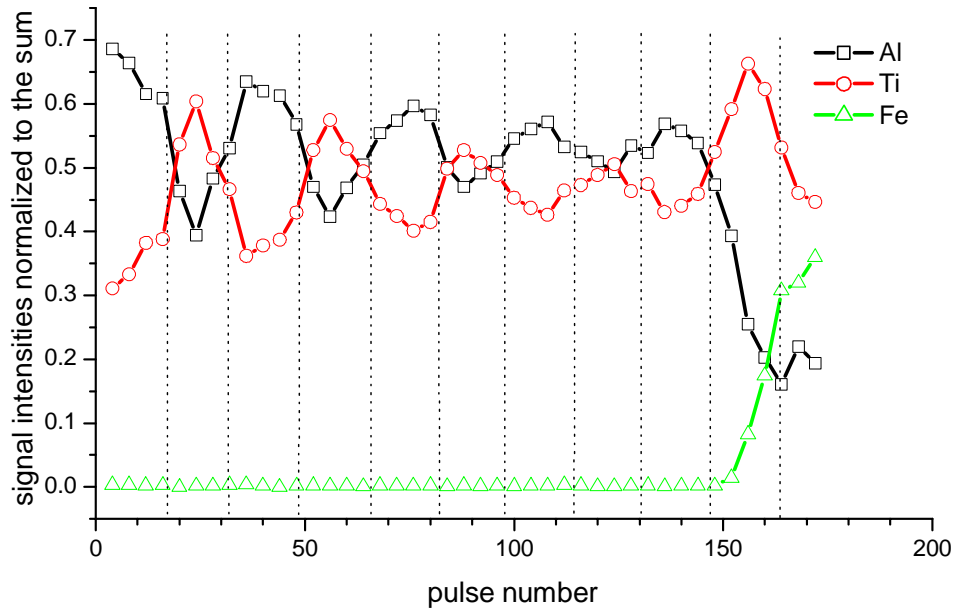


Figure 7-7: Depth profile of the TiAlN/TiN quintuple sandwich sample measured by fs-LA-TOF-MS. The ion signals are normalized to the sum of all ion signals. Laser fluence  $0.37 \text{ J/cm}^2$ . Dashed lines indicate approximate layer boundaries.

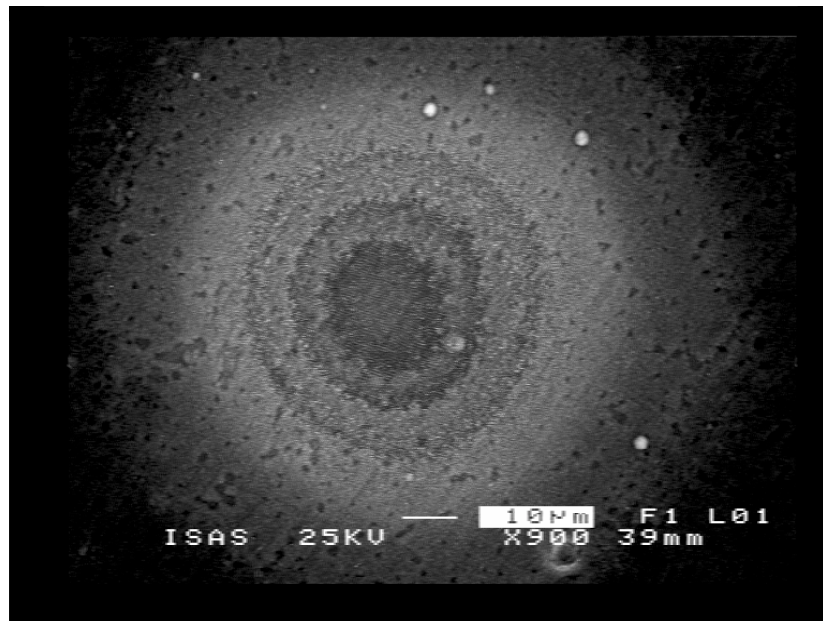


Figure 7-8: SEM image of a crater in the TiAlN/TiN multi-layer sample after 100 laser shots of  $0.35 \text{ J/cm}^2$  fluence.

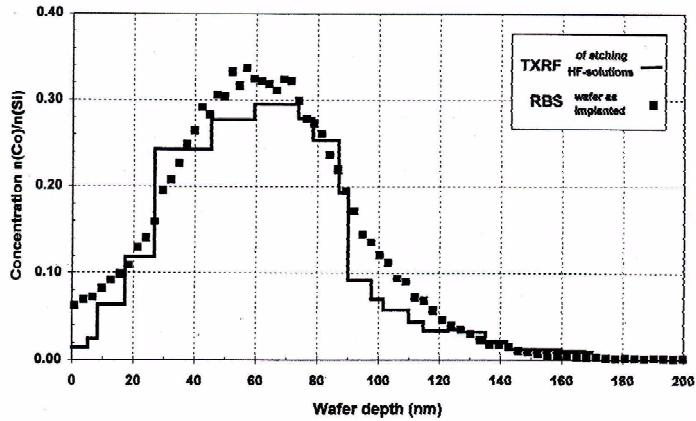


Figure 7-9: Concentration-depth profiles for the Si wafer with Co implantation ( $10^{17}$  ions  $\text{cm}^{-2}$ ) determined by TXRF of etching solutions after repeated etching and by RBS of the original non-etched wafer ('as implanted'). From Klockenkämper et al. [109].

is about 150 nm, while the thickness at the half of the maximum Co concentration amounts about 60 nm. The results of the LA-TOF-MS analysis together with the results of RBS [109] are presented in Figure 7-10. Due to relatively small dynamic range of the MCP detector, the LA-TOF-MS signal of the main component, silicon, was saturated. It was therefore not possible to obtain any information about the relative concentrations. From the comparison with the measurements of Klockenkämper et al. [109] the mean ablation rate can be estimated to be about 4.5 nm per pulse. Even though the repeatability of these first measurements on this sample was not too high, this result clearly indicates that depth resolution of fs-LA-TOF-MS in-depth profiling can be better than 100 nm.

One of the main limitations in the above measurements is the uneven ablation rate distribution across the crater, due to Gaussian intensity profile of the laser beam. In the following, efforts to solve this problem will be presented.

## 7.6 Beam Shaping

The shape of a beam of optical radiation is defined by its spatial irradiance distribution, and the process of redistributing *the irradiance and the phase* is called beam shaping. For incoherent beams, there is only a demand on the irradiance distribution at a target plane, while for

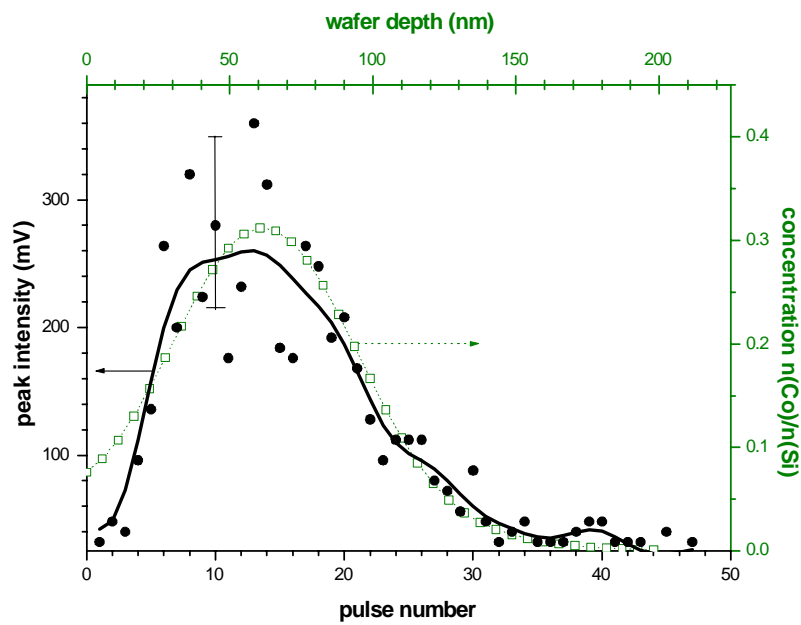


Figure 7-10: ●: LA-TOF-MS intensity-pulse number profile for the Si wafer with Co implantation ( $10^{17}$  ions  $\text{cm}^{-2}$ ); full line: fast Fourier transform smoothed LA-TOF-MS intensity. □: RBS of the original non-etched wafer ("as implanted") [109].



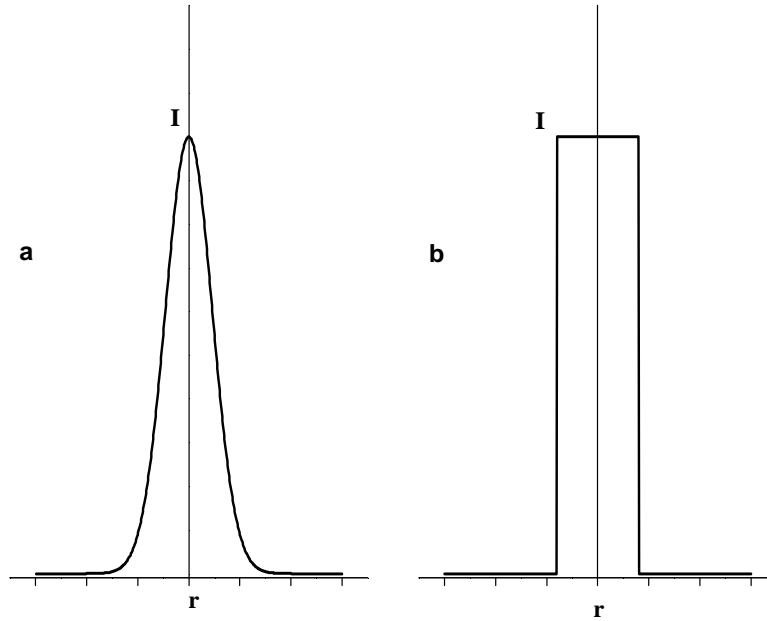


Figure 7-11: Radial intensity distribution of the (a) Gaussian laser beam and (b) flat-top laser beam.

coherent beams constraints on the phase may be required as well (e.g. the collimated output beam must have a uniform phase front). In some applications, it is advantageous that the shaped beam propagates with the desired profile over longer distances, instead of having the wanted properties only at the target plane. A number of low-loss or lossless techniques are systematically treated in [110].

The problem of converting a Gaussian beam (Figure 7-11a) into a flat-top distribution (Figure 7-11b) is of interest for in-depth profiling. Different reflective, refractive or diffraction based systems [110] can be constructed to achieve a more or less uniform flat-top irradiance distribution. However, for the ultrashort, high intensity pulses certain additional restrictions hold. Methods involving too many dispersive elements will prolong the pulse duration, while intermediate focusing in atmospheric conditions may cause a breakdown through which the phase front and the wanted intensity distribution will be destroyed.

The application of ultrashort pulses for depth profiling with good depth resolution requires low pulse energy. Therefore, more attention was paid to the simplicity and robustness of solutions as well as preserving the temporal pulse properties than to the low-loss aspect of the

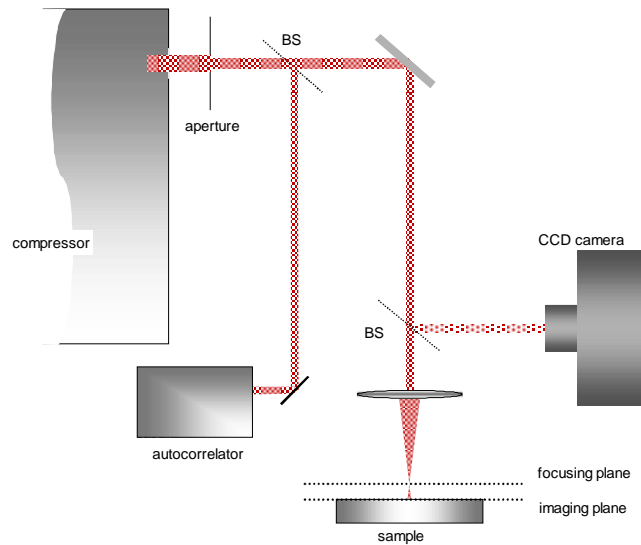


Figure 7-12: Scheme of the experimental arrangement for beam shaping by imaging of an aperture onto the sample surface. The positioning of the aperture has to be controlled by the CCD camera. BS = beam splitter.

problem. In the following, several approaches will be described:

- the truncation of the Gaussian beam with an aperture
- the reflection by the graded reflectivity mirror
- the spatial modulation by a liquid crystal display.

### 7.6.1 Imaging

The simplest method to obtain a flat-top is the imaging of an aperture placed in the nearly homogeneous part of the beam profile (Figure 7-12). The demagnification factor necessary to obtain craters in the range of 20-100  $\mu\text{m}$  diameter from 2-3 mm aperture is between 30 and 100. It follows from the lens equation ( $\frac{1}{a} + \frac{1}{b} = \frac{1}{f}$ ) that the aperture has to be placed 3-5 m in front of the lens (100 mm focal length) and the image position is several mm behind the focus plane. As mentioned above, this method is appropriate only for very low energy densities (or for vacuum conditions), since a breakdown above the sample surface would destroy the phase

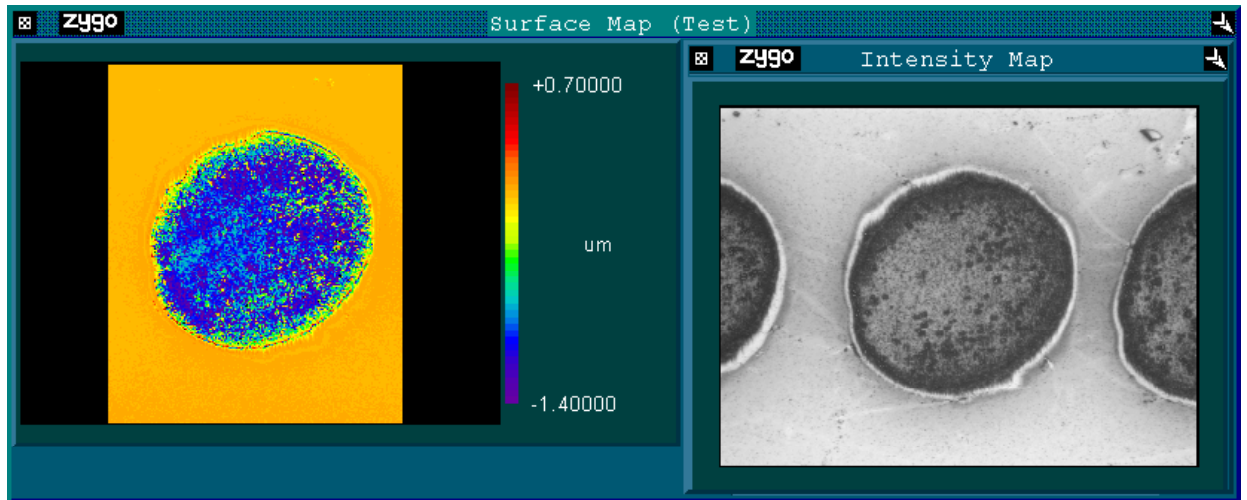


Figure 7-13: The flat bottom craters on the surface of the NIST SRM 2135c sample, created by the aperture imaging and measured by white light interferometry.

front. When the sample surface coincides with the image plane, craters with flat bottom and vertical walls are created (Figure 7-13). The critical factors of this method are

- (i) the positioning of the aperture on a homogeneous part of the beam which has to be controlled with a CCD camera (the beam has a very long path through the laser system and sometimes slightly changes the propagation direction);
- (ii) the positioning of the sample in the image plane. Already 200  $\mu\text{m}$  in front or behind it, a diffraction pattern can be observed which gives the crater shape as in Figure 7-14.

This is the best and a low-cost method as long as the variation of energy across the aperture is small enough. It is in wide use in laser lithography where masks of great complexity are projected onto the sample surface to alter its properties during the pattern production.

To compensate for the uneven energy distribution in the centre of the beam, a **graded reflectivity mirror (GRM)** has been designed and produced (INO, Sainte-Foy, Québec, Canada). The reflectivity profile and the expected and measured beam shapes are shown in Figure 7-15. The angle of incidence should be as small as possible, and the beam width on the GRM should be precisely the one for which it was designed (beam expansion is not necessary). Due to a steep reflectivity step on the edges, diffraction rings are expected after the beam reflection. Therefore, the GRM should be imaged onto the sample surface. The resulting

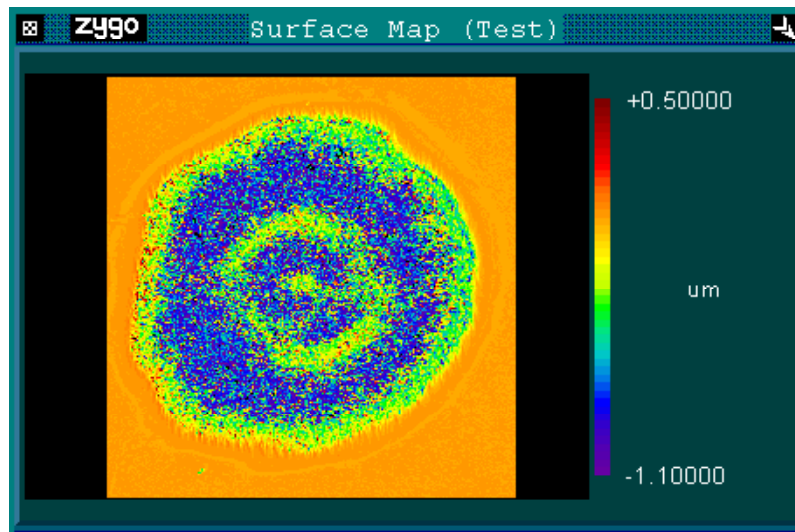


Figure 7-14: White light interferometer measurement of a crater in NIST SRM 2135c sample: diffraction pattern out of the aperture's image plane results in a crater with ring-shaped depth variation.

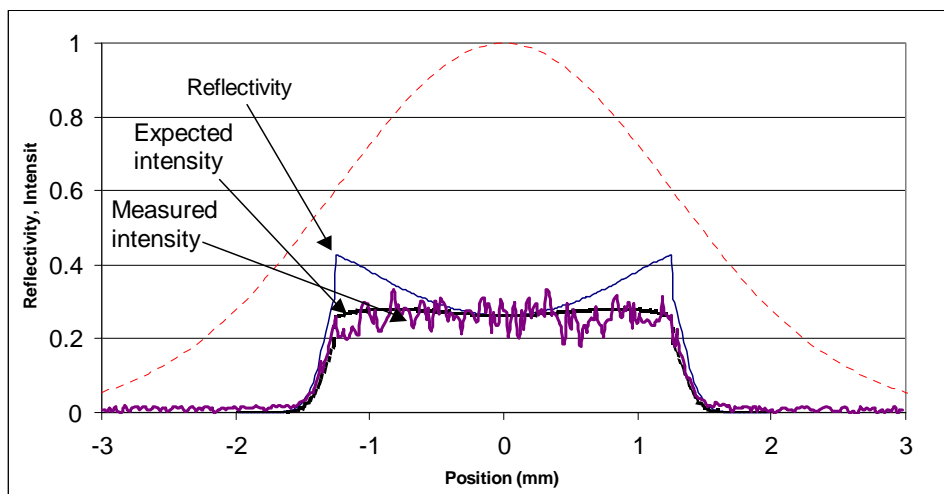


Figure 7-15: Reflectivity of the GRM; starting, Gaussian radial beam intensity distribution(dotted line); expected resulting, flat-top intensity distribution, and measured resulting intensity distribution.

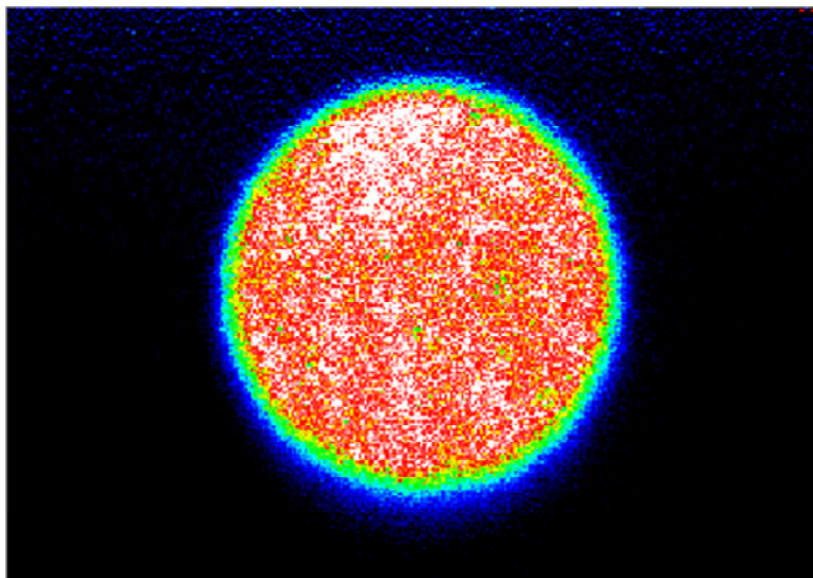


Figure 7-16: Beam shaping with the GRM: GRM imaged on the CCD camera detector plane.

intensity distribution is shown on Figure 7-16. Energy losses amount up to 85%. The other critical factors are the same as for the described aperture imaging- precise centering of the beam on the mirror and positioning of the sample in the plane of the image.

In order to determine the image plane position, the sets of craters for different lens-sample distances were produced. The sample was taken out of the chamber and then inspected under an optical microscope, but the repeatability of the sample (re)positioning was often not good enough. Due to the shallow depth of focus, a  $200\ \mu\text{m}$  difference in the sample position is enough to observe a diffraction pattern instead of the image. A method which is insensitive to the sample positioning had to be found, since an in-situ optical microscope that would prevent these practical difficulties was not available. An application of liquid crystal based spatial light modulators (SLM) is one of the possibilities.

### 7.6.2 LCD-Spatial Light Modulator

LC2002 (HoloEye GmbH) is a spatial light modulator based on a monochrome, transparent, twisted nematic liquid crystal display (SONY LCX0 16AL-6). It can be used as a diffractive optical element which modifies the phase front or as an intensity modulator, described below.

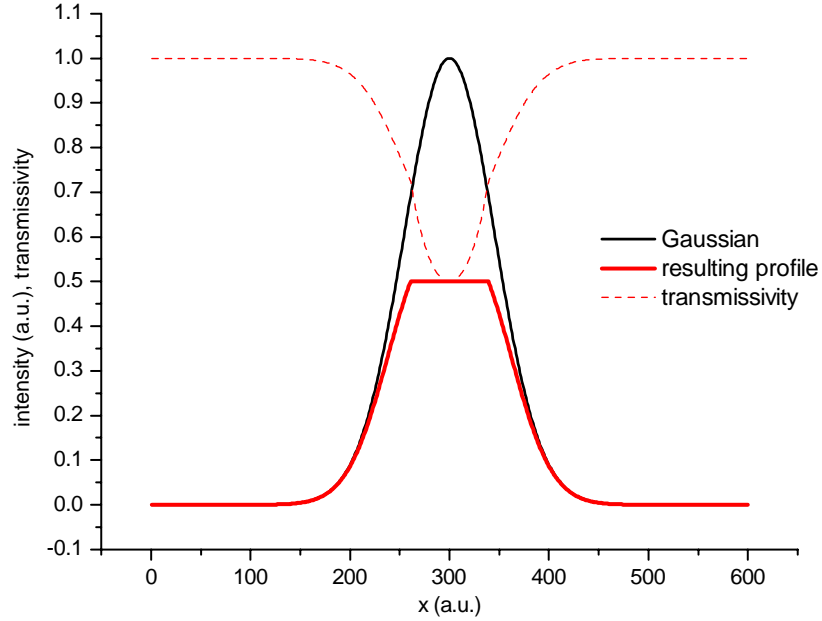


Figure 7-17: Transmissivity profile for converting a Gaussian beam into a flat-top with the SLM.

The device is plugged into the graphics board of a personal computer and the screen image (SVGA, 600×800 pixel) is converted into the grey-level signal, corresponding to the voltage across the display. When used with a polariser in front and an analyser (at 90°) behind, the transmissivity of each pixel corresponds to the shade of grey. The pixel size of 32  $\mu\text{m}$  ensures very fine resolution, well suited for laser beam shaping. Details of the operation principle and the properties are given in the Appendix D.

A pattern should be designed which spatially modifies the Gaussian beam intensity at all planes along the beam propagation, without the necessity to image the SLM on the sample. Such a conversion of a Gaussian beam into a perfect flat-top is not possible, since the steep intensity drop on the edges of a flat-top profile requires a pattern equivalent to an aperture. A sharp edge in the pattern introduces a phase jump across the beam that results with diffraction effects. Therefore, the optimal modification is the one which creates a plateau in the centre of the beam and the wings remain Gaussian. Figure 7-17 shows one possible transmissivity profile and the expected resulting intensity profile. An example of the beam profile after passing the LCD and the polariser is shown in Figure 7-18. For the application of in-depth profiling, the

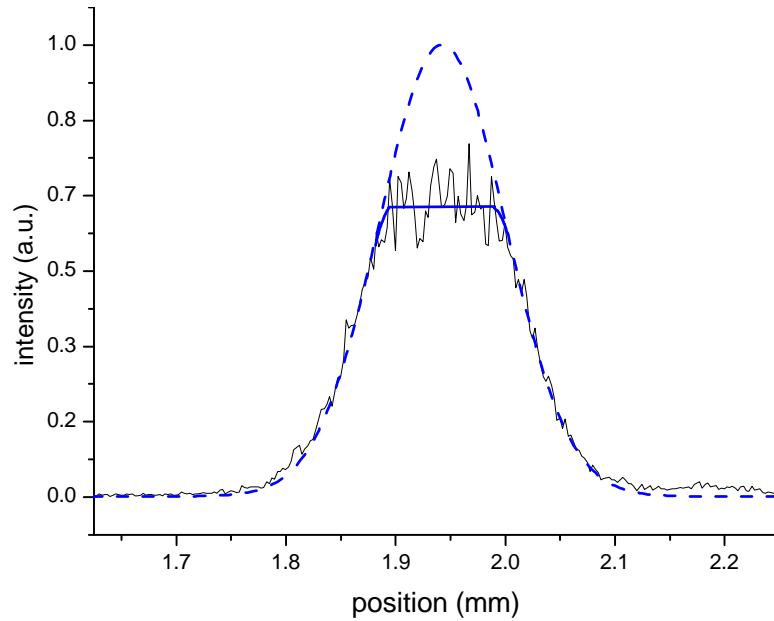


Figure 7-18: Beam profile shaped with the LCD.

beam wings do not represent a problem as long as the laser fluence is kept close to the threshold value and the ablation is effective only in the centre of the beam. The characteristic shapes of craters with steep walls and rather flat bottom are illustrated in Figures 7-19 and 7-20. They show the crater depth and a 3D image of a crater in a thin Cr film on silicon (Section 7.7) created by 20 laser shots. The beam was shaped with the LCD device as in the Figure 7-17.

## 7.7 Cr and Ni thin films on Si

The beam shaping with the aid of the LCD was used for the measurements on thin chrom and nickel films (produced at ISAS).

Figure 7-21 shows the results of a TOF-MS measurement on **a single Cr-layer on silicon (200 nm thickness)**, with the fluence of  $0.3 \text{ J/cm}^2$ . The silicon signal appears after 12 pulses, but decays together with the Cr signal. This will be explained below. In Figure 7-22, an average of three independent measurements in the same conditions as above is presented. The signals are normalized to the sum. The number of pulses for which transition from the layer to substrate is observed is reproducible. The thickness of the layer expressed through the number

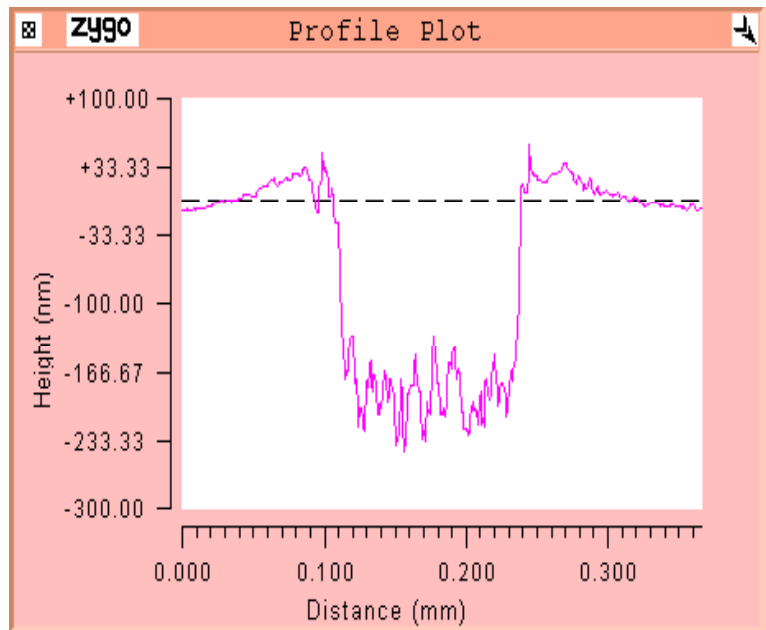


Figure 7-19: Profile of a crater created by the laser beam shaped with the aid of SLM as measured by the white light interferometer. (Cr film on silicon substrate, 20 laser shots, 40 mbar Ar.)



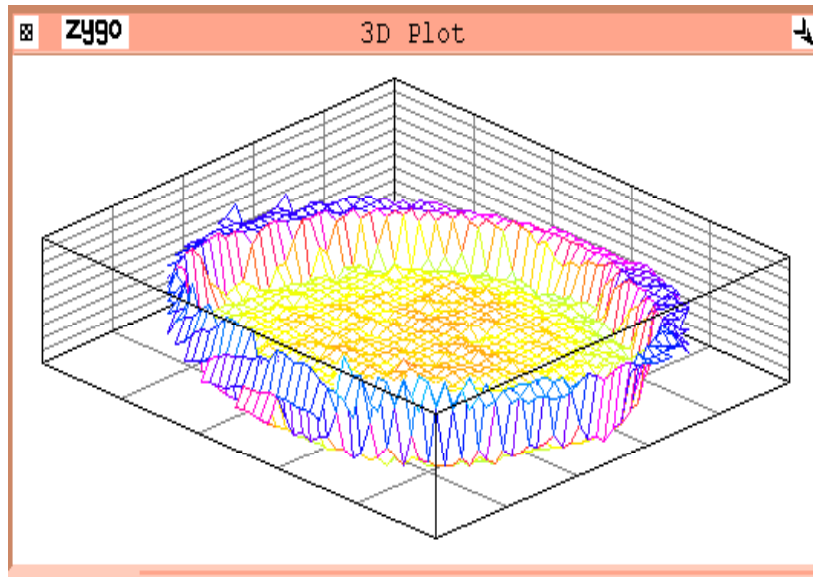


Figure 7-20: 3D representation of the crater from Figure 7-19, created by the laser beam shaped with the aid of SLM as measured by the white light interferometer. (Cr film on silicon substrate, 20 laser shots, 40 mbar Ar.)

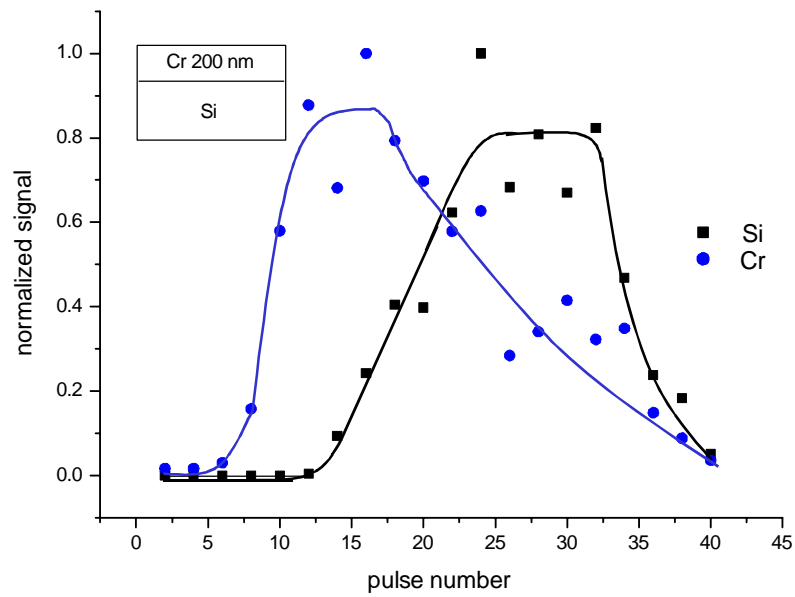


Figure 7-21: LA-TOF-MS depth profile of a 200 nm Cr film on silicon. The lines are guidelines for the eye.

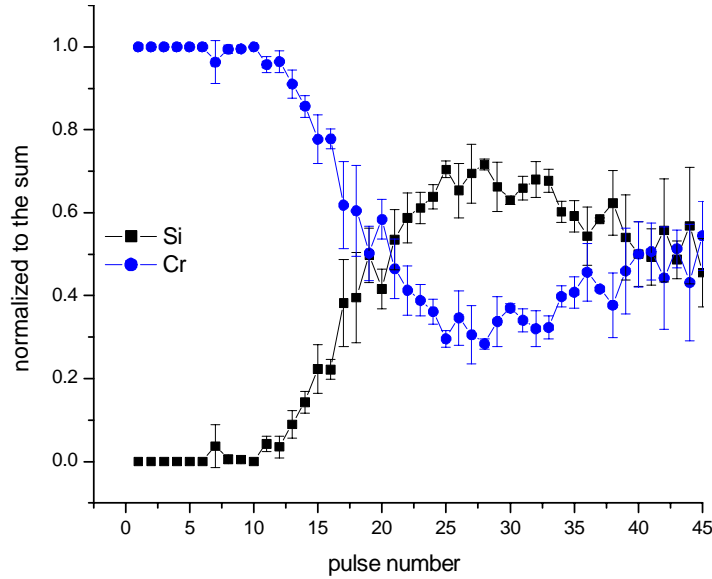


Figure 7-22: Depth profile of a 200 nm Cr film on silicon. Signals shown in Figure 7-21 are normalised to the sum. Each point is the mean value of three independent measurements with the same laser fluence ( $0.3 \text{ J/cm}^2$ ).

of pulses is, following this presentation, 16-20 pulses, which corresponds to the mean ablation rate of  $11 \pm 2 \text{ nm}$  per pulse. On the other hand, the silicon signal started to grow after only 12 pulses, so that at least at one part of the crater area the ablation rate was higher, about 16 nm per pulse.

Several craters were shot applying different numbers of laser pulses and then analysed with the white light interferometer. In that way, real depth measurements are obtained. The crater walls were steep and the bottom rather flat. Profiles of the craters created by a single pulse and by 19 pulses are shown in Figures 7-23 and 7-24 respectively. Note the difference in the scales of x and y axes. The pronounced crater edges can be attributed to the film edges, slightly unfolded due to the thermal stress. From this, it can be seen that the dimensions of the collateral damage on the edges are much smaller than  $1 \mu\text{m}$ . (Remember that the depth resolution of the white light interferometer is much better than the lateral resolution, Section 4.6.)

Depth measurements in the centre of the crater for different numbers of pulses are shown in Figure 7-25. They are in accordance with the TOF-MS results (Figures 7-21 and 7-22):

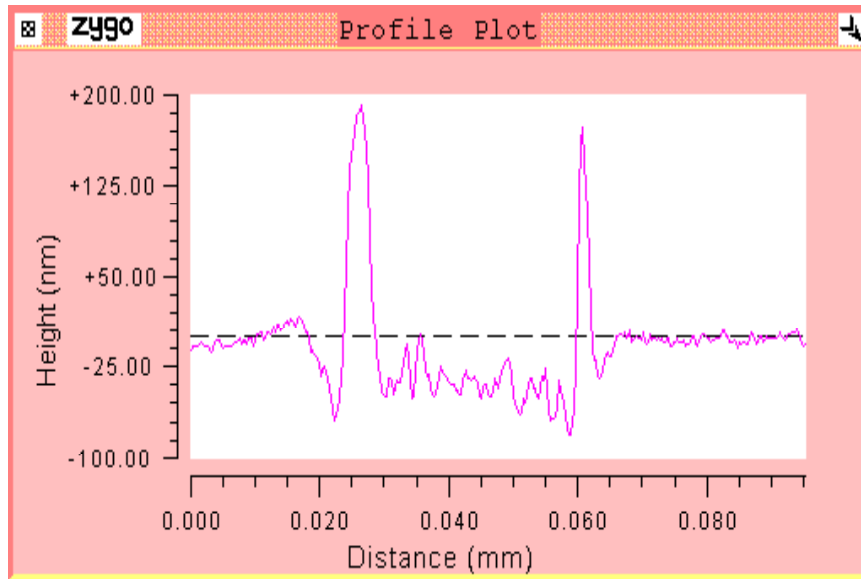


Figure 7-23: Profile of a crater in a 200 nm thick Cr film on silicon created by a single fs pulse of  $0.3 \text{ J/cm}^2$ . Note the difference in units on x and y axis.

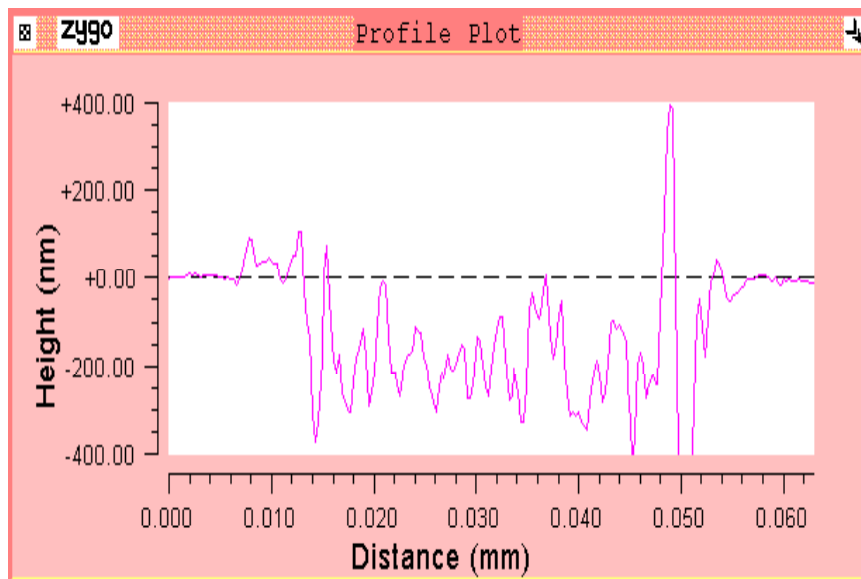


Figure 7-24: Profile of a crater in 200 nm Cr film on silicon, created by 19 pulses of  $0.3 \text{ J/cm}^2$ . Note the difference in units on x and y axis.

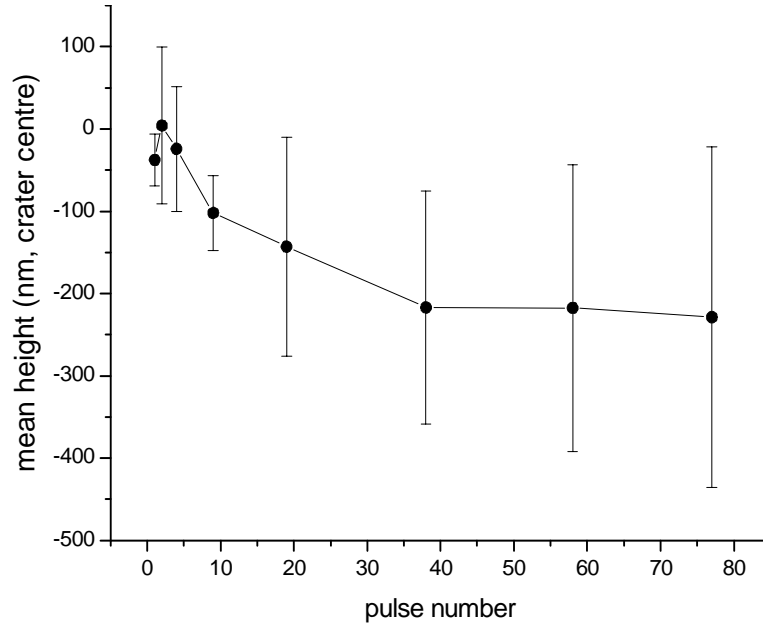


Figure 7-25: Central crater depth vs. the pulse number for a 200 nm Cr film on silicon;  $F= 0.3 \text{ J/cm}^2$ .

- the average depth of the 18 pulses crater is still smaller than the nominal layer thickness of 200 nm, but from the rms roughness of the crater bottom (expressed as error-bars) it is visible that some parts of the crater centre are below that level.
- The depth of the crater does not change anymore after 40 laser pulses, which coincides with the decay of the TOF-MS signals (compare Figure 7-21). The fluence ( $0.3 \text{ J/cm}^2$ ) is too low to ablate the substrate. Silicon could only be removed from the interface region.
- The ablation rate of the chromium layer estimated from the 100 nm average depth of the 9 pulses crater  $L_{Cr} \simeq 11 \text{ nm/pulse}$ , which is in accordance with the value estimated from the TOF-MS measurement, knowing that the thickness of the layer is 200 nm ( $11 \pm 2 \text{ nm/pulse}$ ).

Following the definition of depth resolution (eq. 7.1 and Figure 7-1), the TOF-MS measurements from Figure 7-22 have  $\Delta N_{Cr} \approx 9$  and  $\Delta N_{Si} \approx 11$ . The corresponding depth resolution for Cr layer is  $\Delta z_{Cr} = \Delta N_{Cr} * L_{Cr} \simeq 100 \text{ nm}$ . It was assumed here that the ablation rate of the pure

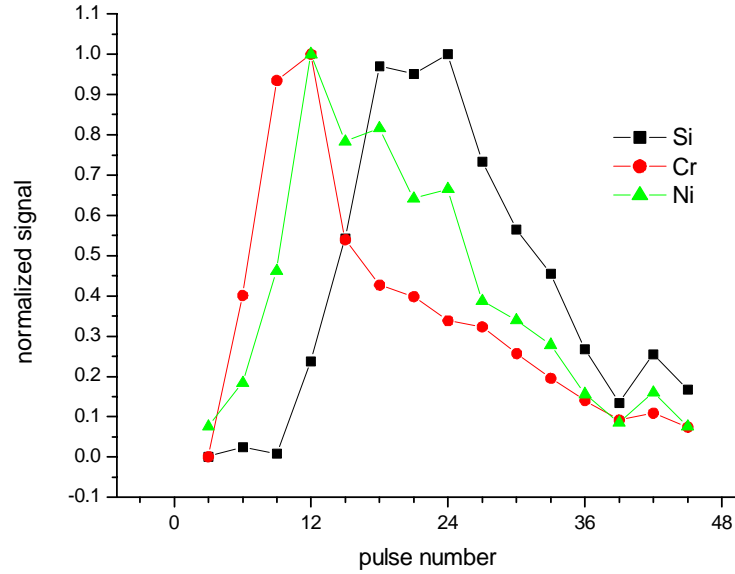


Figure 7-26: LA-TOF-MS depth profile of a multilayer Ni-Cr-Ni structure on silicon. Laser fluence  $0.4 \text{ J/cm}^2$ ; the signal was accumulated from each three subsequent pulses.

Cr layer is valid for the interface zone as well. However, according to the depth measurements (Figure 7-25), the ablation rate decreases when the substrate is reached, and from the  $10^{\text{th}}$  to  $22^{\text{nd}}$  pulse has a value of  $L_{\text{interface}} \approx 5 \text{ nm/pulse}$ . Thereby is the depth resolution for the Cr layer  $50 \pm 5 \text{ nm}$ .

The following example is a **three-layer structure Ni (80 nm)- Cr (100 nm)- Ni (100 nm)- Si**. Figure 7-26 shows the normalised signal from the LA-TOF-MS measurement with  $0.4 \text{ J/cm}^2$ . Each point represents the signal accumulated from three subsequent laser pulses. As in the previous measurement, the signals of all elements approach zero after 40 laser pulses. Figure 7-27 shows the signals normalised to the sum. Under these conditions, the depth resolution is of the order of the layer thicknesses so that the three layers can just be distinguished. For comparison, the craters were inspected with the white light interferometer. Figure 7-28 shows the mean depths in the central crater region of craters created by laser pulses of  $0.54 \text{ J/cm}^2$  and  $0.4 \text{ J/cm}^2$  as in the above TOF-MS measurement. The craters produced by  $0.4 \text{ J/cm}^2$  are not deeper than 400 nm, even after 120 applied pulses. Only the interface layer of silicon can be removed. The fluence of  $0.54 \text{ J/cm}^2$  was high enough to penetrate deeper into

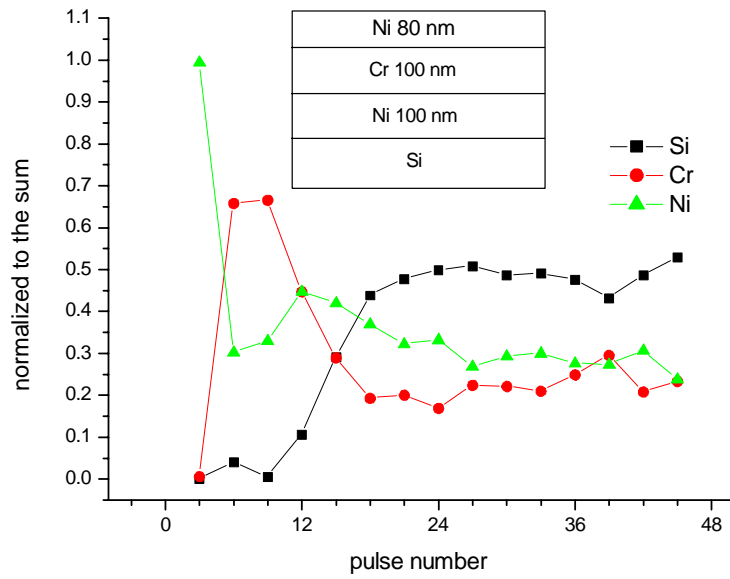


Figure 7-27: Depth profile of a Ni-Cr-Ni structure on silicon. Signals shown in Figure 7-26 are normalised to the sum.

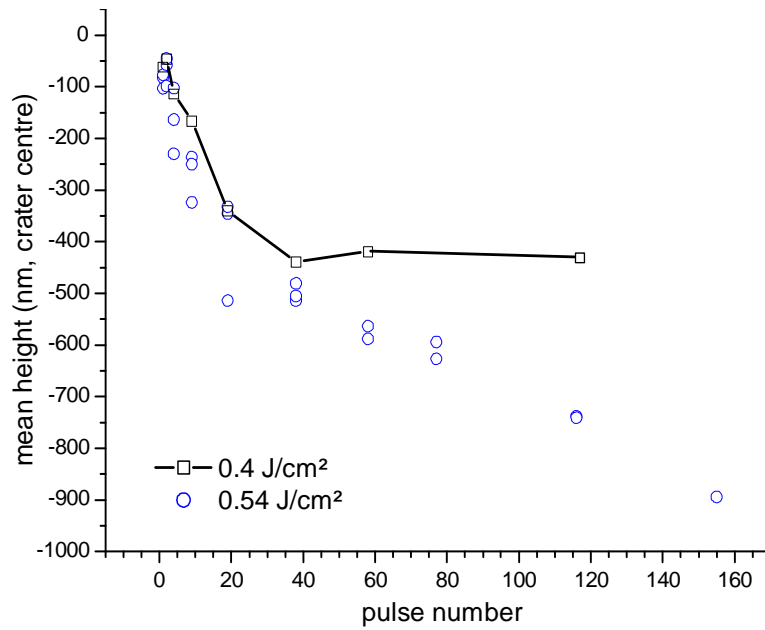


Figure 7-28: Central crater depth vs. the pulse number for a Ni-Cr-Ni structure on silicon obtained with 0.4 and 0.54 J/cm<sup>2</sup>.

the substrate. The ablation rate of the silicon is lower than for the metal films.

The depth resolution is estimated in the same way as for the Cr single layer measurements. The ablation rates were different for different layers: 28 nm/pulse during the first four pulses and 18 nm/pulse between pulse 4 and 20. The resolutions of the top Ni layer and the rise of the Cr layer are 83 nm, limited by the signal accumulation of each three pulses. The rise of the second Ni layer has the resolution of 54 nm and the fall of the Cr layer signal 100 nm. Obviously, the laser fluence and the number of accumulated pulses should be lower in order to achieve better resolution.

It is evident from these two examples that the laser fluence is a critical parameter. Its value should be above the ablation threshold of all materials in the profile. If the ablation rates and threshold fluences of the subsequent layers differ a lot, that might lead to a loss of depth resolution for the layer that is more easily ablated. In such cases the profiling with variable laser parameters should be considered. The matrix dependence of the removal rates is immanent to all of the in-depth profiling techniques.

**The NIST standard reference material 2135c** contains nine alternating Cr and Ni layers (57 and 56 nm thickness, respectively) on a silicon substrate. To resolve them, very low laser fluence should be applied. Even the slightest intensity differences across the laser beam can cause that several layers are being removed with a single pulse. In such a case the distinction of layers is impossible (see Figure 7-29). The imaging geometry as in Figure 7-13 was used, and the laser fluence was about 0.1 J/cm<sup>2</sup>. Although the individual Cr and Ni layers can not be distinguished, the interface with the silicon can be observed. The ablation started after 50 laser pulses and the films were removed during the next 300, giving for the mean ablation rate less than 2 nm per pulse. The used signal accumulation of each seven subsequent pulses would still allow the resolution of Cr and Ni layers, had the beam profile been completely flat and homogeneous. The variations of the Cr and Ni signals are correlated and they follow the laser energy fluctuations. Recall that the number of ions that reach the TOF-MS detector is not directly proportional to the laser pulse energy; the velocity distribution of ions created in the ablation process changes with laser energy, and only ions from a certain velocity interval are selected for the detection.

Under optimal conditions, as in Figure 7-30, clear alternating signals of the two elements

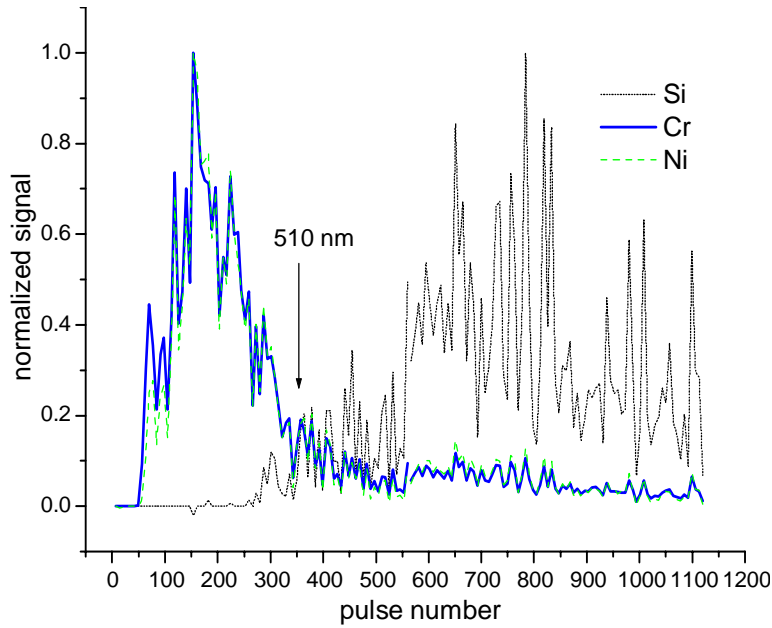


Figure 7-29: Fs-LA-TOF-MS depth profile of NIST SRM 2135c- normalized Ni, Cr, and Si signals. Laser fluence  $0.1 \text{ J/cm}^2$ .

can be obtained. The laser fluence was  $0.17 \text{ J/cm}^2$ , and signal from each pulse was stored separately. For some shots the ion signals of all elements were zero. These shots were excluded.

While working with the fluences close to the threshold value for a given material, the pulse-to-pulse energy stability of the laser becomes very important. Small fluence variations can cause significant differences in the ablation depth from one pulse to another, especially if the fluence of some pulses is below the threshold. This is illustrated in Figure 7-31. From the equation 2.4 for the dependence of the ablation rate on the laser fluence, follows

$$\frac{\Delta L}{L} = \frac{1}{\ln \frac{F}{F_{th}}} \frac{\Delta F}{F}$$

The relative change of the ablation rate increases as the fluence approaches the threshold value, keeping the relative change of fluence constant. Since the number of applied pulses is converted into the depth, the uniform ablation rate during the profiling process is crucial. In case that, as in the last example, the separate analysis for each laser pulse is performed, the pulses that did not result in any material removal can be excluded. However, it is often necessary to



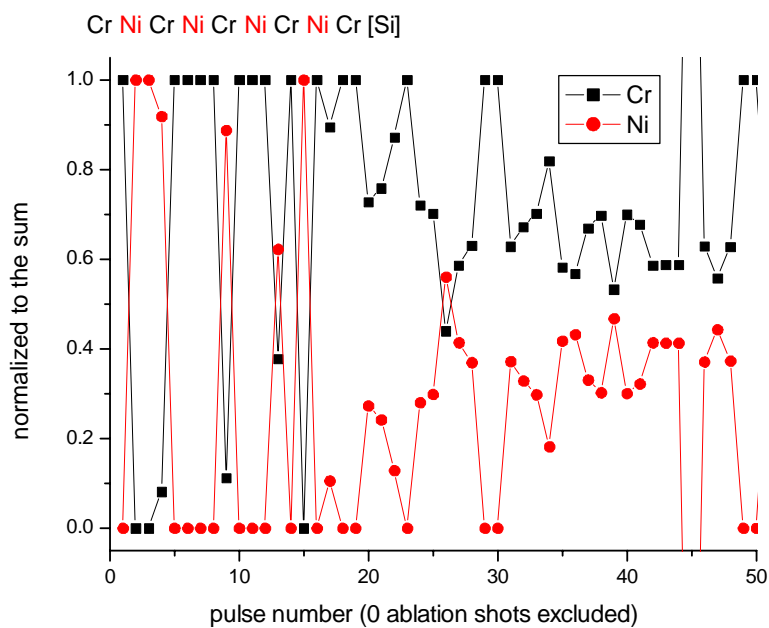


Figure 7-30: Fs-LA-TOF-MS depth profile of NIST SRM 2135c- Ni, Cr, and Si signals are normalized to the sum. Laser fluence  $0.17 \text{ J/cm}^2$ .

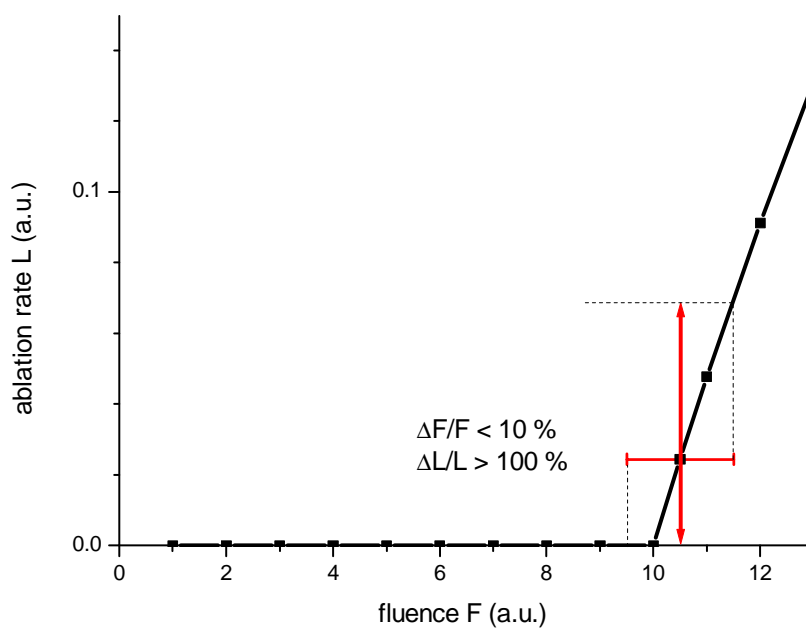


Figure 7-31: Variation of the ablation rate in the vicinity of the threshold fluence.

accumulate the signal from several pulses. In such a case, the discrimination between ablation and no ablation is impossible. The energy stability is, therefore, crucial for the accuracy of the measurement.

## 7.8 Summary

All measurements clearly demonstrate that the femtosecond laser ablation is a promising sampling method for in-depth profiling. With depth resolutions better than 100 nm and lateral resolutions of 10  $\mu\text{m}$ , it could be a good alternative to the established methods such as glow discharge measurements or ion sputtering. There are no special requests either on the ambient conditions (extra clean noble gas, UHV) or on the sample material, and the analysis can be conducted within several seconds. For reliable results, the laser and the detection system should satisfy certain conditions.

**Laser.** Of crucial importance are beam quality and energy stability. Several methods for the creation of the flat-top intensity distribution have been realised and discussed. In the near-threshold fluence regime for slow material removal, it is critical to have no intensity fluctuations across the beam. Fluctuations cause uneven material ablation in parts of the irradiated area, where the fluence is above the threshold. This reduces the depth resolution and the accuracy of the measurement. The energy stability in the reported experiments was between 6 and 12 %, a limiting factor in many measurements. Femtosecond laser systems with much better performance in that sense, more robust and simpler to operate, as well as cheaper became available recently. The presented results should, therefore, be regarded as a demonstration of the feasibility that can still be improved.

**Detection system.** The single pulse multi-elemental analysis should be available, and at best the complete ablated material should be analysed. This is of importance for quantitative measurements, as well as for the trace element analysis, since the sampled quantities are small. Employing a postionisation would be advantageous, providing it allows the single pulse detection.

Better characterisation of the ablation process of different materials is necessary. Precise knowledge of the ablation rates and threshold fluences would help in the choice of the exper-

imental parameters. Such studies of ultrashort laser ablation are being performed in many laboratories around the world.

## Chapter 8

# Conclusion

The main scope of this thesis was the investigation of the physics of femtosecond laser ablation as a solid sampling method for elemental analysis. In comparison to the sampling with longer laser pulses, two aspects could be improved by using ultrashort pulses: elimination of the elemental fractionation from the ablation crater, which is necessary for an accurate quantitative analysis, and better control of material removal (especially for metals), which increases the spatial resolution of microanalysis.

Basic aspects of ultrashort laser ablation were studied in order to use it with optimum efficiency. It could be shown that the results of the LIF study of plasma expansion fit to the simple spherical expansion model of Arnold [29]. The influence of the ambient pressure on the plume expansion and some of the plume properties were understood on that basis. The spectroscopic studies of plasma emission and determination of the excitation temperature served to find suitable conditions for quantitative elemental analysis by LIBS.

The highly energetic ions that antecede the plume expansion were observed under high vacuum conditions in the time of flight spectrometer. The production of so fast ions during the LA of metals could be explained by the space-charge acceleration. The experiments with additional acceleration have shown that the fastest component can be assigned to very high ionisation states. The two peaks that are typical for fs LA TOF signals were previously attributed as the non-thermal and thermal component. These experiments show that none of them is of thermal origin and that both of them might belong to the same mechanism of ion creation. Although these fast ions did not directly influence the analytical measurements performed here,

they might be of interest for future analytical applications.

The expectations that fs LA could bring important improvements to quantitative analysis are fulfilled. There are almost no fractionation effects from the crater when fs lasers are used. The femtosecond laser ablation of brass has shown no signs of the elemental fractionation from the crater. The calibration graphs were linear when the internal standardisation method was employed. Their non-linearity without internal standardisation is the consequence of the different ablation rates for the samples of different composition. The signal intensity was brought into connection with the structure of the samples, using the tabulated material properties. Such connection could not be established for the sampling with longer pulses due to the effects of plasma shielding.

The analysis of the trace element concentrations in a metal matrix, which is one of the more demanding tasks in nanosecond LA-ICP-MS, could be successfully accomplished with femtosecond sampling. The performance of the infrared femtosecond laser in sampling of transparent glasses was as good as of the UV nanosecond lasers. In both cases, the ablation was free from the fractionation effects induced by the laser.

The in-depth profiling was suggested as a promising application for femtosecond laser ablation. Its high potential has been demonstrated on layered samples of different materials. Depth resolution of the order of less than 100 nm was already obtained for some materials. The pre-condition for the controlled material removal is the availability of the flat-top beam intensity profile. Several solutions for the beam shaping were suggested and validated. The limiting factor in these in-depth profiling measurements was low pulse-to-pulse energy stability. Laser systems with much better performance in that respect should be used. Such laser systems became available recently.

The reported measurements were the first applications of a femtosecond laser in analytical chemistry. They produced strong evidence of the high quality performance of fs LA in quantitative bulk analysis, which is very promising for future routine applications. However, the main advantage of ultrashort LA sampling is a high spatial resolution for microanalysis and depth analysis. Quantitative analysis of layered structures could be realised by improving the detection techniques. In particular for analysis at atmospheric pressure and for optical emission measurements, techniques for post-atomisation and post-ionisation of the laser induced plasmas

by another laser or by a transport of the ablated material into the second plasma, (for example, an inductively coupled plasma -ICP), could improve the performance.

# Appendix A

## Elliptical plume

For elliptical plume it is convenient to substitute the radial coordinates used in the spherical model with the rectangular ones [13] (see Figure A-1).  $X_0$ ,  $Y_0$ , and  $Z_0$  are the initial values of the plume boundaries  $X(t)$ ,  $Y(t)$ , and  $Z(t)$ . Anisimov et al. [111] have shown that the shape of the adiabatically expanding plume depends on the gas adiabatic constant  $\gamma$  and the initial ratio of the plume axes  $X_0/Z_0$  only. According to their numerical calculation, the ratio  $k(t) = \frac{Z(t)}{X(t)}$  changes very weakly after  $Z(t)$  becomes 10-100 times bigger than  $X_0$ , so that the asymptotic values  $k(\infty)$  can be used for plume shape evaluations. The total energy and mass  $E$  and  $M$  used in the spherical expansion model are doubled energy and mass of the plume since the expansion is semispherical:  $E = (1 - R)E_{laser} \frac{4\pi}{\Omega}$ ,  $\Omega = 2\pi$ . For elliptical expansion the solid angle can be approximated by

$$\Omega \approx \frac{2\pi}{k(\infty)^2}.$$

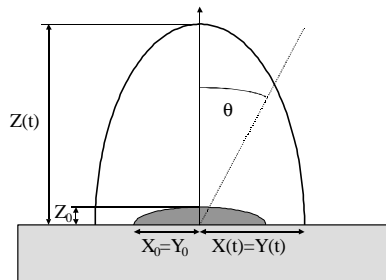


Figure A-1: Scheme for the elliptical plume expansion.

## Appendix B

# Triggering schemes

The detailed triggering schemes are shown in Figures B-1 and B-2. The femtosecond laser system with the master trigger pulses from the SErF seed laser is triggering the rest of the experiments through the delay generator DG535. In Figure B-1 the pulse properties and connections for the LIBS experiment with the Czerny-Turner spectrograph, the CCD camera and the TOF-MS are presented. The settings for the Echelle spectrometer and the dye laser used in the LIF measurements are given in Figure B-2. There is a jitter inherent to these triggering schemes. The TRA's Pockels cell controller and delay generators have their internal clocks that have to be synchronised with the master trigger pulses from the SErF seed laser. The period of the seed laser (repetition rate of 39 MHz) amounts to 25 ns, and that is the jitter of the output pulse with respect to the other signals coming out of the delay generators, i.e. the other components in the experiments.



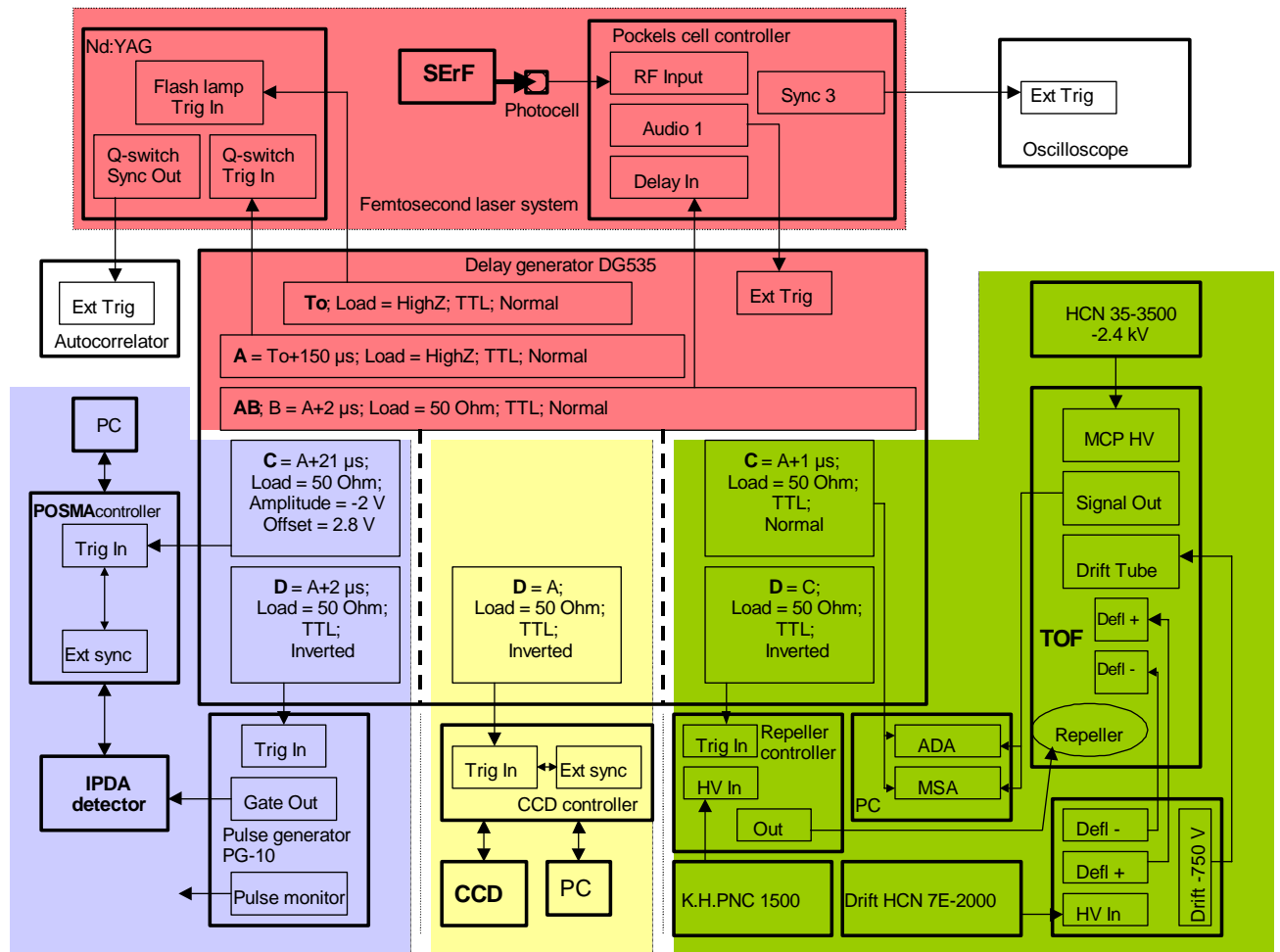


Figure B-1: Triggering scheme of the fs- laser system and the delay generator which controls the detection equipment: POSMA for time-resolved spectroscopy with the Czerny-Turner spectrograph, the CCD camera for beam diagnostics, and the TOF-MS.

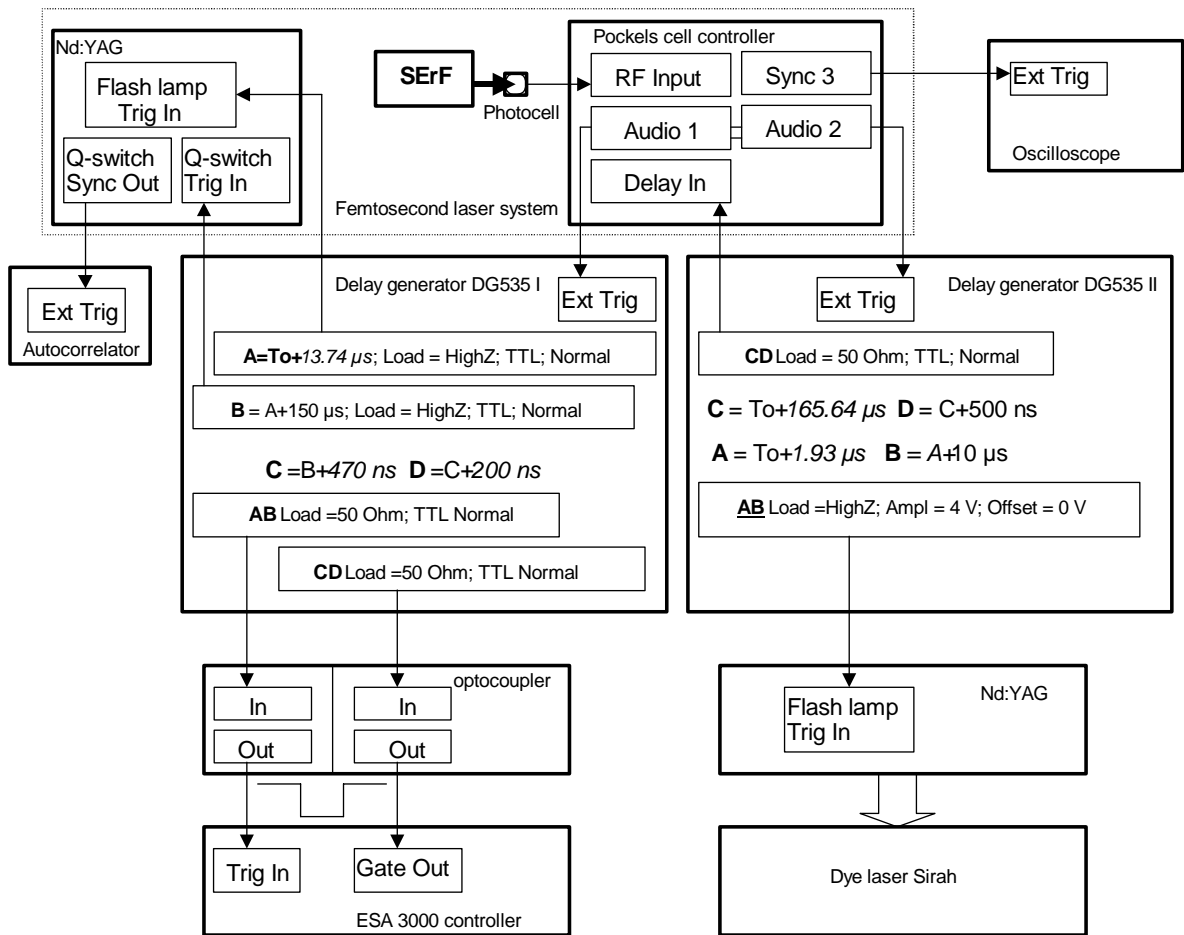


Figure B-2: Triggering scheme of the femtosecond laser system, the echelle spectrometer ESA 3000, and the dye laser. Two delay generators DG535 are necessary for laser ablation + LIF measurements with variable delay.

## Appendix C

# TOF - velocity distribution

The ion velocity distribution can be deduced from a direct time of flight measurement. The TOF signal  $I(t)$  is proportional to the velocity distribution  $f(v_x, v_y, v_z, E)$ . The detector is located at the distance  $x$  normal to the target and a distance  $y$  away from the normal, and its area as well as the area of the laser spot are small compared to their spacing (Figure C-1). The flux of emitted particles in the range  $(v_x, dv_x; v_y, dv_y; v_z, dv_z)$  can be written as  $dv_x dv_y dv_z v_x f(v_x, v_y, v_z, E)$ . Since  $y$  and  $z$  are the directions parallel to the sample surface and  $v_y = y/t$ , where  $t$  is the time of flight,  $dv_y = dy/t$  and  $dv_z = dz/t$ .  $x$  is parallel to the sample normal and the experiment involves the time of flight. Therefore is  $|dv_x| = x dt/t^2$ . For a flux-sensitive detector the TOF signal follows as

$$I(t) \sim x^2 t^{-5} f(v_x, v_y, v_z, E).$$

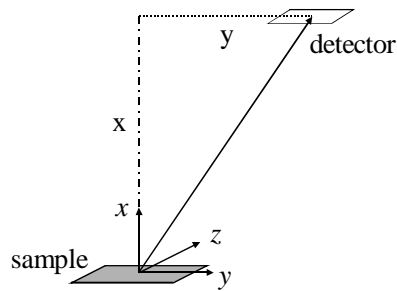


Figure C-1: Position of the TOF detector with respect to the sample and the coordinate axes for the evaluation of the TOF signal.

# Appendix D

## LC properties

Liquid crystal molecules can be visualised as ellipsoids, with a circular symmetry around a single long axis. Adjacent molecules are not rigidly bound to one another, and can rotate or slide with respect to one another under the application of mechanical or electrical forces. In nematic LC, the molecules favour a parallel orientation throughout the entire volume, with randomly located centres within that volume. The alignment direction can be imposed on the molecules by polishing a soft layer (e.g. polyimide) coated on the container glass plate. If the two layers are polished in different directions, a twisted nematic crystal is created (Figure D-1).

Application of an electric field across such a device (transparent conductive layers of indium tin oxide films are placed between alignment layers and glass plates) can induce an electric dipole in each liquid crystal molecule, and often are the charges at the opposite ends of the long direction of the molecule. The torques exerted on these dipoles by applied fields can cause changes in the natural spatial orientation (Figure D-2).

Due to their elongated molecular structure, these materials are anisotropic in their optical behaviour, exhibiting birefringence. Usually the refractive index for polarisation direction parallel to the long molecule axis (extraordinary,  $n_e$ ) is larger than that for polarisations normal to the long axis (ordinary,  $n_o$ ). The difference  $n_e - n_o$  is often in the range of 0.2 or more. A twisted nematic liquid crystal with no voltage applied will affect the light passing through it by rotating the polarisation direction for the twist angle, and by inducing a relative phase retardation between the ordinary and extraordinary polarisation components [112]:

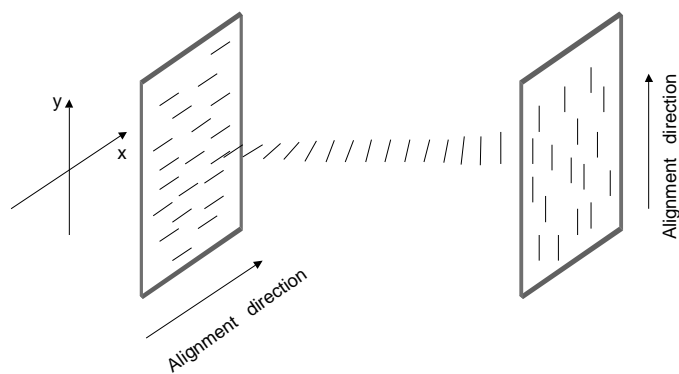


Figure D-1: Orientation of the nematic liquid crystal molecules between the two alignment plates.

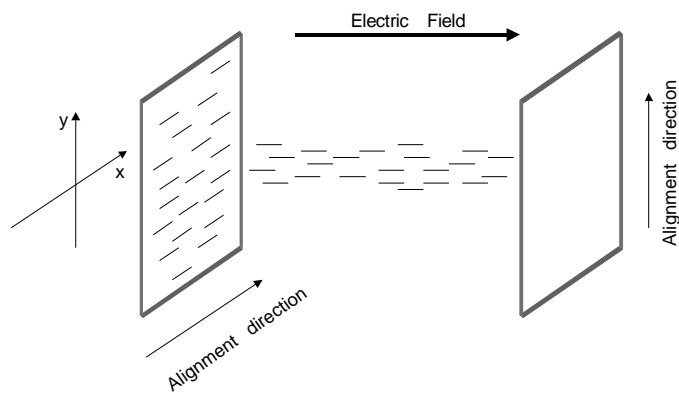


Figure D-2: Orientation of the nematic liquid crystal molecules between the two alignment plates with an applied electric field.

$$\Delta\varphi = \frac{2\pi(n_e - n_o)}{\lambda_0}d$$

where  $\lambda_0$  is the vacuum wavelength of the light and  $d$  is the cell thickness. Applying the voltage across the cell, the long axis direction coincides with the light propagation direction and neither polarisation rotation, nor phase retardation occur. A  $90^\circ$  twisted nematic LC, with a polariser parallel to the front surface alignment and an analyser parallel to the rear surface alignment, allows the light to pass through the cell when no voltage is applied, and blocks it when the full extinction voltage is applied. For a smaller voltage, partial intensity transmission will occur, with a limited range of analog operation.

# Bibliography

- [1] T. H. Maiman, *Nature* **187**, 493 (1960).
- [2] F. Brech and L. Cross, *Appl. Spectrosc.* **16**, 59 (1962).
- [3] N. Omenetto, *J. Anal. At. Spectrom.* **13**, 385 (1998).
- [4] D. A. Rusak, B. C. Castle, B. W. Smith, and J. D. Winefordner, *TrAC* **17**, 453 (1998).
- [5] S. Amoruso, R. Bruzzese, N. Spinelli, and R. Velotta, *J. Phys. B: At. Mol. Opt. Phys.* **32**, R131 (1999).
- [6] D. Günther, I. Horn, and B. Hattendorf, *Fresenius J. Anal. Chem.* **368**, 4 (2000).
- [7] B. N. Chichkov, C. Momma, S. Nolte, F. von Alvensleben, and A. Tünnermann, *Appl. Phys. A* **63**, 109 (1996).
- [8] S. Nolte, C. Momma, H. Jacobs, A. Tünnermann, B. N. Chichkov, B. Wellegehausen, and H. Welling, *J. Opt. Soc. Am. B* **14**, 2716 (1997).
- [9] K. Furusawa, K. Takahashi, H. Kumagai, K. Midorikawa, and M. Obara, *Appl. Phys. A* **69** [Suppl.], 359 (1999).
- [10] S. Preuss, A. Demchuk, and M. Stuke, *Appl. Phys. A* **61**, 33 (1997).
- [11] D. von der Linde and H. Schüler, *J. Opt. Soc. Am. B* **13**, 216 (1996).
- [12] M. Wolf and M. Aeschlimann, *Phys. Bl.* **54**, 145 (1998).
- [13] D. Bäuerle, *Laser Processing and Chemistry-3<sup>rd</sup> ed.*, Springer, Berlin, 2000.

- [14] N. F. Mott and H. Jones, *The theory of the properties of metals and alloys*, Dover Publications, New York, 1958.
- [15] J. C. Kieffer, P. Audebert, M. Chaker, J. P. Matte, H. Pépin, T. W. Johnston, P. Maine, D. Meyerhofer, J. Delettrez, D. Strickland, P. Bado, and G. Mourou, *Phys. Rev. Lett.* **62**, 760 (1989).
- [16] M. Born and E. Wolf, *Principles of Optics-6<sup>th</sup> ed. (with corrections)*, Pergamon Press, Oxford, 1993.
- [17] P. Gibbon and E. Förster, *Plasma Phys. Control. Fusion* **38**, 769 (1996).
- [18] R. Fedosejevs, R. Ottmann, R. Sigel, G. Kühnle, S. Szatmari, and F. P. Schäfer, *Phys. Rev. Lett.* **64**, 1250 (1990).
- [19] K. Sokolowski-Tinten and D. von der Linde, *Phys. Rev. B* **61**, 2643 (2000).
- [20] R. Stoian, Investigation of the Dynamics of Material Removal in Ultrashort Pulsed Laser Ablation of Dielectrics, *Dissertation*, Freie Universität Berlin, 2000.
- [21] S. I. Anisimov, M. I. Tribel'ski, and G. Ya Epel'baum, *Sov. Phys. JETP* **51**, 802 (1980).
- [22] E. Matthias, M. Reichling, J. Siegel, O. W. Käding, S. Petzoldt, H. Skurk, P. Bizenberger, and E. Neske, *Appl. Phys. A* **58**, 129 (1994).
- [23] S.-S. Wellershoff, J. Hohlfeld, J. Güdde, and E. Matthias, *Appl. Phys. A* **69** [Suppl.], 99 (1999).
- [24] F. Vidal, T. W. Johnston, S. Laville, O. Barthélemy, M. Chaker, B. Le Drogoff, J. Margot, and M. Sabsabi, *Phys. Rev. Lett.* **86**, 2573 (2001).
- [25] R. Kelly and A. Miotello, *Appl. Surf. Sci.* **96-98**, 205 (1996).
- [26] A. Miotello and R. Kelly, *Appl. Phys. A* **69** [suppl.], 67 (1999).
- [27] V. P. Skripov, *Metastable Liquids*, John Wiley & Sons, New York, 1974.
- [28] M. M. Martynyuk, *Russ. J. Phys. Chem.* **57(4)**, 494 (1983).



- [29] N. Arnold, J. Gruber, and J. Heitz, *Appl. Phys. A* **69** [suppl.], 87 (1999).
- [30] Zs. Márton, P. Heszler, Á. Mechler, B. Hopp, Z. Kántor, and Zs. Bor, *Appl. Phys. A* **69** [suppl.], 133 (1999).
- [31] N. Huber, J. Gruber, N. Arnold, J. Heitz, and D. Bäuerle, *Europhys. Lett.* **51**, 674 (2000).
- [32] F. Kokai, K. Takahashi, K. Shimizu, M. Yudasaka, and S. Iijima, *Appl. Phys. A* **69** [suppl.], 223 (1999).
- [33] B. C. Stuart, M. D. Feit, S. Herman, A. M. Rubenchik, B. W. Shore, and M. D. Perry, *Phys. Rev. B* **53**, 1749 (1996).
- [34] J. B. Ko, W. Sdorra, and K. Niemax, *Fresenius Z. Anal. Chem.* **335**, 648 (1989).
- [35] A. A. Sysoev, A. A. Sysoev, S. S. Poteshin, V. I. Pyatakhin, I. V. Shchekina, A. S. Trofimov, *Fresenius J. anal. Chem.* **361**, 261 (1998).
- [36] A. A. Sysoev, *Eur. J. Mass Spectrom.* **6**, 501 (2000).
- [37] W. Sdorra and K. Niemax, *Microchim. Acta* **107**, 319 (1992).
- [38] W. Sdorra, J. Brust, and K. Niemax, *Microchim. Acta* **108**, 1 (1992).
- [39] D. Günther, S. E. Jackson, H. P. Longerich, *Spectrochim. Acta Part B* **54**, 381 (1999).
- [40] M. Guillong and D. Günther, *J. Anal. At. Spectrom.* DOI: 10.1039/b202988j (2002).
- [41] F. Leis, W. Sdorra, J. B. Ko, K. Niemax, *Mikrochim. Acta* **II**, 185 (1989).
- [42] A. Quentmeier, W. Sdorra, and K. Niemax, *Spectrochim. Acta* **45B**, 537 (1990).
- [43] D. Günther, A. Audétat, R. Frischknecht, and C. A. Heinrich, *J. Anal. At. Spectrom.* **13**, 263 (1998).
- [44] D. Günther, R. Frischknecht, C. A. Heinrich, and H.-J. Kahlert, *J. Anal. At. Spectrom.* **12**, 939 (1997).
- [45] S. E. Jackson, H. P. Longerich, G. R. Dunning, B. J. Fryer, *Can. Mineral.* **30**, 1049 (1992).

- [46] T. E. Jeffries, S. E. Jackson, H. P. Longerich, *J. Anal. At. Spectrom.* **13**, 935 (1998).
- [47] E. F. Cromwell and P. Arrowsmith, *Appl. Spectrosc.* **49**, 1652 (1995).
- [48] D. J. Figg, J. B. Cross, C. Brink, *Appl. Surf. Sci.* **127-129**, 287 (1998).
- [49] P. M. Outridge, W. Doherty, D. C. Gregoire, *Spectrochim. Acta Part B* **52**, 2093 (1997).
- [50] X. Mao, W.-T. Chan, M. Caetano, M. A. Shannon, and R. E. Russo, *Appl. Surf. Sci.* **96-98**, 126 (1996).
- [51] O. V. Borisov, X. L. Mao, A. Fernandez, M. Caetano, and R. E. Russo, *Spectrochim. Acta Part B* **54**, 1351 (1999).
- [52] A. Semerok, C. Chaleard, V. Detalle, J.-L. Lacour, P. Mauchien, P. Meynadier, C. Nouvellon, B. Salle, P. Palianov, M. Perdix, and G. Petite, *Appl. Surf. Sci.* **311**, 138 (1999).
- [53] A. P. K. Leung, W. T. Chan, X. L. Mao, and R. E. Russo, *Anal. Chem.* **70**, 4709 (1998).
- [54] M. K. Kim, T. Takao, Y. Oki, and M. Maeda, *Jpn. J. Appl. Phys.* **39**, 6277 (2000).
- [55] V. Margetic, A. Pakulev, A. Stockhaus, M. Bolshov, K. Niemax, and R. Hergenröder, *Spectrochim. Acta Part B* **55**, 1771 (2000).
- [56] V. Margetic, K. Niemax, and R. Hergenröder, *Spectrochim. Acta Part B* **56**, 1003 (2001).
- [57] V. Margetic, M. Bolshov, A. Stockhaus, K. Niemax, and R. Hergenröder, *J. Anal. At. Spectrom.* **16**, 616 (2001).
- [58] J.-C. Diels and W. Rudolph, *Ultrashort Laser Pulse Phenomena*, Academic Press, London, (p. 376) 1996.
- [59] H. Varel, Untersuchungen zur Ablation dielektrischer Materialien mittels Ultrakurzpulslaser, *Dissertation*, Freie Universität Berlin, 1999.
- [60] J. Krüger, Ultrakurze Laserimpulse in der Mikromaterialbearbeitung, *Dissertation*, Brandenburgische Technische Universität Cottbus, 1999.

- [61] I. Feldmann, W. Tittes, N. Jakubowski, D. Stuewer, and U. Giesmann, *J. Anal. At. Spectrom.* **9**, 1007 (1994).
- [62] W. Tittes, N. Jakubowski, D. Stuewer, G. Toelg, and J. A. C. Broekaert, *J. Anal. At. Spectrom.* **9**, 1015 (1994).
- [63] W. Tittes, Untersuchungen zur analytischen Charakterisierung eines neuen hochauflösenden ICP-Massenspektrometers, *Dissertation*, Universität Dortmund, 1994.
- [64] C. Thomas, Anwendung von hocheffizienten Zerstäubungstechniken bei der Kopplung von HPLC und ICP-Massenspektrometrie zur Speziation von Selen in biologischem Material, *Dissertation*, Universität Dortmund, 1998.
- [65] D. Günther and C. Heinrich, *J. Anal. At. Spectrom.* **14**, 1363 (1999).
- [66] J. Bonse, S. Baudach, J. Krüger, W. Kautek, and M. Lenzner, *Appl. Phys. A* **74**, 19 (2002).
- [67] S. Nolte, G. Kamlage, T. Bauer, F. Korte, C. Fallnich, A. Ostendorf, and F. von Alvensleben, *LaserOpto* **31**, 72 (1999).
- [68] F. Dausinger, T. Abeln, D. Breitling, J. Radtke, V. Konov, S. Garnov, S. Klimentov, T. Kononenko, and O. Tsarkova, *LaserOpto* **31**, 78 (1999).
- [69] Y. Jee, M. F. Becker, and R. M. Walser, *J. Opt. soc. Am. B* **5**, 648 (1988).
- [70] S. Petzoldt, A. P. Elg, J. Reif, and E. Matthias, “Shockwave detection, an efficient way to determine multiple-pulse damage thresholds,” in *Laser induced damage in optical materials*, H. E. Benett et al., ed., Proc. SPIE 1438, ASTM STP - 1117, NIST special publication 801 (1990).
- [71] J. D. Morrow, “Cyclic plastic strain energy and fatigue of metals,” in *International Friction Damping and Cyclic Plasticity* (American Society for Testing & Materials, Philadelphia, Pa., 1965), p. 45.

- [72] W. Sdorra, Fluoreszenz- und emissionsspektroskopische Untersuchungen der Verdampfung fester Proben durch Laserstrahlung zur Analyse von Spurenelementen, *Dissertation*, Universität Dortmund, 1991.
- [73] R. W. Dreyfus, *J. Appl. Phys.* **69**, 1721 (1991).
- [74] W. Sdorra and K. Niemax, *Spectrochim. Acta* **45B**, 917 (1990).
- [75] W. Pietsch, B. Dubreuil, and A. Briand, *Appl. Phys. B* **61**, 267 (1995).
- [76] B. A. Bushaw and M. L. Alexander, *Appl. Surf. Sci.* **127-129**, 935 (1998).
- [77] J. A. Aguilera and C. Aragón, *Appl. Phys. A* **69** [Suppl.], S475 (1999).
- [78] E. M. Monge, C. Aragón, and J. A. Aguilera, *Appl. Phys. A* **69** [Suppl.], S691 (1999).
- [79] J. C. S. Kools and J. Dieleman, *J. Appl. Phys.* **74** (6), 4163 (1993).
- [80] V. Margetic, T. Ban, F. Leis, K. Niemax, and R. Hergenröder, *submitted*.
- [81] J. Brust, Untersuchungen zum Feinstrukturtransfer in Magnesium- und Kalziumionen mit Hilfe eines laserinduzierten Plasmas, *Diplomarbeit*, Universität Dortmund, 1992.
- [82] R. F. Wood, K. R. Chen, J. N. Leboeuf, A. A. Puretzky, and D. B. Geohegan, *Phys. Rev. Lett.* **79**, 1571 (1997).
- [83] R. F. Wood, J. N. Leboeuf, K. R. Chen, D. B. Geohegan, and A. A. Puretzky, *Appl. Surf. Sci.* **127-129**, 151 (1998).
- [84] M. von Allmen and A. Blatter, *Laser-Beam Interactions with Materials-2nd ed.*, Springer, Berlin, 1995.
- [85] F. Garrelie, C. Champeaux, and A. Catherinot, *Appl. Phys. A* **69** [Suppl.], S55 (1999).
- [86] B. Le Drogoff, J. Margot, M. Chaker, M. Sabsabi, O. Barthélemy, T. W. Johnston, S. Laville, F. Vidal, and Y. von Kaenel, *Spectrochim. Acta Part B* **56**, 987 (2001).
- [87] A. Miotello and R. Kelly, *Appl. Surf. Sci.* **138-139**, 44 (1999).

- [88] S. Amoruso, X. Wang, C. Altucci, C. de Lisio, M. Armenante, R. Bruzzese, and R. Velotta, *Appl. Phys. Lett.* **77**, 3728 (2000).
- [89] R. P. van Ingen, *J. Appl. Phys.* **76** (12), 8055 (1994).
- [90] S. Amoruso, X. Wang, C. Altucci, C. de Lisio, M. Armenante, R. Bruzzese, N. Spinelli, and R. Velotta, *Appl. Surf. Sci.* **186**, 358 (2002).
- [91] J. Baldwin, *Appl. Spectrosc.* **24**, 429 (1970).
- [92] M. Gagean and J. M. Mermet, *Spectrochim. Acta Part B* **53**, 581 (1998).
- [93] L. Moenke-Blankenburg, *Spectrochim. Acta Rev. 1* **15**, 37 (1993).
- [94] A. Fernandez, X. L. Mao, W. T. Chan, M. A. Shannon, and R. E. Russo, *Anal. Chem.* **67**, 2444 (1995).
- [95] Landolt-Börnstein, New Series IV/5d, p. 289, Springer, Berlin, 1971.
- [96] A. Cottrell, *Concepts in the Electron Theory of Alloys*, Ch. 9, St Edmundsbury Press, UK, 1998, p. 95.
- [97] Landolt-Börnstein, New Series III/15c, p. 215-219, Springer, Berlin, 1991.
- [98] Landolt-Börnstein, 6.Auflage, II. Band, 4. Teil, p. 818, Springer, Berlin, 1961.
- [99] Landolt-Börnstein, 6.Auflage, II. Band, 4. Teil, p. 766, Springer, Berlin, 1961.
- [100] M. Lenzner, J. Krüger, W. Kautek, and F. Krausz, *Appl. Phys. A* **68**, 369 (1999).
- [101] I. Zergioti, M. Stuke, *Appl. Phys. A* **67**, 391 (1998).
- [102] J. M. Vadillo and J. J. Laserna, *J. Anal. At. Spectrom.* **12**, 859 (1997).
- [103] C. C. García, M. Corral, J. M. Vadillo, and J. J. Laserna, *Appl. Spectrosc.* **54**, 1027 (2000).
- [104] D. R. Anderson, C. W. McLeod, T. English, and A. T. Smith, *Appl. Spectrosc.* **49**, 691 (1995).

- [105] A. Plotnikov, C. Vogt, V. Hoffmann, C. Täschner, and K. Wetzig, *J. Anal. At. Spectrom.* **16**, 1290 (2001).
- [106] J. Bonse, P. Rudolph, J. Krüger, S. Baudach, and W. Kautek, *Appl. Surf. Sci.* **154-155**, 659 (2000).
- [107] H. Spillmann, P. R. Willmott, M. Morstein, and P. J. Uggowitzer, *Appl. Phys. A* **73**, 441 (2001).
- [108] K. Wetzig, S. Baunack, V. Hoffmann, and F. Präßler, *Fresenius J. Anal. Chem.* **358**, 25 (1997).
- [109] R. Klockenkämper, A. van Bohlen, H. W. Becker, and L. Palmetshofer, *Surf. Interface Anal.* **27**, 1003 (1999).
- [110] F. M. Dickey and S. C. Holswade Eds., *Laser Beam Shaping: Theory and Techniques*, Marcel Dekker, Inc., New York, 2000.
- [111] S. I. Anisimov, D. Bäuerle, B. S. Luk'yanchuk, *Phys. Rev. B* **48**, 12076 (1993).
- [112] J. W. Goodman, *Introduction to Fourier Optics-2<sup>nd</sup>* ed., McGraw-Hill, New York, 1996.

# Acknowledgements

This thesis resulted from the experiments performed at the Institute of Spectrochemistry and Applied Spectroscopy in Dortmund, funded by the Deutsche Forschungsgemeinschaft. I am very grateful to **Dr. Roland Hergenröder** and **Prof. Dr. Kay Niemax** for giving me the opportunity to work on this very interesting project.

I wish to thank Roland for his guidance and support during the last three and half years, for everything I have learned and achieved, and for the wonderful friendship that arose from our cooperation.

To my supervisor, Prof. Dr. Niemax, I am thankful for many suggestions and fruitful discussions, especially during the writing of my thesis. Sincere thanks to Prof. Dr. D. Suter for accepting to be the second referee and for his interest in my work.

It has been very pleasant to be a member of the (ex-)AG 313 lead by Prof. Dr. M. Bolshov. I want to thank him and **all** my colleagues for their help, support, stimulative discussions and a very friendly working atmosphere. Very special thanks go to the one sharing the darkness and light of the lab with me- Antje Michels (Stockhaus) for her immense contribution and for refusing to speak English.

I'm happy to say that I had very good cooperation with many other ISAS colleagues- from the administration, maintenance, electrical and mechanical workshop to PhD students and researchers. That was very important for me and I am very grateful to all of them. I want to thank to colleagues from ISAS Berlin, especially Dr. E. Hoffmann and Mr. J. Skole for their help with the TOF-MS.

It is hard to imagine this thesis without the information from scanning electron microscope. Mrs. M. Becker and Mr. A. von Bohlen were always ready to help with it and I thank them here for that, for their curiosity and many inspiring discussions. For the cooperation and help with the ICP-MS, I am obliged to Dr. N. Jakubowski, Mr. I. Feldmann, and Dr. J. Koch. The LIF experiments with Mr. Sc. T. Ban and Dr. F. Leis were a good fun. Ticijana, we should do something like that again!

Dr. H. Swoboda and Dr. G. Jung from Jobin-Yvon GmbH were of great help with the laser system. I want to thank them for their assistance at all times. Dr. A. Pakulev should be thanked for starting the femtosecond laser and for the preliminary experiments.

Sincere thanks go to Liz and Steve Tingley for editing my thesis.

Without the unconditional love and support from my parents and family I certainly would not have made it so far. Veliko vam hvala! I want to thank to my friends all around the world, just for being there for me.

To my soulmate and husband Floris Hommes I want to thank for his patience and support, for long phone calls, and for all the kilometres driven.

# Curriculum vitae

Name: Vanja Margetić

Date of birth: January 18<sup>th</sup>, 1973

Place of birth: Bjelovar, Croatia

Parents: Danica and Boško Margetić

## Education:

- 1999-2002 PhD, Institute of Spectrochemistry and Applied Spectroscopy,  
University of Dortmund, Germany
- 2000 Participant of the WE-Heraeus-Ferienkurs für Physik “Wechselwirkung  
intensiver Laserfelder mit Materie”, Jena, Germany, Sep 11-22, 2000
- 1997 Diploma thesis “Glow discharge in Ar/O<sub>2</sub> mixtures- electron temperature  
and collision broadening of oxygen emission lines” at the  
Institute of Physics, Zagreb, Croatia
- 1991-1997 Department of Physics, University of Zagreb, Croatia

## Employment:

- since Jan 1999 Institute of Spectrochemistry and Applied Spectroscopy,  
Dortmund, Germany